ANTINEUTRINO CHARM PRODUCTION AND PENTAQUARK SEARCH IN
THE CHORUS EXPERIMENT

A THESIS SUBMITTED TO
THE GRADUATE SCHOOL OF NATURAL AND APPLIED SCIENCES
OF
MIDDLE EAST TECHNICAL UNIVERSITY

BY

UMUT KÖSE

IN PARTIAL FULFILLMENT OF THE REQUIREMENTS

FOR

THE DEGREE OF DOCTOR OF PHILOSOPHY

IN

PHYSICS

NOVEMBER 2006

Approval of the Graduate School of Natural and Applied Sciences.

Prof. Dr. Canan Özgen
Director

I certify that this thesis satisfies all the requirements as a thesis for the degree of Doctor of Philosophy.

Prof. Dr. Sinan Bilikmen
Head of Department

This is to certify that we have read this thesis and that in our opinion it is fully adequate, in scope and quality, as a thesis for the degree of Doctor of Philosophy.

Assoc. Prof. Dr. Ali Murat
Güler
Supervisor

Examining Committee Members

Prof. Dr. Ali Ulvi Yılmazer (Ankara Uni.,PHYS) ⎯⎯⎯⎯⎯⎯⎯⎯⎯⎯

Assoc. Prof. Dr. Ali Murat Güler (METU,PHYS) ⎯⎯⎯⎯⎯⎯⎯⎯⎯⎯

Prof. Dr. Kimio Niwa (Nagoya Uni.,PHYS) ⎯⎯⎯⎯⎯⎯⎯⎯⎯⎯

Assoc. Prof. Dr. Bayram Tekin (METU,PHYS) ⎯⎯⎯⎯⎯⎯⎯⎯⎯⎯

Assist. Prof. Dr. Osamu Sato (Nagoya Uni.,PHYS) ⎯⎯⎯⎯⎯⎯⎯⎯⎯⎯

"I hereby declare that all information in this document has been obtained and presented in accordance with academic rules and ethical conduct. I also declare that, as required by these rules and conduct, I have fully cited and referenced all material and results that are not original to this work."

Name Surname : UMUT KÖSE

Signature :

ABSTRACT

ANTINEUTRINO CHARM PRODUCTION AND PENTAQUARK SEARCH

IN THE CHORUS EXPERIMENT

KÖSE, UMUT

Ph.D., Department of Physics

Supervisor: Assoc. Prof. Dr. Ali Murat Güler

November 2006, 156 pages.

During the years between 1994 and 1997, the emulsion target of the CHORUS experiment was exposed to the wide band neutrino beam of the CERN SPS of 27 GeV average energy collecting about 10^6 neutrino interactions. A measurement of $\bar{\nu}_\mu$ induced charm production and search for anticharmed pentaquark (Θ_c^0) have been performed by using the presence of a 6% $\bar{\nu}_\mu$ component in the beam. By requiring a positive muon charge as determined by the CHORUS muon spectrometer, 46 $\bar{\nu}_\mu$-induced charm events were observed with an estimated background of 5.2 ± 0.4 events. At an average antineutrino energy of 18 GeV in the neutrino beam, the charm production rate induced by $\bar{\nu}_\mu$ is

measured to be

$$\frac{\sigma(\bar{\nu}N \to \mu^+\bar{c}X)}{\sigma(\bar{\nu}N \to \mu^+X)} = 4.55^{+0.96}_{-0.81}(\text{stat}) \pm 0.64(\text{syst})\%.$$

$\bar{D}^0$ and charged charm (D^-, D_s^-) production rates are measured to be

$$\frac{\sigma(\bar{\nu}_\mu N \to \mu^+\bar{D}^0 X)}{\sigma(\bar{\nu}_\mu N \to \mu^+X)} = (2.86^{+0.71}_{-0.59}(\text{stat}) \pm 0.14(\text{syst}))\%,$$

$$\frac{\sigma(\bar{\nu}_\mu N \to \mu^+(D^-, D_s^-)X)}{\sigma(\bar{\nu}_\mu N \to \mu^+X)} = (1.69^{+0.62}_{-0.52}(\text{stat}) \pm 0.24(\text{syst}))\%.$$

The ratio between neutral and charged charm production rates is found to be

$$1.69^{+0.75}_{-0.63}(\text{stat}) \pm 0.21(\text{syst}).$$

By using the $\bar{\nu}_\mu$ data sample, anticharmed pentaquark (Θ_c^0) have been searched and no evidence is found. Based on the null observation, the limit on the Θ_c^0 production is found as a function of different possible Θ_c^0 lifetimes. The tightest bound is $\sigma_{\Theta_c^0}/\sigma_{\bar{\nu}} < 0.039$ at 90% C.L by assuming that Θ_c^0 lifetime is equal to $0.5 c\tau_{D^0}$.

Keywords: Antineutrino, Charm Production, Pentaquark, Emulsion.

ÖZ

CHORUS DENEYİNDE ANTİNÖTRİNO ETKİLEŞMLERİNDE CHARM ÜRETİMİ VE PENTAQUARK ARANMASI

KÖSE, UMUT

Doktora, Fizik Bölümü

Tez Yöneticisi: Assoc. Prof. Dr. Ali Murat Güler

Kasım 2006, 156 sayfa.

1994-1997 yılları arasında, CHORUS emulsiyon hedefi, CERN SPS'te üretilen 27 GeV ortalama enerjili nötrino hüzmesi ile bombardıman edilmiş ve yaklaşık olarak 10^6 nötrino etkileşimi kaydedilmiştir. Nötrino hüzmesinde bulunan %6 oranındaki $\bar{\nu}_\mu$ kullanılarak, etkileşimindeki charm üretimi ve anticharm içeren pentaquark çalışılmıştır. CHORUS müyon spektrometrede pozitif müyon içeren 46 $\bar{\nu}_\mu$ charm bozunumu, 5.2±0.4 fon yoğunluğu (background) ile gözlenmiştir. Nötrino hüzmesindeki ortalama 18 GeV antinötrino enerjisinde, charm üretim oranı

$$\frac{\sigma(\bar{\nu}N \to \mu^+ \bar{c}X)}{\sigma(\bar{\nu}N \to \mu^+ X)} = \%(4.55^{+0.96}_{-0.81}(\text{istat}) \pm 0.64(\text{sist})).$$

$\bar{D}^0$ ve yüklü charm (D^-, D_s^-) üretim oranı da

$$\frac{\sigma(\bar{\nu}_\mu N \to \mu^+ \bar{D}^0 X)}{\sigma(\bar{\nu}_\mu N \to \mu^+ X)} = \%(2.86^{+0.71}_{-0.59}(\text{istat}) \pm 0.14(\text{sist})),$$

$$\frac{\sigma(\bar{\nu}_\mu N \to \mu^+ (D^-, D_s^-) X)}{\sigma(\bar{\nu}_\mu N \to \mu^+ X)} = \%(1.69^{+0.62}_{-0.52}(\text{istat}) \pm 0.24(\text{sist}))$$

olarak ölçülmüştür. Yüksüz ve yüklü charm üretim oranı

$$1.69^{+0.75}_{-0.63}(\text{istat}) \pm 0.21(\text{sist})$$

olarak bulunmuştur.

Antinötrino datası kullanılarak anticharm içeren pentaquark (Θ_c^0) aranmış ve hiç bir aday gözlenememiştir. Bu koşullar altında, Θ_c^0'nin farklı olası yaşam ömürlerinde, üretim limiti hesaplanmıştır. Θ_c^0'nin $0.5c\tau_{D^0}$ yasam ömründe üretim oranı %90 C.L.'de $\sigma_{\Theta_c^0}/\sigma_{\bar{\nu}} < 0.039$ olarak ölçülmüştür.

Anahtar Kelimeler: Antinötrino, Charm Üretimi, Pentaquark, Emulsiyon

To my Family and "Umut".....

ACKNOWLEDGMENTS

TABLE OF CONTENTS

LIST OF TABLES

xvi

LIST OF FIGURES

CHAPTER 1

INTRODUCTION

Ever since the beginning of the twentieth century, physicists have been searching for the answers of the following questions:

- what are the basic building blocks of matter?

- what are the interactions between those building blocks?

Experimental and theoretical work on these two questions have led to the Standard Model [1, 2, 3] of particle physics: an almost complete picture of high energy physics, save gravity. According to the Standard Model, matter in the universe is made up of elementary fermions interacting through bosonic fields. The fermions can be arranged in three generations, the first one consisting of the electron, the up and down quarks, and the electron neutrino. All ordinary matter is made of the first generation particles. The higher generation particles decay quickly into the first generation ones and can only exist for a short time in high energy experiments. The second generation consists of the muon, the muon neutrino and

1

the strange and charm quarks. The third generation consists of the tau lepton, the tau neutrino and the bottom and top quarks. These are the basic building blocks of matter.

The neutrino is now central to elementary particle physics, astrophysics, and cosmology. Neutrinos play a key role in theories that unify the elementary particles and forces. There are three types of neutrinos: ν_e, ν_μ, and ν_τ, so named because they are associated with the electron, muon, and tau particles. The three neutrinos differ from the nine other building blocks of matter because they are so light and interact so weakly. These two differences are at the root of their importance to modern astrophysics and physics.

Neutrinos also allow us to study the forces of nature at the shortest distances by observing rare processes in which they participate. For instance, neutrinos permit us to see deep into the nuclei of atoms through the process of neutrino scattering from the quarks within the nucleons. Their tiny masses and the transformations of one neutrino type to another have even revealed physics beyond the Standard Model of particle physics. Studying and understanding neutrino mass and oscillations provide a unique view into how the forces and particles are unified.

The CHORUS experiment was designed to search for $\nu_\mu \rightarrow \nu_\tau$ oscillation by using the CERN neutrino beam to investigate a different regime of mass and mixing parameters than the Super-Kamiokande experiment. The CHORUS experiment

has not observed a signal for neutrino oscillation. The CHORUS detector is also suitable for the study of neutrino production of charmed hadrons, since charmed hadrons have lifetimes similar to that of the τ lepton, and can be detected with the same procedures used for latter.

High energy neutrino interactions produce charm in a few percent of the events and therefore they are a good tool to study charm physics. The study of charm production is an important testing ground for perturbative QCD due to the large contribution from gluon initiated diagrams. In addition, understanding the threshold behavior associated with the heavy charm mass is critical to the extraction of the weak mixing angle $\sin\theta_W$ from neutrino neutral-current and charged-current data.

Another interesting aspect of charm physics is charm spectroscopy. In general, hadron spectroscopy investigates the masses, widths, decay channels and quark contents of hadrons. And it is known that QCD allows various colorless combinations of quarks. Nevertheless, up to now, only mesons, composed of a quark and an antiquark, and baryons, composed of three quarks, have been observed in the experiments. In the last three years, the search for states with more than three quarks has become a very active field. The observation of a narrow resonance decaying to K^+n or K^0p and its interpretation as a strange pentaquark triggered new interest in the baryon spectroscopy, since it is an exotic particle.

Thesis Outline:

In this thesis, the measurement of antineutrino charm production and the results for the searches for an anticharmed pentaquark particle in antineutrino interactions from the CHORUS experiment are presented. After the current introductory chapter, a theoretical framework is given in Chapter 2 on neutrino interactions, including charm and pentaquark production by neutrinos. In Chapter 3, the experimental setup of the CHORUS detector is briefly introduced. Chapter 4 explains the data taking, location of the neutrino interactions in emulsion and the detailed description of the NetScan technique to scan the emulsion and to reconstruct the events. Chapter 5 deals with the measurement of antineutrino charm production rate. In Chapter 6, the description of the pentaquark analysis methods and results in CHORUS is discussed. Finally, Chapter 7 presents the conclusions.

CHAPTER 2

NEUTRINO NUCLEON INTERACTIONS

The neutrino deep-inelastic scattering is an interesting tool to have information on the parton densities in the nucleon. Furthermore, the neutrino scattering is a way to study the heavy quark production due to the light to heavy quark charged current interactions. Charge conservation requires that neutrinos scatter from quarks and antineutrinos scatter from antiquarks.

In the following, the theoretical framework of the neutrino interactions and charm production will be discussed.

2.1   Kinematics

The process of the neutrino-nucleon interaction is usually described in terms of the kinematic variables shown in Figure 2.1. The four-momenta introduced are k for the incoming neutrino, k' for the muon, p for the nucleon and p' for the hadronic final state and $q = k - k' = p' - p$ for the four-momentum carried by the W-boson. The Lorentz invariant kinematic variables are:

- $E_\nu = E_\mu + E_{had}$,   the neutrino energy,

- $s = (k + p)^2$,   square of the center-of-mass energy,

- $\nu = \frac{p.q}{m} = E_\nu - E_\mu = E_{had}$,   energy transferred from the neutrino to the nucleon,

- $Q^2 = -q^2 = -(k - k')^2 = -(p' - p)^2$,   square of the four-momentum transfer,

- $W^2 = (p')^2$,   square of the hadronic final state invariant mass,

- $x = \frac{Q^2}{2p.q}$,   Bjorken scaling variable, in the parton model, x can be interpreted as the fraction of the target nucleon's longitudinal momentum carried by the struck quark,

- $y = \frac{p.q}{p.k}$,   inelasticity variable, measures the ratio of the energy transferred to the hadronic system, to the total leptonic energy available in the target's rest frame. And it is directly related to the lepton scattering angle θ in the center-of-mass frame; $y \simeq 1 - \frac{1}{2}(1 + \cos\theta)$.

When the fermi motion related to nuclear binding energy is neglected, and the nucleon is considered to be at rest, the four momenta can be written in the laboratory system as:
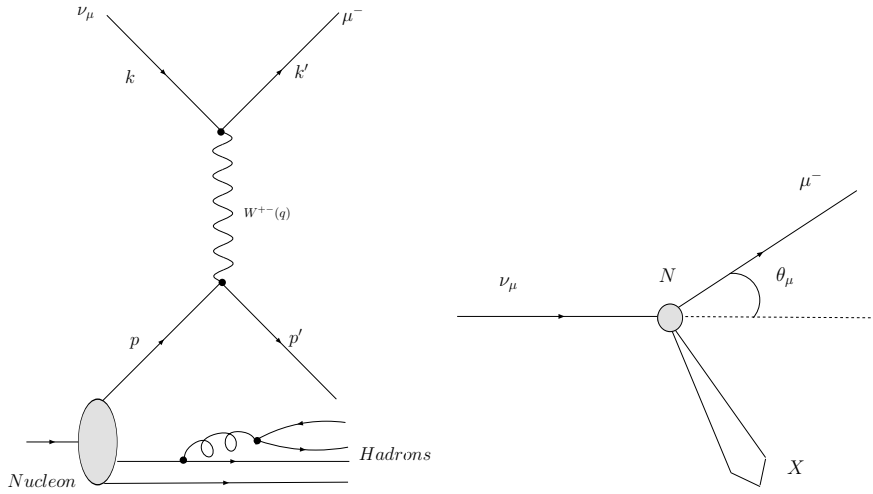
Figure 2.1: Feynman diagrams of the $\nu_\mu N \to \mu^- X$ process.

$$p = \begin{pmatrix} M \\ 0 \\ 0 \\ 0 \end{pmatrix}, k = \begin{pmatrix} E_\nu \\ 0 \\ 0 \\ E_\nu \end{pmatrix}, k' = \begin{pmatrix} E_\mu \\ E_\mu \sin\theta_\mu \cos\phi_\mu \\ E_\mu \sin\theta_\mu \sin\phi_\mu \\ E_\mu \cos\theta_\mu \end{pmatrix} \qquad (2.1)$$

where M is the nucleon rest mass, E_ν the neutrino energy, E_μ the muon energy and θ_μ and ϕ_μ are the scattering angle of the outgoing muon, also E_{had} is the energy of the hadronic final state. The muon mass is negligible.

$$y = \frac{\nu}{E_\nu}, \qquad (2.2)$$

$$Q^2 = 2E_\nu(E_\mu - P_\mu \cos\theta_\mu) - m_\mu^2 \approx 4E_\nu P_\mu \sin^2\frac{\theta_\mu}{2}, \qquad (2.3)$$

$$x = \frac{Q^2}{2M_N \nu}, \qquad (2.4)$$

$$W^2 = M_N^2 - Q^2 + 2M_N \nu, \qquad (2.5)$$
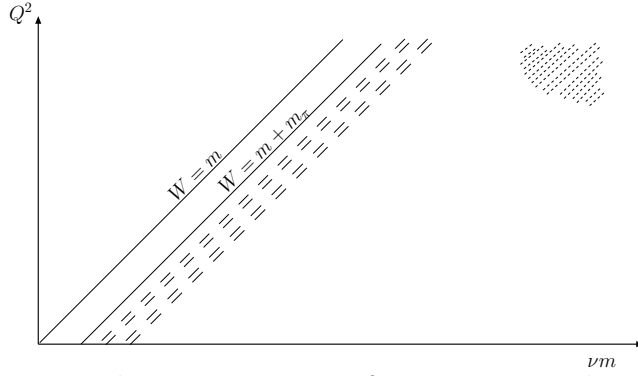
Figure 2.2: Distinct kinematic regions for neutrino-nucleon interactions.

where it is assumed that the target nucleon is at rest in the laboratory system, and the measured energy of the hadronic final state does not include the mass of the target nucleon. From Equation 2.5, it can be seen that W^2 is an explicit function of ν and Q^2. Distinct kinematic regions are shown in Figure 2.2 in the $(Q^2, \nu m)$ plane. The line $W = m$ corresponds to quasi-elastic scattering reactions: $\nu_\mu + n \rightarrow \mu^- + p$ and $\bar{\nu}_\mu + p \rightarrow \mu^+ + n$.

To the left of this line, the region is kinematically forbidden. The line $W = m + m_\pi$ traces the threshold of inelastic reactions of the type $\nu_\mu + N \rightarrow \mu^- + N + \pi$. Dashed lines corresponds to production of a number of hadronic resonances, for instance $\nu_\mu + p \rightarrow \mu^- + \Delta^{++}$. The hatched area gives the lower left-hand part of the deep-inelastic region. In this region, both ν and Q^2 are large and multiple production of hadrons takes places.

2.2 Quasi-elastic νN and $\bar{\nu} N$ Scattering

In the low energy approximation, the following interactions are possible:

- $\nu_\ell + n \rightarrow \ell^- + p,$

- $\bar{\nu}_\ell + p \rightarrow \ell^+ + n$

where ℓ can be τ or μ or e. The amplitude for this process can be found by using Feynman rules,

$$M = \frac{4G_F \cos\theta_c}{\sqrt{2}}[\bar{u}(\ell)\gamma^\mu \frac{1}{2}(1-\gamma_5)u(\nu_\ell)][\bar{u}(p)\gamma_\mu \frac{1}{2}\{F_v(q^2) + F_A(q^2)\gamma_5\}u(n)] \quad (2.6)$$

where F_v and F_A are form factors which appear since the proton and the neutron are not elementary particles. In the small regime of q^2, we take $q^2=0$. So the cross sections involve the vector and axial vector weak charges of the neutron and proton $g_v = F_v(0)$ and $g_A = F_A(0)$ respectively.

The conserved vector current hypothesis says that $g_v = 1$, whereas g_A has been measured to be 1.26 (Ref. [4]). For low energy neutrinos, $m_p \gg E \gg m_\ell$, the cross section is given by

$$\sigma(\nu n) = \frac{G_F^2}{\pi}(g_v^2 + 3g_A^2)E^2 \simeq 9.75 \times 10^{-42}(\frac{E}{10\text{MeV}})^2 cm^2. \quad (2.7)$$

The same expression also applies to $\bar{\nu} p$ scattering

$$\sigma(\bar{\nu} p) = \frac{G_F^2}{\pi}(g_v^2 + 3g_A^2)E^2 \quad (2.8)$$

2.3 Deep Inelastic Scattering of Neutrinos off Nucleons

In the previous section, we considered the kinematical region of $|q^2| \ll m^2{}_N$. Here, in contrast, we consider the region where $|q^2| \gg m_N^2$, but still $|q^2| \ll m_W^2$. The process is as follows, $\nu_\ell(k) + N(p) \to \ell^-(k') + X(p')$; the relevant diagram describing the charged current neutrino-nucleon interaction is shown in Figure 2.1. The cross section will have the general form

$$d\sigma^\nu \sim G_F^2 N_{\mu\nu} W^{\mu\nu}(q,p) \tag{2.9}$$

where $N_{\mu\nu}$ is the leptonic tensor ($\nu_\ell \to \ell$ transition) describing the interaction at the vertex of the neutrino and the W boson. The tensor $N_{\mu\nu}$, since it contains only information about the electroweak vertex, can be calculated exactly via Quantum Electrodynamics (QED) and the Glashow-Weinberg-Salam (GWS) theory of weak interactions. It is given by

$$N_{\mu\nu} = Tr[k\gamma_\mu(1 - \gamma_5)k\gamma_\nu(1 - \gamma_5)], \tag{2.10}$$

$$N_{\mu\nu} = 8\{k'_\mu k_\nu + k'_\nu k_\mu + \frac{q^2}{2}g_{\mu\nu} - i\epsilon_{\mu\nu\alpha\beta}k^\alpha k'^\beta\}. \tag{2.11}$$

In the approximation of small lepton masses,

$$q^\mu N_{\mu\nu} = q^\nu N_{\mu\nu}. \tag{2.12}$$

$W^{\mu\nu}$ is the hadronic tensor containing information about hadronic vertex. The $W^{\mu\nu}$ is a parametrization of an unknown quantity, interpreted in the parton

model as the precise distribution of partons inside the nucleus. It is deduced from Lorentz invariance, and depends on two vectors p and p', or alternatively on p and $q = p = p'$. This is given by

$$W^{\mu\nu} = -g^{\mu\nu}W_1 + \frac{p^\mu p^\nu}{m_N^2}W_2 - \frac{i\epsilon^{\mu\nu\lambda\rho}p_\lambda q_\rho}{2m_N^2}W_3 + \frac{q^\mu q^\nu}{m_N^2}W_4$$
$$+ \frac{(p^\mu q^\nu + p^\nu q^\mu)}{2m_N^2}W_5 + \frac{i(p^\mu q^\nu - p^\nu q^\mu)}{2m_N^2}W_6. \tag{2.13}$$

Here m_N is the nucleon mass, and W_1 to W_6 are form factors. All these form factors, being Lorentz scalars and can depend only on q^2 and $p.q$, since these are the only kinematical scalar variables. It is easy to see that the terms involving W_4, W_5 and W_6 are proportional to the charged lepton mass, and hence they are neglected. Then we have

$$W^{\mu\nu} = -g^{\mu\nu}W_1 + \frac{p^\mu p^\nu}{m_N^2}W_2 - \frac{i\epsilon^{\mu\nu\lambda\rho}p_\lambda q_\rho}{2m_N^2}W_3. \tag{2.14}$$

In the laboratory frame the cross section in terms of W_1, W_2, W_3 may be derived from

$$d\sigma^\nu = (\frac{G_F}{\sqrt{2}})^2 \frac{1}{4k.p} 4\pi M N_{\mu\nu} W^{\mu\nu} \frac{d^3k'}{2k'(2\pi)^3}. \tag{2.15}$$

In terms of the laboratory variables;

$$\frac{d^2\sigma^\nu}{dk'd\Omega} = G_F^2 \frac{k'^2}{2\pi^2}\{2\sin^2\frac{\theta}{2}W_1 + \cos^2\frac{\theta}{2}W_2 + \frac{k+k'}{M}\sin^2\frac{\theta}{2}W_3\}. \tag{2.16}$$

If we change the variables from (k', Ω) to (ν, Q^2) where $Q^2 = 2kk'(1 - \cos\theta)$ and $\nu = k - k'$, we obtain

$$\frac{d^2\sigma^\nu}{dQ^2d\nu} = \frac{G_F^2}{2\pi}\frac{k'}{k}\{2\sin^2\frac{\theta}{2}W_1 + \cos^2\frac{\theta}{2}W_2 + \frac{k+k'}{M}\sin^2\frac{\theta}{2}W_3\}. \tag{2.17}$$

11

For an incoming antineutrino beam, we get

$$\frac{d^2\sigma^{\bar{\nu}}}{dQ^2 d\nu} = \frac{G_F^2}{2\pi}\frac{k'}{k}\{2\sin^2\frac{\theta}{2}W_1 + \cos^2\frac{\theta}{2}W_2 - \frac{k+k'}{M}\sin^2\frac{\theta}{2}W_3\}. \qquad (2.18)$$

In general, the structure functions W_i depend on the target and on the neutrino helicity. In terms of the absorption cross sections for left-handed, right-handed, and scalar W bosons $(\sigma_L, \sigma_R, \sigma_S)$ the structure functions can be written as:

$$W_1 = \frac{K}{\pi G_F \sqrt{2}}(\sigma_R + \sigma_L), \qquad (2.19)$$

$$W_2 = \frac{K}{\pi G_F \sqrt{2}}\frac{Q^2}{Q^2 + \nu^2}(\sigma_R + \sigma_L + 2\sigma_S), \qquad (2.20)$$

$$W_3 = \frac{K}{\pi G_F \sqrt{2}}\frac{2m_N}{\sqrt{Q^2 + \nu^2}}(\sigma_R - \sigma_L), \qquad (2.21)$$

where K represents the flux of virtual W_S. The ratio of absorption cross sections for longitudinally to transversely polarized bosons is defined as:

$$R(\nu, Q^2) \equiv \frac{\sigma_S}{\sigma_T} = \frac{W_2}{W_1}(1 - \frac{\nu^2}{Q^2}) - 1. \qquad (2.22)$$

For high Q^2, $Q^2 \to \infty$, and $\nu, \nu \to \infty$, that is in the range of Bjorken scalling invariance, the structure functions notations can be written as a functions of a single dimensionless variable $x = \frac{Q^2}{2M\nu}$,

$$MW_1^{\nu}(Q^2, \nu) \to F_1^{\nu}(x), \qquad (2.23)$$

$$\nu W_2^{\nu}(Q^2, \nu) \to F_2^{\nu}(x), \qquad (2.24)$$

$$\nu W_3^{\nu}(Q^2, \nu) \to F_3^{\nu}(x), \qquad (2.25)$$

12

where F's are finite. In terms of the scaling variables $x = \frac{Q^2}{2M\nu}$, $y = \frac{\nu}{k}$ and Q^2, the cross section in neutrino scattering (Equation 2.18) may be written in the form,

$$\frac{d^2\sigma^{\nu(\bar{\nu})}}{dxdy} = \frac{G_F^2 Mk}{\pi}(\frac{y^2}{2}2xF_1^{\nu(\bar{\nu})} + (1 - y - \frac{Mxy}{2k})F_2^{\nu(\bar{\nu})} \pm (y - \frac{1}{2}y^2)xF_3^{\nu(\bar{\nu})}). \quad (2.26)$$

If we assume the Callan-Gross relation

$$2xF_1^{\nu} = F_2^{\nu} \qquad (2.27)$$

then

$$\frac{d^2\sigma^{\nu}}{dxdy} = \frac{G_F^2}{2\pi}s(F_2^{\nu}\frac{1 + (1 - y)^2}{2} - xF_3^{\nu}\frac{1 - (1 - y)^2}{2}) \qquad (2.28)$$

in terms of the Bjorken scaling variables.

The validity of Callan-Gross relation, Equation 2.27, indicates that the partons are spin-1/2 particles. Callan-Gross relation is explained by the vanishing of the longitudinally polarized virtual boson-parton scattering cross section. For spin-1/2 massless particles, such an interaction violates the helicity conservation. As a consequence of the Bjorken scaling phenomenon, and the validity of Callan-Gross relation to a good approximation, we identify the spin-1/2 point-like nucleon constituents as quarks. In the framework of the four-quark (u, d, s, c) parton model, the structure functions depend only on one variable, expressed in terms of the distributions over the fraction x of the momentum of the quarks and antiquarks in the nucleon:

$$F_2^{\nu N}(x) = q(x) + \bar{q}(x), \qquad (2.29)$$

13

$$xF_3^{\nu N}(x) \quad = \quad xq(x) - x\bar{q}(x) + 2x[s(x) - c(x)], \qquad (2.30)$$

$$2xF_1^{\nu N}(x) \quad = \quad F_2^{\nu N}(x), \qquad (2.31)$$

where

$$q(x) = x[u(x) + d(x) + s(x) + c(x)], \qquad (2.32)$$

$$\bar{q}(x) = x[\bar{u}(x) + \bar{d}(x) + \bar{s}(x) + \bar{c}(x). \qquad (2.33)$$

Inserting Equation 2.29, 2.30 in Equation 2.28, we obtain the cross section form

in terms of quark distributions,

$$\frac{\partial^2 \sigma_{CC}^{(\nu N)}}{\partial x \partial y} = \frac{G_F^2}{\pi} s[q(x) + (1 - y^2)\bar{q}(x)]. \qquad (2.34)$$

For the antineutrino interaction,

$$\frac{\partial^2 \sigma_{CC}^{(\bar{\nu} N)}}{\partial x \partial y} = \frac{G_F^2}{\pi} s[\bar{q}(x) + (1 - y^2)q(x)]. \qquad (2.35)$$

Integrating independently Equation 2.34 over y and x between zero and one, we

get the differential cross sections for neutrino scattering from a nucleon:

$$\frac{d\sigma_{CC}^{(\nu N)}}{dx} = \frac{G_F^2}{\pi} s[q(x) + \frac{1}{3}\bar{q}(x)], \qquad (2.36)$$

$$\frac{d\sigma_{CC}^{(\nu N)}}{dy} = \frac{G_F^2}{\pi} s \int F_2^{\nu N}(x) dx [\frac{1+B}{2} + \frac{1-B}{2}(1 - y^2)], \qquad (2.37)$$

where

$$B = \frac{\int (q - \bar{q}) dx}{\int (q + \bar{q}) dx} = \frac{\int x F_3^{\nu N}(x) dx}{\int F_3^{\nu N}(x) dx}. \qquad (2.38)$$

This parameter characterizes the relative contribution of the valence quarks to

the cross section.

14

The total cross section of the neutrino(antineutrino) interaction increases linearly with neutrino energy: $\sigma = \sigma_0 E_\nu$. Equation 2.34 also suggests that for an isoscalar target with equal number of up quarks and down quarks the total cross section for neutrinos is three times as large as the antineutrino cross section since $\int (1 - y^2) dy = 1/3$. The true ratio is slightly smaller due to the presence of sea quarks within the nucleons. The experimental results from different experiments are shown in Figure 2.3. The average value of σ_0 for the charged current cross section for neutrinos is $0.677 \pm 0.014 \times 10^{-38} cm^2/\mathrm{GeV}$ and for antineutrinos is $0.334 \pm 0.008 \times 10^{-38} cm^2/\mathrm{GeV}$ [6].
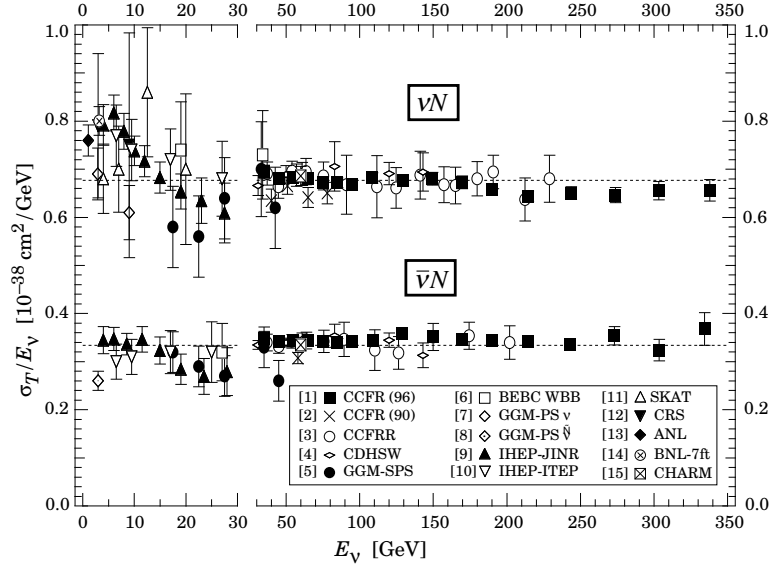
Figure 2.3: σ_T/E_ν, for the muon neutrino and antineutrino charged current total cross section as a function of neutrino energy. The error bars include both statistical and systematic errors. The straight lines are the averaged values over all energies as measured by the experiments in Refs [7, 8, 9, 10] = $0.677 \pm 0.014(0.334 \pm 0.008) \times 10^{-38}$ cm^2/GeV. There is a change in the energy scale at 30 GeV.

2.4 Charm Production by Neutrino Charged Current Interaction

In the charged current interaction neutrino interacts with the "valence" d quark or the "sea" s quark to produce c quark. In the antineutrino case there are no allowed transitions from valence quarks. The strongest contribution is from the transition of $\bar{s}$ antiquark into a $\bar{c}$ antiquark. There is also a transition of $\bar{d}$ from the sea into a $\bar{c}$ antiquark, which is Cabibbo-suppressed. Then by hadronization process, c quark ($\bar{c}$ antiquark) "dresses" itself with other quarks or antiquarks from "valence" and "sea" quarks of the interacting nucleon so then a charmed valence(anticharmed) hadron is produced. Figure 2.4 shows charm production by neutrino and antineutrino deep-inelastic scattering.
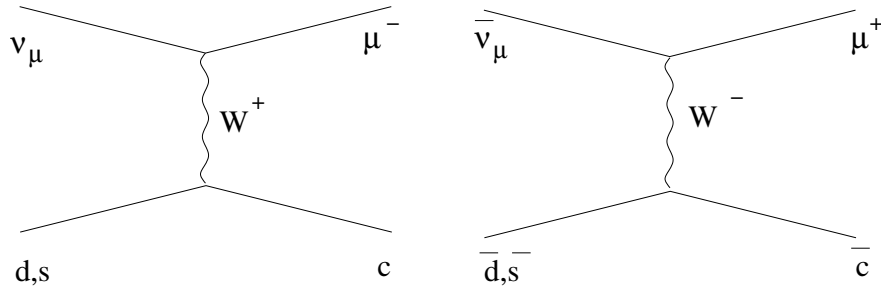
Figure 2.4: Charm production by **Left:** neutrino and **Right:** antineutrino CC interaction.

Let us consider the semi-inclusive process

$$\nu_\mu N \to \mu^- c X$$

where X is a hadronic final state, and for the moment we neglect the hadronization of the final c quark.

Defining

$$2xF_1^c(x) = xF_3^c(x) = |V_{cd}|^2 xd(x) + |V_{cs}|^2 xs(x) \qquad (2.39)$$

where V_{cd} and V_{cs} are CKM-matrix elements [11, 12].

At partonic level, the relevant processes for c production are [13]

$$\nu_\mu d \to \mu^- c \qquad \frac{d\sigma(\nu_\mu d \to \mu^- c)}{dy} = \frac{G_F^2 \hat{s}}{\pi}(1 - \frac{m_c^2}{\hat{s}})|V_{cd}|^2, \qquad (2.40)$$

$$\nu_\mu s \to \mu^- c \qquad \frac{d\sigma(\nu_\mu s \to \mu^- c)}{dy} = \frac{G_F^2 \hat{s}}{\pi}(1 - \frac{m_c^2}{\hat{s}})|V_{cs}|^2. \qquad (2.41)$$

The production of c quark through $\nu_\mu d$ scattering is Cabibbo suppressed ($|V_{cd}|^2 \sim \sin^2\theta_c \simeq 0.04$), while the production through $\nu_\mu s$ scattering ($|V_{cs}|^2 \sim \cos^2\theta_c \simeq 0.96$) is instead suppressed by the low abundance of s quarks in the sea.

If $\hat{p} = \xi p$ is the parton four-momentum, if a c quark is produced in the final state, and neglecting the initial parton mass ($m_d, m_s \ll m_c$), we have

$$m_c^2 = (\hat{p} + q)^2 = -Q^2 + 2\xi p.q = -Q^2 + \frac{\xi Q^2}{x}. \qquad (2.42)$$

The parton distribution will be probed at

$$\xi = x(1 + \frac{m_c^2}{Q^2}) \qquad (2.43)$$

which is called the *slow rescaling* variable [14, 15].

17

The cross section for charm production induced by neutrino scattering off an isoscalar target T then reads

$$\frac{d^2\sigma(\nu_\mu T \rightarrow \mu^- cX)}{dxdy} = \frac{G_F^2 s\xi}{2\pi}[(u(\xi) + d(\xi))|V_{cd}|^2 + 2s(\xi)|V_{cs}|^2](1 - \frac{m_c^2}{s\xi})\theta(\xi - \frac{m_c^2}{s}).$$

(2.44)

Since $\hat{s} = (\xi p + k)^2 \simeq \xi s$, we can replace the kinematic factor $(1 - \frac{m_c^2}{s\xi})$ in Equation 2.44, with $(1 - \frac{m_c^2}{\hat{s}})$, and with the further assumption $s(x) = \bar{s}(x) = c(x) = \bar{c}(x)$, we get

$$\frac{\sigma(\nu_\mu T \rightarrow \mu^- cX)}{\sigma(\nu_\mu T \rightarrow \mu^- X)} \simeq \frac{(U + D)|V_{cd}|^2 + 2S|V_{cs}|^2}{U + D + 2S + \frac{1}{3}(\bar{U} + \bar{D} + 2\bar{S})}(1 - \frac{m_c^2}{\hat{s}})$$

(2.45)

where

$$Q = \int_0^1 xq(x)dx, \qquad Q = U, D, S$$

(2.46)

is the fraction of nucleon's momentum carried by q quarks.

Using the world average, we assume

$$\eta_s := \frac{2S}{U + D} = 0.061 \pm 0.004,$$

(2.47)

$$\kappa := \frac{2\bar{S}}{\bar{U} + \bar{D}} = 0.40 \pm 0.05,$$

(2.48)

where the η_s and κ are the strangeness and antistrangeness of the sea. Then for $E_{\nu_\mu} = 20$ GeV, we obtain

$$\frac{\sigma(\nu_\mu T \rightarrow \mu^- cX)}{\sigma(\nu_\mu T \rightarrow \mu^- X)} \simeq \frac{6}{10}\frac{\frac{1}{\eta_s}|V_{cd}|^2 + |V_{cs}|^2}{\frac{1}{\eta_s} + 1 + \frac{1}{3}(\frac{1}{\kappa} + 1)}$$

(2.49)

$$\simeq 0.056 \pm 0.008.$$

(2.50)

That means about 6% of all charged current interaction have a charm quark in the final state.

2.5   Charm Quark Hadronization

The ν_μCC interaction can produce a single charm quark in the final state. However, single bare quarks have not been observed; the charm quark forms hadronic states through its binding to virtual quarks and antiquarks, mediated by gluon exchange. All of the nonperturbative processes that act to "dress" the charm quark so that it emerges as a hadron are known as fragmentation or hadronization processes. All fragmentation models define a fragmentation parameter $z = \frac{p_h}{p_h^{max}}$. It describes the fraction of the momentum p_h carried by a hadron with respect to the maximum momentum p_h^{max} of hadrons (i.e. the momentum of the quarks). It is allowed kinematically, at the same E_ν, Q^2 and x.

Assuming factorization, the charmed hadron cross section in (anti)neutrino-nucleon interaction can be connected to the charmed quark cross section via fragmentation functions:

$$\frac{d\sigma(\nu N \to \mu^- CX)}{dxdydzdp_T^2} = \frac{d\sigma(\nu N \to \mu^- cX)}{dxdy} \cdot \sum_h f_h . D_c^h(z, dp_T^2), \qquad (2.51)$$

$$\frac{d\sigma(\bar\nu N \to \mu^+ \bar C X)}{dxdydzdp_T^2} = \frac{d\sigma(\bar\nu N \to \mu^+ \bar c X)}{dxdy} \cdot \sum_h \bar f_h . \bar D_{\bar c}^h(z, dp_T^2) \qquad (2.52)$$

where $D_c^h(z, dp_T^2)$ is the probability distribution for the charmed quark fragment-ing into a charmed hadron of type h carrying a fraction of the quark's longitudinal momentum z and transverse momentum p_T with respect to the quark direction. Moreover, f_h is the mean multiplicity of the hadron h in neutrino production of charm. The barred quantities indicate antineutrino charm production. So, $D_c^h(z, dp_T^2)$ and f_h are normalized as

$$\int_0^1 dz \int_0^\infty dp_T^2 D_c^h(z, dp_T^2) = \int_0^1 dz \int_0^\infty dp_T^2 \bar{D}_{\bar{c}}^h(z, dp_T^2) = 1, \qquad (2.53)$$

and

$$\sum_h f_h = \sum_h \bar{f}_h = 1. \qquad (2.54)$$

The analytical form of the fragmentation function depends on the quark mass. For light quarks (u, d and s), the Lund parameterization [16] is mostly used, with

$$D_L(z) \propto \frac{1}{z}(1 - z)^a e^{-bm_\perp/z} \qquad (2.55)$$

where $m_\perp = \sqrt{m^2 + p_\perp^2}$ is called transverse mass, a and b are parameters of order 0.3 and 0.58 GeV^{-2}, respectively.

For heavy quarks two alternative parametrizations are available. The Collins-Spiller [17] function

$$D_{CS}(z) \propto (\frac{1 - z}{z} + \frac{\epsilon_{CS}(2 - z)}{1 - z})(1 + z)^2(1 - \frac{1}{z} - \frac{\epsilon_{CS}}{1 - z})^{-2} \qquad (2.56)$$

and the Peterson [17] function

$$D_p(z) \propto \frac{1}{z}(1 - \frac{1}{z} - \frac{\epsilon_P}{1 - z})^{-2} \qquad (2.57)$$

where ϵ's are free parameters. The ϵ_P parameter will be different for different mesons, but can be expected to scale as $1/m_c^2$, with m_c the mass of the charmed hadron.

During the fragmentation process, the emerging hadron acquires a momentum component transverse to the original direction of the charm quark with a distribution of the type

$$\frac{dN}{dp_\perp^2} \propto e^{-\beta p_\perp^2}. \tag{2.58}$$

The parameter β was measured by LEBC EHS [18] as $\beta = 1.1 \pm 0.3$ corresponding to $\langle p_\perp^2 \rangle = 0.9 \pm 0.2 \text{GeV}^2$.

2.6   Pentaquark Hadrons

Our present understanding of hadrons as bound states of quarks is based on Quantum Chromodynamics, a non-Abelian gauge theory using Yang-Mills fields [19]. Quantum Chromodynamics (QCD) is believed to be the underlying theory of the strong interaction. Quark model which is based on QCD, is widely used to classify hadrons, calculate static properties and low energy reactions. According to the quark model, mesons are composed of a pair of quark and antiquark while baryons are composed of three quarks. Besides conventional mesons and baryons, QCD does not exclude the existence of the "nonconventional", "nonstandard" or "exotic" hadrons with quark content other than $q\bar{q}$ or qqq as long as they are colorless. Some examples are glueballs (gg,ggg,...), hybrid states ($q\bar{q}$g or qqqg),

multiquark mesons ($qq\overline{qq}$), multiquark baryons ($qqqq\overline{q}$) and dibaryons ($qqqqqq$).

A very important question is whether there exist in nature baryon states constructed from more complicated quark configurations, such as pentaquark. Why is the Pentaquark important? Observation of the pentaquark is very interesting because of its unusual structure and would contribute to the understanding of QCD in the nonperturbative regime and for the concept of confinement.

The possible existence of multiquark states, H (dibaryon which was a six quark state), particle was suggested by Jaffe with MIT bag model [20] as early as 1977. Unfortunately it was not found experimentally. In the past years there has accumulated some experimental evidence of possible existence of glueballs and hybrid mesons with exotic quantum numbers like $J^{PC} = 1^{-+}$ [21].

Speculations regarding multiquark baryon states has appeared in the literature for more than 30 years, initially in connection with $K - N$ scattering data [22]. These states, initially referred to as Z^* resonances, were included in the Particle Data Group (PDG) listings until 1986. In 1988 review the Particle Data Group officially put the subject to sleep [23]:

> "The general prejudice against baryons not made of three quarks and
> the lack of any experimental activity in this area make it likely that
> it will be another 15 years before the issue is decided."

After that, the subject of exotic baryons did not receive much attention. And then they were dropped due to a lack of convincing experimental evidence.

Diakonov *et al.* [24] proposed in a 1997 paper, on the basis of a chiral soliton

model, the existence of a low mass antidecuplet of such multiquark baryons, with spin-1/2 and even parity, and with specific estimates for the masses and widths. The earlier predictions on the pentaquark masses range form 1500 to 1800 MeV, with about a hundred MeV width. They did not give specific values for the mass or the width, while Diakonov *et al.* made very specific and testable predictions.

2.7 Theoretical Model of Pentaquark

After the experimental observations of pentaquarks, a lot of theoretical models have been proposed for the pentaquark masses. The mass of the anticharmed pentaquark $\Theta_c^0(uudd\bar{c})$ has been estimated using various methods:

- Jaffe and Wilczek [25] estimated by using the diquark-diquark-antiquark model, that $m(\Theta_c^0) = 2710$ MeV,

- Skyrme model [27] yields $m(\Theta_c^0) = 2704$ MeV,

- Cheung [28] obtained by assuming the color spin interaction as the dominant mechanism for hyperfine splitting that $m(\Theta_c^0) = (2985 - 2997)$ MeV,

- Karliner and Lipkin [29] found by using diquark-triquark model, that $m(\Theta_c^0) = 2985 \pm 50$ MeV,

- A lattice calculation by Sasaki [30] leads to $m(\Theta_c^0) = 3445$ MeV,

- Lattice QCD calculation [31] with exact chiral symmetry predicts a mass of $m(\Theta_c^0) = 2977 \pm 109$ MeV.

The mass of the pentaquark is a very important parameter, since the decay modes of the pentaquark depends on its mass. If the pentaquark has a large mass, $M(\Theta_c^0) > M(D^-) + M(N)$, it would decay strongly to substructure particles. If the pentaquark mass is below the threshold then it would decay weakly. The low production rate of this state might be traced back to the unlikely hadronization of a $\bar{c}$ quark with four light quarks. Consequently, it is relevant to study the weak decays of charmed pentaquarks.

In the following section, the chiral soliton model which gives a specific estimation for the masses and decay widths of the pentaquark, and Jaffe-Wilczek model which gives low mass of Θ_c^0 will be discussed.

2.7.1 The Chiral Soliton Model

Diakonov *et al.* [24] proposed, the existence of a low mass antidecuplet of such multiquark baryons, with spin-1/2 and even parity, and with specific estimates for the masses and widths. These estimations came within the chiral soliton model, which is based on the skyrme model [32, 33], where the nucleons can be interpreted as solitons of the pion field. It is strictly true only in the limit of a fictional world where the numbers of colors in QCD goes to infinity (the large N_c model [34]). The classification of the light baryons as the rotational states of the

soliton is the strength of the model.

The energy eigenvalues of such a rotation are quantized and the rotational Hamiltonian is described in terms of the SU(3) generators. The result of the chiral soliton model is a set of states with mass determined by the given group structure and the splitting of the light quark and strange quark masses. The lowest rotational state corresponds to an octet with spin-1/2, the next highest rotational state is a decuplet with spin-3/2. These states are identified by the lowest mass baryon octet and decuplet. In this model next rotational excitation of solitons is considered. The next excitation in the three flavour case should be an antidecuplet with spin-1/2 (a decuplet with opposite symmetry, written as $\overline{10}$). They identified known nucleon resonance N(1710) as a member of the antidecuplet. The scheme of the antidecuplet is shown in the Figure 2.5. The
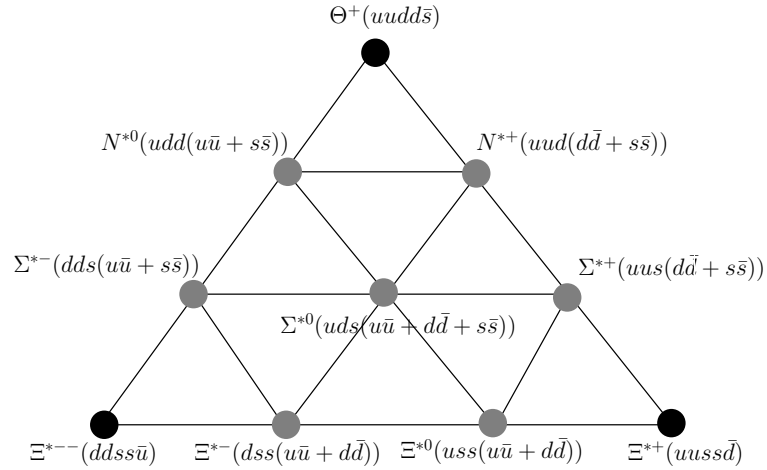
Figure 2.5: Antidecuplet of baryons. The corners of this diagram are exotic.

candidates, located at the corners of triangle, are exotic pentaquarks, since the antiquark has a different flavor than the other quarks. While the other members of antidecuplet are not exotic.

2.7.2 Jaffe-Wilczek Model

In the model of Jaffe-Wilczek [25, 26], the pentaquark states consist of an antiquark $(\bar{q})$, and two diquark pairs (qq). Each diquark is in state of spin 0, $\bar{3}$ color, and $\bar{3}$ of flavor.

If we ignore color and approximate the diquarks as point particles, the two are identical bosons; thus their wave function must be symmetric in spin and flavor in order to obey Bose statistics. However, the overall wave function of the pentaquark must be completely antisymmetric according to Fermi statistics.

Jaffe and Wilczek suggested that the charm analogs of Θ^+ may be stable against strong decays. They estimated the mass of the Θ_c^0 by comparing the masses of the $\Lambda(1116)$, and $\Lambda_c(2285)$. The $[ud]$ diquark in the Λ and Λ_c are coupled to color $\bar{3}$ and spin zero. So the diquark provides an environment for s quark nearly identical to the environment of the $\bar{s}$ in the Θ^+. If we assume that hyperfine effects for the s quark in Λ are similar to those for $\bar{s}$ in Θ^+, the mass of the Θ_c^0 can be estimated as

$$M(\Theta_c^0) \approx M(\Theta^+) + M(\Lambda_c) - M(\Lambda) \approx 2710 \ MeV \qquad (2.59)$$

100 MeV below the threshold for strong decay into DN.

26

In our analysis the mass of the Θ_c^0 is assumed to be 2.7 GeV/c^2. Therefore, we will focus on weakly decaying charmed pentaquarks.

CHAPTER 3

THE CHORUS EXPERIMENT

The CHORUS (CERN Hybrid Oscillation Research apparatUS) experiment was designed to search for $\nu_\mu \to \nu_\tau$ oscillations via the direct observation of the decay of the τ lepton produced in the interaction $\nu_\tau N \to \tau^- X$ and the subsequent τ decay into a muon or a negative hadron. Since the lifetime of charm particles is similar to that of the τ lepton, it is also possible to study charm particles in the CHORUS experiment.

For CHORUS, a "hybrid" detector system was adopted [35], with a target/tracker of nuclear emulsions, together with electronic detectors. Electronic detectors help to reconstruct the event kinematics and nuclear emulsions are used as an active target and to observe the decay topology. As illustrated in the Figure 3.1, the CHORUS detector set-up consists of the emulsion target, a trigger system, a scintillating fiber tracker, an air-core magnet, an electromagnetic and hadronic calorimeter, and a muon spectrometer. A detailed description of all the elements of the detector system can be found in Ref. [35].
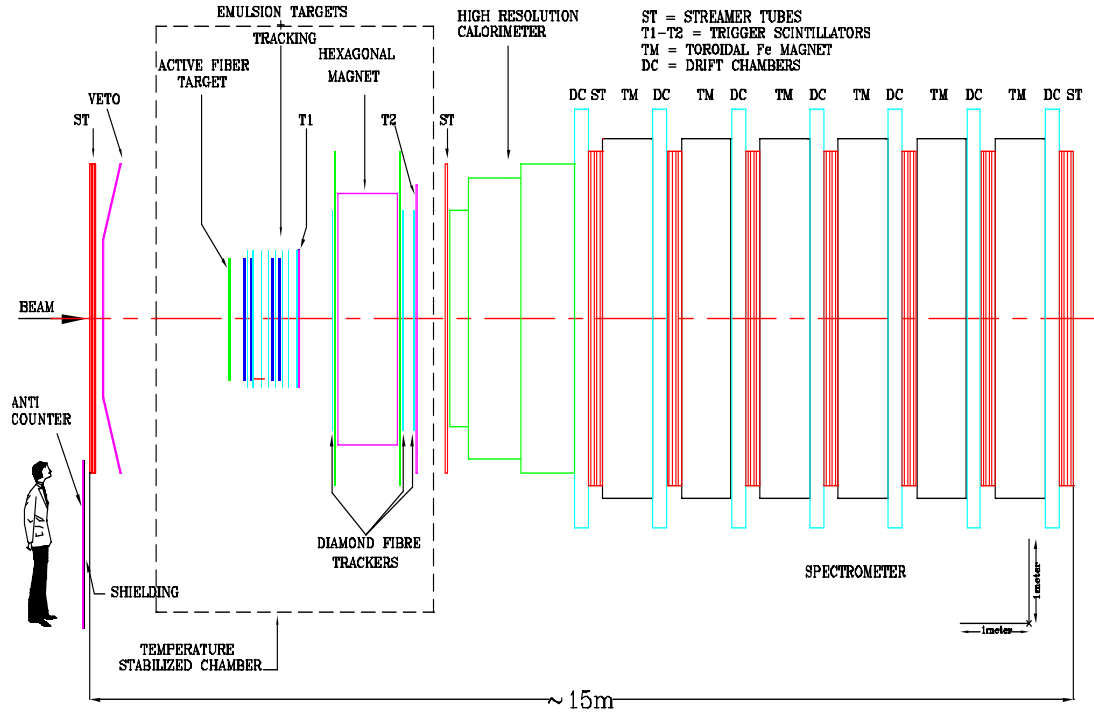
Figure 3.1: The CHORUS detector.

3.1   The Neutrino Beam

The West Area Neutrino Facility (WANF) of the CERN Super Proton Synchrotron (SPS) [36] provides a ν_μ beam with a mean energy of 27 GeV well above the tau and charm production thresholds. A schematic overview of the beam line is shown in the Figure 3.2.

The SPS accelerates protons from the Proton Synchrotron (PS) to an energy of about 450 GeV. The acceleration cycle is repeated every 14.4s. After the acceleration, protons are extracted in two 6ms long spills, separated in time by

29

2.7s, and then are directed onto the beryllium target composed of a succession of 11 beryllium rods of 10 cm length and 3 mm diameter, separated by 9 mm gaps. The proton-beryllium interaction produces mainly pions and kaons. These positive(negative) mesons are focused (defocused) by two magnetic lenses, the horn and the reflector. The horn and the reflector consist of a 7 m long aluminum cylinder, with an inner cylinder of conical shape. The outer diameter of the horn is 40 cm, while the reflector has an outer diameter of 80 cm. Helium bags are positioned in the space between the horn and the reflector, and downstream of the reflector, in order to minimize the number of hadronic re-interactions of the pions and kaons.

The mesons decay in flight in a 290 m long vacuum tunnel and produce muonic neutrinos mainly via the decay channels:

$$\pi^+ \rightarrow \mu^+ \nu_\mu, \qquad (BR : 99.9\%)$$

$$K^+ \rightarrow \mu^+ \nu_\mu, \qquad (BR : 63.5\%)$$

$$K^+ \rightarrow \pi^0 \mu^+ \nu_\mu \qquad (BR : 3.2\%).$$

The protons, which did not interact in the target, the charged leptons or hadrons from the meson decay and the surviving π^+ or K^+ are all absorbed in a shielding composed of 225 m of iron and 144 m of earth. Finally, a toroidal magnet defocuses not stopping muons.

The beam line has an upward slope of 42 mrad. The detector parts are

centered along this slope, however, every part is placed vertically. The dominant component of the beam is ν_μ, with an unavoidable contamination of $\bar{\nu}_\mu$, since negative hadrons not defocused by the magnets, and a 1% of ν_e and $\bar{\nu}_e$ mainly coming from three body decays of kaons. The prompt ν_τ component, coming from D_s^+ which is produced in the production target and in the beam-dump, decays into τ is estimated to be 3.3×10^{-6} charged current interactions for every ν_τ charged current interaction [37]. The energy spectra of the components by GBEAM [38] utility is shown in Figure 3.3 and the relative abundance of the different neutrino flavours in the beam is given in Table 3.1.
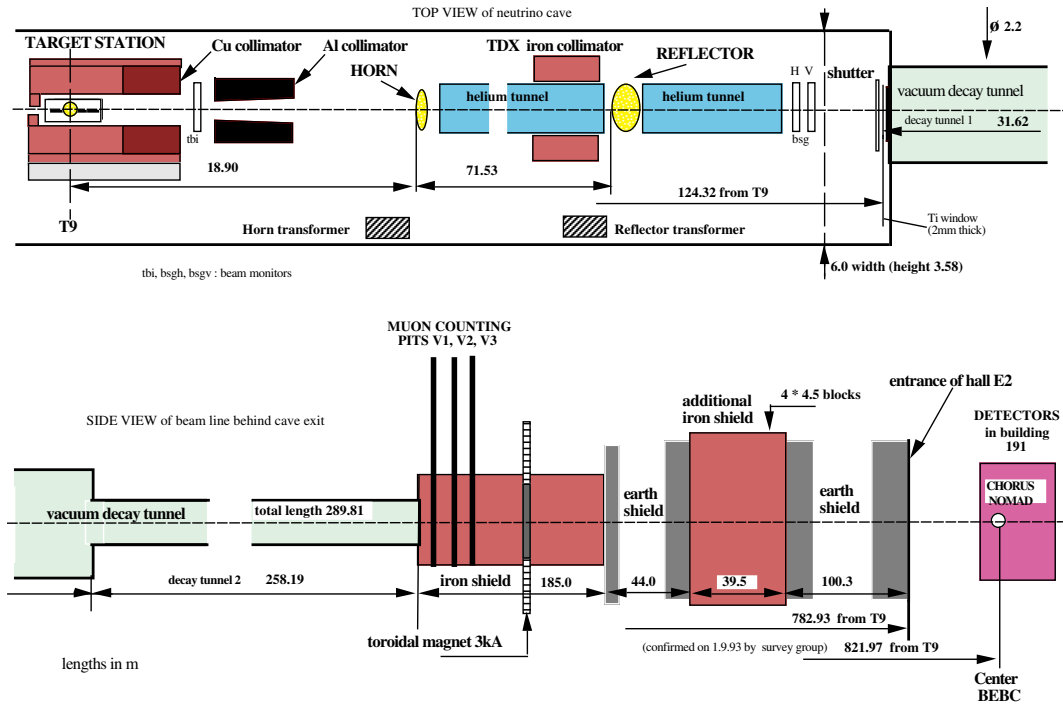
Figure 3.2: Schematic overview of the WANF neutrino beam-line.

31
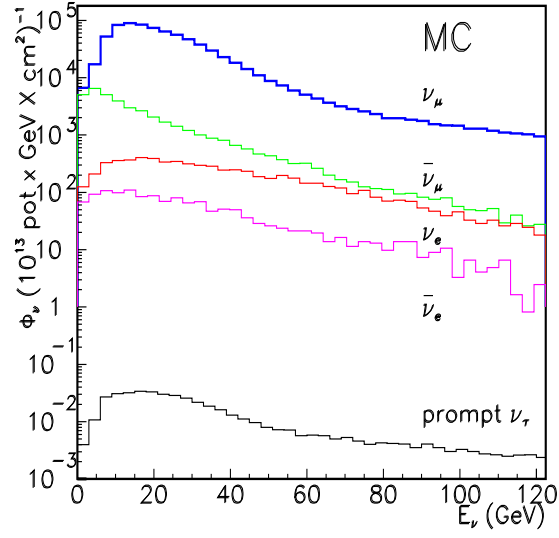
Figure 3.3: Neutrino beam energy spectrum.

Table 3.1: Relative composition of the CHORUS neutrino beam.

Neutrino type	Relative Abundance	$< E >$(GeV)
ν_μ	100%	26.9
$\bar{\nu}_\mu$	5.6%	21.7
ν_e	0.7%	47.9
$\bar{\nu}_e$	0.17%	35.3

Muon antineutrino contamination primarily results from K^0 decays and the remaining π^-, K^- components in the beam. And also due to focalization of positive secondaries, most of muons in the beam are positive and contribute to the $\bar{\nu}_\mu$ contamination. The contamination of muon antineutrino is $\sim 6\%$ and the mean energy is $< E_{\bar{\nu}_\mu} > \simeq 18$ GeV. Figure 3.4 shows the energy spectrum of the antineutrino component beam as obtained by simulation. The neutrino exposure
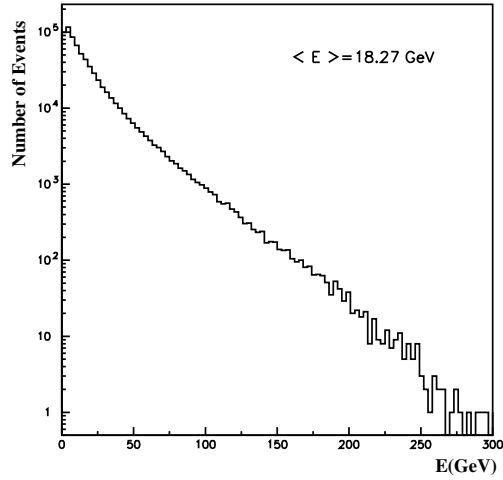
Figure 3.4: Energy spectrum of the antineutrino component of the beam.

started in 1994 and ended in 1997. In these four years of data taking, emulsions have been exposed to the neutrino beam with an intensity corresponding to 5.06×10^{19} protons on target. CHORUS ran also in 1998, without emulsions, with a neutrino and antineutrino beam, using the calorimeter as target for compared analysis of cross-section νN and $\bar{\nu}$N [39].

3.2 The Emulsion Target

Nuclear emulsions provide the three dimensional reconstruction of a track with a resolution of the order of 1 μm, being ideal for the study of interactions including short lived particles, like tau lepton and charm hadron.

CHORUS emulsions are made of microcrystals of silver halides ($AgBr$) dispersed in a gelatine layer, the composition of the CHORUS emulsion is shown in Table 3.2. When a charged particle passes through nuclear emulsion, it forms a latent image by ionizing the $AgBr$ crystals along its trajectory. After suitable chemical processing of the emulsion such ionization sites induce the deposition of Ag atoms as dark spots (grains) thus making the trajectory of the charged particle visible. The grain size ranges from 0.2 to 0.6 μm, and there are on average 300 grains per mm of track length.

CHORUS emulsion set-up consists of two components: a massive emulsion target where the neutrino interactions are recorded, also called the "bulk", and thin emulsion sheets used to interface the tracks reconstructed by the fibre tracker and the emulsion target. The volume of the emulsion target is 206 l, corresponding to 770 kg. It is divided into four stacks, each stack corresponding to 1 radiation length and to 0.08 interaction lengths. Each stack has a surface of $1.42 \times 1.42\ m^2$, and thickness of 2.8 cm. They are subdivided into 8 sectors of $0.71 \times 0.36\ m^2$ each formed by 36 plates. The plates consist of 350 μm of emulsion gel poured

onto the two of the faces of a 90 μm depth plastic base. The interface sheets are composed by a 800 μm thick plastic base and two gel layers of 100 μm depth. The different emulsion and base thicknesses of the CS/SS sheets with respect to the bulk plates are due to the necessity to maximize the angular resolution to match the electronic detector track with the emulsion track. In fact the interface sheets have a larger level arm and less distortion due to the shrinkage of the emulsion during its development. They were inserted in order to make predictions on track location in emulsion, so the first sheet, called "special" is after the emulsion stack, while the remaining two, called "changeable", are positioned in front of the first tracker plane downstream the stack, in order to minimize the error on extrapolation of the tracks from target tracker.

In order to provide favourable background conditions for the recognition of the predicted tracks in the emulsions, in the 1994-95 data taking the changeable sheets were replaced every three to six weeks during the data taking. In 1996-97 exposure only one change per year have been done.

3.3   The Scintillating Fiber Tracker

The scintillating fiber tracker [41, 42, 43] provides tracking and vertex reconstruction, with the accuracy needed for the extrapolation of tracks to the upstream interface sheet.

When a charged particle crosses a scintillating fiber, photons are emitted in

Table 3.2: Atomic composition of nuclear emulsions (Fuji ET-B7) used in the CHORUS experiment [40].

Element	Atomic number	Mass (%)	Mole fraction (%)
Iodine (I)	53	0.3	0.06
Silver (Ag)	47	45.5	11.2
Bromine (Br)	36	33.4	11.1
Sulfur (S)	16	0.2	0.2
Oxygen (O)	8	6.8	11.3
Nitrogen (N)	7	3.1	5.9
Carbon (C)	6	9.3	20.6
Hydrogen (H)	1	1.5	40.0
Mean number of nucleons		36 protons, 45 neutrons	
Density		3.73 g/cm^3	
Radiation length		2.94 cm	
Nuclear interaction mean free path		38 cm	
Concentration of $AgBr$		45.5% in volume	

the fiber. Then the photons are collected and sent to photomultipliers and to the optoelectronic chain capable to read the signal. The CHORUS target tracker system was built assembling more than 1 million plastic scintillating fibers of 500 μm, 2.3 m length and with a 3.2 mm total thickness. The layers of the fiber ribbons are glued with a TiO_2 based paint which also reduces cross talk.

The target tracker is composed of eight modules. The first module is positioned downstream the first emulsion stack, the following three are downstream the second stack etc. as shown in Figure 3.5. The 40 mm distance of a stack from the downstream tracker plane optimizes the upward extrapolation. It maintains a good track separation. Every module is composed of four planes, measuring the two transverse coordinates Y, Z and two orthogonal stereo projections $Y^{\pm}$,

$Z^{\pm}$ rotated by $\pm 8^o$ with respect to Y and Z, to eliminate ambiguities on the tridimentional track reconstruction.
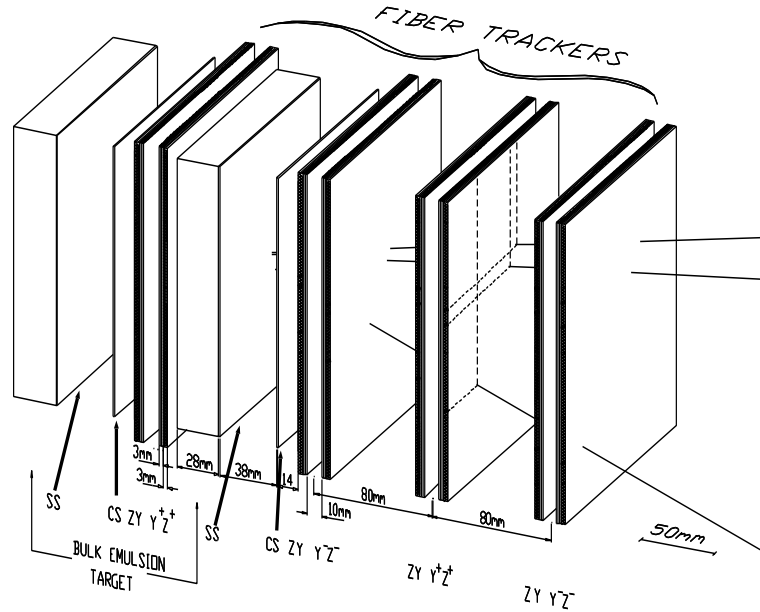
Figure 3.5: The geometry of half of the target region, showing the target emulsion stacks and the interfaces sheets and the target trackers.

The readout is composed of 58 optoelectronic chains, each made up by four image intensifiers and a CCD camera. A maximum number of two events for spill could be recorded. The prediction accuracy was measured as $\sigma \sim 150\ \mu m$ in position and $\sigma \sim 2.5\ mrad$ in angle [42].

3.4   The Air Core Magnet

The sign and momentum of particles are determined by the Air Core Spectrometer before they enter the calorimeter. It is also employed to determine the

momentum of the muons that don't reach the muon spectrometer. This is a very unusual spectrometer: it has no iron-core magnet. It consists of an air core magnet with a toroidal field and fiber tracker planes.

The magnet has a hexagonal shape [45], as shown in Figure 3.6. It is made of six equilateral triangles with 1.5 m sides, 0.75 m depth, and housed in a cylinder with 3.6 m diameter. The edges of the triangles are covered by aluminium coils. The magnetic current is pulsed with the same time structure as the neutrino beam in it. A field of 0.12 T is obtained, parallel to the external edge and independent of the distance from the center. The material of the front and back faces corresponds to less than 4% of a radiation length. The six spokes of the magnet represent a dead space for momentum reconstruction, which concerns about the 15% of the tracks reaching the magnet.

The momentum resolution $\Delta P/P$ of the magnet tracker results from the quadratic combination of two terms: a constant term, evaluated at 22% from multiple scattering, and a term proportional to the momentum, which reflects the measurement accuracy. The measured resolution, shown in Figure 3.6, is given by

$$\frac{\Delta P}{P} = 22\% + 3.5\% \frac{P}{\text{GeV}/c}.$$ (3.1)
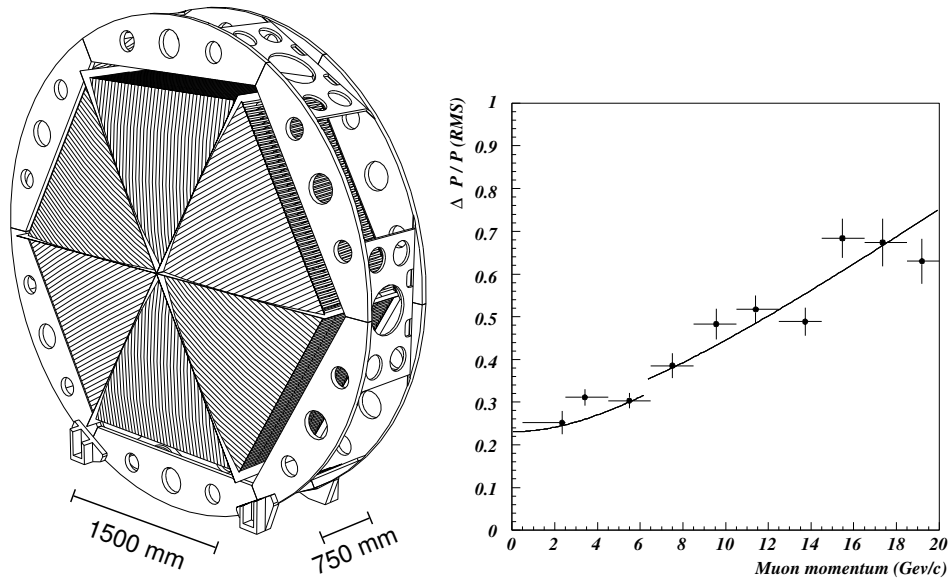
Figure 3.6: **Left:** The Hexagonal Magnet. **Right:** resolution on the momentum measured by the magnet trackers for particles traversing the hexagonal magnet. The momentum measurement uses only diamond tracker information and the resolution was determined by comparing, in neutrino events, the momenta measured for muons which are also reconstructed in the muon spectrometer.

3.5 The Calorimeter

The calorimeter [46] measures the energy and the direction of the hadron showers, and tracks muons before they arrive at the muon spectrometer. The calorimeter consist of 3 sectors of decreasing granularity called, electro-magnetic sector (EM), the first hadronic sector (HAD1) and the second hadronic sector (HAD2). The total depth corresponds to 144 radiation lengths, thus 99% of a shower from a 5 GeV pion is contained. The planes are transversally segmented to modules that are oriented alternatingly horizontally or vertically, Figure 3.7.

39
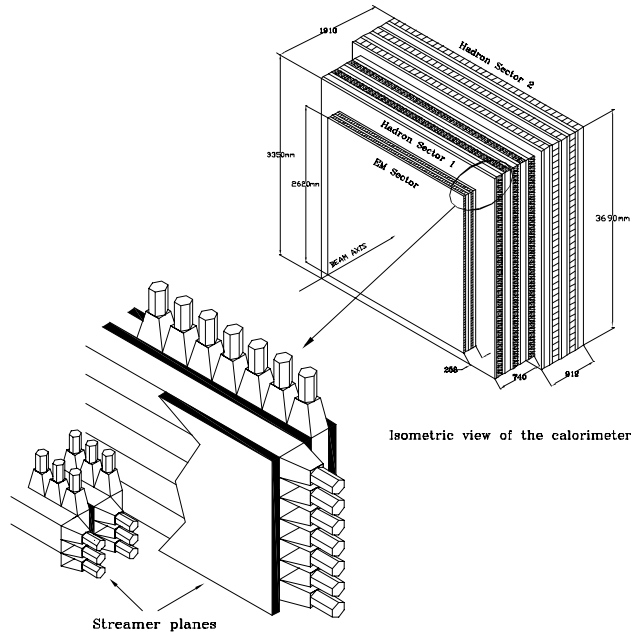
Figure 3.7: Layout of the calorimeter.

The EM and HAD1 sections are made by "spaghetti technique" [44]: thin scintillating fibers (1 mm diameter) are embedded into a lead matrix, with a volume ratio 1:4. Such a ratio leads to a compensated detector, with the same detection efficiency for energy associated with the electromagnetic and the hadronic part of the event products.

The last section, HAD2, is lead/scintillating strip sandwich calorimeter with a volume 4:1. Each plane of the EM sector contains 31 modules. Each modules consists of 21 layers of grooved lead, 1.9 mm thick, interspersed with plastic scintillating fibers of 1 mm diameter. The length of a module is 2.62 m and the thickness is 82.4 mm. The total thickness of the EM sector corresponds to about

20 radiation length. It is sufficient to contain the longitudinal extension of a electromagnetic showers. There are 740 fibers in each modules. On both sides of a module, the fibers are assembled into two bundles and each bundle is coupled to a PMT via a Plexiglas light guide. Each plane of the HAD1 sector contains 40 modules. Each modules consist of 43 layer of lead, with a length of 3.35 m. There are 1554 scintillating plastic fibers in each module. At both ends the fibers are collected into one bundle and coupled to PMT via a light guide. Each plane of the HAD2 sector contains 18 modules. Each modules is built as a sandwich of five layers of lead with a thickness of 1.6 cm and five layers of 4 mm thick scintillator strips. The modules are 3.69 m long and 20 cm wide. Each module is coupled to four PMT's via light guides,two on either side.

The intrinsic performance of the calorimeter was determined with various test beams of the electrons and pions of well defined energy, ranging from 2.5 to 10 GeV for electrons and from 3 to 20 GeV for pions [47]. The energy resolution for electrons is:

$$\frac{\sigma(E)}{E} = \frac{(13.8 \pm 0.9)\%}{\sqrt{E(GeV)}} + (-0.2 \pm 0.4)\% \tag{3.2}$$

while for pions

$$\frac{\sigma(E)}{E} = \frac{(33.3 \pm 2.4)\%}{\sqrt{E(GeV)}} + (1.4 \pm 0.7)\%. \tag{3.3}$$

3.6   The Muon Spectrometer

The role of the muon spectrometer in the CHORUS detector is to identify the muons and to determine their charge and momentum. The spectrometer is located behind the calorimeter, so only the muons with energy greater than about 1.5 GeV can reach it. The main source of background for antineutrino induced charm production search is the ν_μ induced charm production with primary μ^- reconstructed as μ^+ in the spectrometer. Thus, the CHORUS spectrometer performances affected the antineutrino analysis in a very crucial way.

As illustrated in Figure 3.8, the spectrometer consists of six magnetized iron toroidal magnets with scintillating strips, drift chambers and streamer tubes. In addition, scintillating planes interleaved with the magnet iron provide a measurement of the leakage of hadronic showers from the back of the calorimeter into the muon spectrometer at the entrance of the spectrometer. The fast signal from the scintillator planes are also used for triggering.

The momentum of a muon is determined from the bending of its trajectory in the six toroidal magnets. If a low momentum muon stops in the spectrometer, its momentum is also estimated from the range measurement. Each magnet consists of twenty 2.5 cm thick iron disks with an outer diameter of 375 cm, interleaved with 0.5 cm thick scintillator planes inserted into the 0.6 cm gaps between the disks. The iron is magnetized by four sets of water-cooled copper
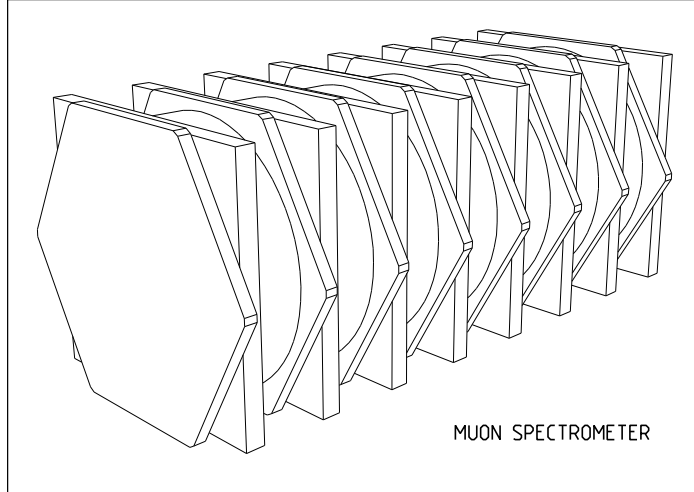
Figure 3.8: The components of the muon spectrometer.

coils passing through a 8.5 *cm* wide hole in the center of each magnet. A toroid field with an average strength of 1.7 *T* is obtained by applying a continuous current of 700 *A* through the coils. The field in the iron is nearly independent of the azimuthal angle but varies by about 25% along the radius. The polarity is such that negatively charged muons are bent towards the center of the magnets and positively charged muons are bent outwards. During antineutrino running, the polarity is inverted. The six magnets are positioned at increasing height to follow the 42 *mrad* slope of the beam-line. In each magnet, 20 planes of scintillating plastic strips are embedded between the iron disks. They are grouped in four planes of five consecutive layers, two planes with vertical and two planes with horizontal orientation. These are used for triggering purposes, for the detection of energy leakage from the calorimeter and for a range measurement of muons

with up to 5 GeV/c at the entrance of the spectrometer. The energy measurement of the shower tails is primarily of interest for studies of neutrino nucleon structure functions where the calorimeter is used as massive target.

Seven drift chambers have been installed to reconstruct the muon trajectories through the six magnets. Each chamber consists of three hexagonal planes with wires oriented at 60° with respect to each other. The chambers are flushed with a gas mixture of 60% argon and 40% ethane. Each plane has 62 parallel sense wires with a diameter of 40 μm and a length of 375 cm. A nearly uniform electric field is obtained using the field shaping wires at different voltages. The signals from the sense wires are amplified with pre-amplifiers and readout by time-to-digital converters (TDC). Each TDC has a buffer of four hits per event. The hit resolution obtained from a drift time measurement is about 1 mm and the efficiency per plane is better than 99%.

The absolute calibration was performed using negative 75 GeV/c test beam muons, corresponding to 71 GeV/c at the entrance of the spectrometer due to ionization losses in the upstream detectors and beam elements. The momentum resolution of the muon spectrometer is about 19% at 70 GeV, as calculated from data obtained with a test beam of negative muons. The momentum resolution of the muon spectrometer has been evaluated using a detailed simulation, the results of which are shown in Figure 3.9. These also provide a validation of the resolution determined from simulation, indicated by the open dot. For stopping muons, the
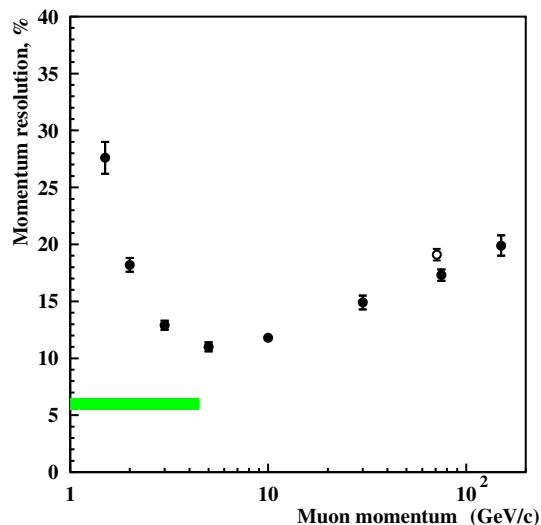
Figure 3.9: The muon spectrometer resolution as a function of the incident momentum. The full dots show Monte Carlo events, and the open dots at show real events 71 GeV/c test beam muons. The shaded band corresponds to muons stopping in the spectrometer, with their momentum measured by range.

charge is determined from the curvature of the trajectory, whereas the momentum is determined from their range, resulting in a momentum resolution of 6%. The efficiencies of the trigger signals provided by the spectrometer scintillators are close to 100%. The spectrometer energy resolution for shower tails above 1 GeV is $(110 \div 150)\%/\sqrt{E(\text{GeV})}$. Relative alignment of the spectrometer components is performed with 100 GeV/c test beam muons recorded with the magnetic field off. Alignment relative to the rest of the CHORUS detector is done by reconstructing high-momentum muons in the neutrino beam traversing the entire detector.

45

3.7   Trigger System

The trigger system has been designed to select neutrino induced interactions in the emulsion target and to reject background from cosmic rays, beam muons and neutrino interactions outside the target.

The scintillator trigger-hodoscopes are labeled as E (emulsion), T (timing), H (hodoscope), V (veto) and A (anti-counter), as shown in Figure 3.10. The E and T planes are installed between the emulsion target and the hadron spectrometer, whereas H is located downstream from the hadron spectrometer.   The A and
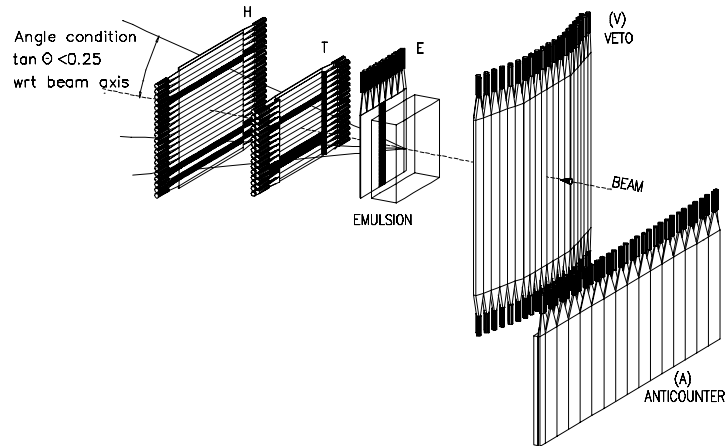
Figure 3.10: Layout of the trigger.

V planes are installed upstream of the emulsion target.   The main trigger is for neutrino interactions in emulsion, defined by a coincidence of hits in the

hodoscopes E, T and H consistent with a particle trajectory with $\tan\theta < 0.25$ with respect to the neutrino beam axis. A veto is defined by any combination of a counter hit in the veto hodoscopes (V and A), and a hit in T, with precise timing to avoid vetoes due to backscattering of particles coming from neutrino interactions in the target. The measured rate of neutrino interactions in 0.5 events per 10^{13} protons on the SPS target corresponding to an effective neutrino target mass of 1600 kg.

3.9   The Emulsion Scanning Technique

Scanning of the emulsion plates is performed by a fully automated scanning system, the track selector [49, 50], was developed by Nagoya group during the course of the experiment. It has been realized by the fusion of a computer controlled mechanism, a microscope optic with CCD camera readout, electronics for the video signal processing and for the digital signal processing. Track recognition for penetrating tracks in an emulsion film is done by superimposing several tomographic images taken at different depths.

The entire emulsion plate (36 x 71 cm^2 for the interface sheets, and 36 $\times$ 35.5 cm^2 for the target sheets) is placed on the microscope stage and kept flat by vacuum. Immersion oil is put on the surface of the emulsion plate to optimize the light illumination of the microscope objective lenses. The view size of the objective lens is $150 \times 120~\mu m^2$ and the focus depth is $\sim 5~\mu m$.

Inter calibration between the microscope and the emulsion plate coordinates is achieved by means of fiducial marks. The emulsion provides three-dimensional images of the trajectories with a grain ("hit") size of 1 μm and an average density of 300-400 hits per millimeter for minimum ionizing particles (Figure 3.11). The images are collected by a Hammatsu CCD camera. An emulsion layer with a thickness of ~ 100 μm is used to recognize the penetrating track. When the focal plane is moved in the emulsion layer, 16 tomographic CCD images of different depths are read out. By checking the coincidence of these images, the penetrating tracks can then be recognized. Figure 3.12 displays the track reconstruction procedure in the automatic scanning system. The position and slope information of all the recognized tracks are then stored in a data base. This procedure is repeated view by view, with a 30 μm overlap, to cover the entire required surface.

The three-dimensional information of the emulsion is converted into many layers of a tomographical image by the synchronized interplay between the microscope and the CCD camera. Each tomographical image is focused on some depth and cover an area of 150×120 μm^2.

The Track Selector is a type of video image processor and has 16 frame memories. It digitizes the CCD video signals and sends the data into a dynamic frame memory. Sixteen layers of digitized images are stored, and the predicted tracks are located by superimposing the data with different shifts between layers. A
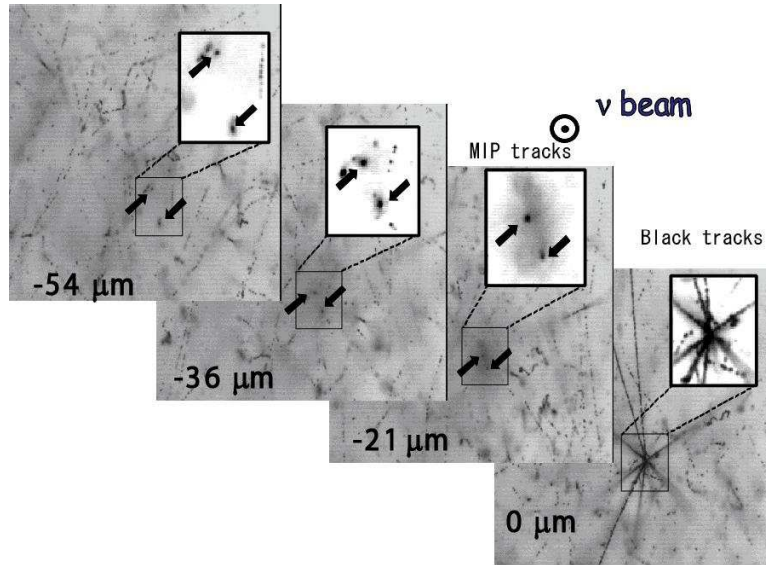
Figure 3.11: Microscope view of a vertex found in the emulsions. The depth of images goes down with the beam direction. The two tracks of charged particles marked with arrows get closer as they approach the neutrino interaction point. The black tracks that are seen at 0 μm depth are highly ionizing nuclear fragments and slow hadrons.
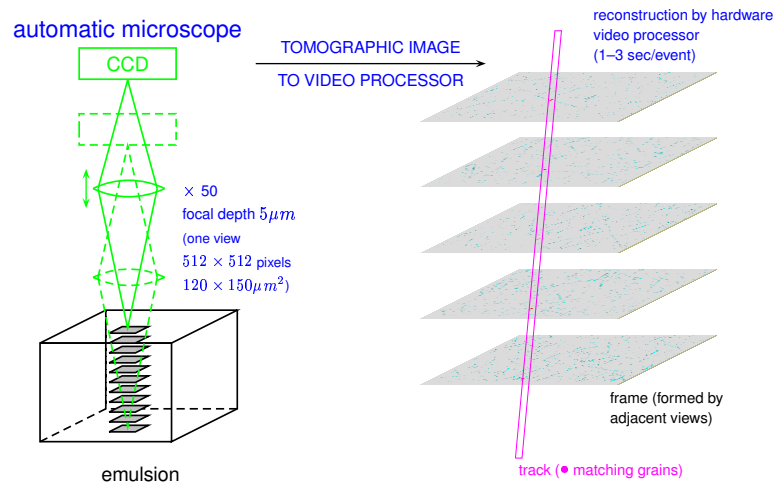
Figure 3.12: Schematic description of the track reconstruction procedure in the automatic scanning system.

track is identified by having an enhancement in the superimposed signals when the shifts match the angle of the track. Found tracks are then followed to the next emulsion plate, until the neutrino vertices are located. Figure 3.12 displays the track reconstruction procedure in the automatic scanning system.

3.10   CHORUS Data Sample

The CHORUS detector was exposed to the wide-band neutrino beam of the CERN SPS during the years 1994–97, with an integrated flux of 5.06×10^{19} protons on target. The data acquisition system recording the response of the electronic detectors was operational for 90% of the time. The average dead time for the emulsion interaction triggers was 12%. The trigger efficiency was 99% for charged current (CC) and 90% for neutral-current (NC) events [48].

3.10.1   Neutrino Oscillation Analysis in CHORUS

The CHORUS collaboration already reported, limits on $\nu_\mu \rightarrow \nu_\tau$ oscillation obtained from an analysis of a subsample of neutrino interaction [51]. In the second phase of analysis, the search for ν_τ interactions has been performed for the following three decay modes of the τ lepton:

(1) $\tau^- \rightarrow \mu^- \nu_\tau \bar{\nu}_\mu$

(2) $\tau^- \rightarrow h^- (n\pi^0)\nu_\tau$

(3) $\tau^- \rightarrow h^- h^+ h^- (n\pi^0)\nu_\tau$

E= 40.3 GeV

E= 36.9 GeV

Pmu= -16.0 GeV/c super-samt

E= 11.3 GeV

Pmu= 3.6 GeV/c samtra
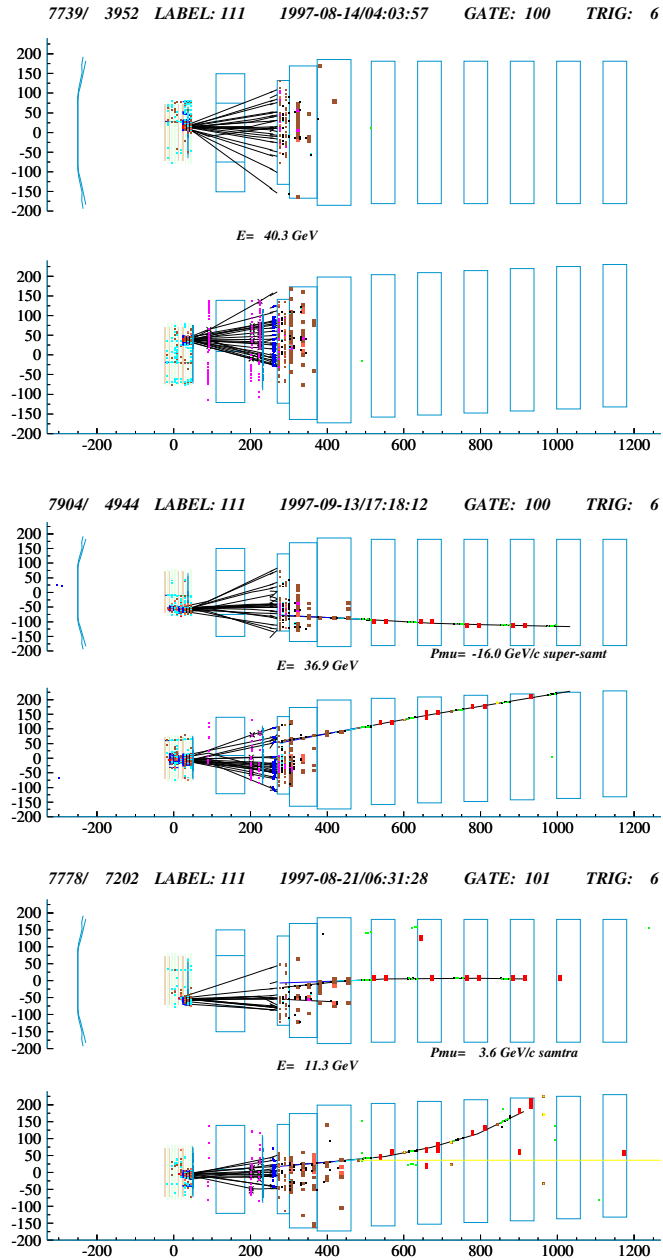
Figure 3.13: Example of **Top:** 0μ, **Middle:** μ^- and **Bottom:** μ^+ events in the CHORUS detector.

51

The information of the electronic detectors has been used to define two data sets, 1μ and 0μ samples, Figure 3.13, distinguished by the presence or absence of one reconstructed muon of negative charge. For each sample few kinematical selections are applied to reduce the scanning load, while keeping a high sensitivity to the two decay modes of the τ. The resulting $1\mu(0\mu)$ sample consists of 477,600(335,398) events with a reconstructed vertex in emulsion. Among this sample $\sim$150,000 1μ and $\sim$37,000 0μ events were located in nuclear emulsions and analyzed. No τ decay is found, neither in the 1μ sample nor in the 0μ sample once the best set of selections is applied. The null observation is used to set limits on oscillation parameters. The limit on the $\nu_\mu \to \nu_\tau$ oscillation probability obtained $P_{\mu\tau} \leq 1.72 \times 10^{-4}$ at 90% C.L.. In a two-family oscillation formalism, the result can be expressed as an exclusion plot in the parameter space $(\sin^2 \theta_{\mu\tau}, \Delta m^2)$ as shown in Figure 3.14. The sensitivity of the experiment has been obtained as $S_{\mu\tau} = 2.5 \times 10^{-4}$. In the absence of signal events, the probability to obtain an upper limit of 1.72×10^{-4} or lower is 28% [52].

3.10.2   Multiplicity Measurement in CHORUS

In the CHORUS experiment, quasi-elastic charge-current (QE) interactions were for the first time topologically identified with nuclear emulsions [5]. An event is defined as QE if there is no shower track other than muon and sum of
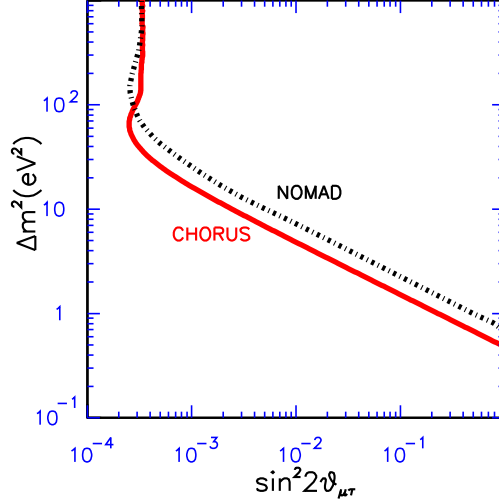
Figure 3.14: Final limit of CHORUS on $\nu_\mu \rightarrow \nu_\tau$ oscillation compared to the NOMAD result.

the grey and black tracks[1] is zero or one at the neutrino vertex. The fraction of quasi-elastic events was measured to be $(2.0 \pm 0.5)\%$ for ν_μ and $(5.3 \pm 0.9)\%$ for $\bar\nu_\mu$ interactions. The ratio of QE-like events to events with one shower (muon) and any number of grey and black tracks was measured to be $(23.2 \pm 4.9)\%$ for ν_μ and $(35.5 \pm 4.8)\%$ for $\bar\nu_\mu$ interactions.

To understand the nuclear mechanism involving hadrons in the nucleus, the sub-sample of QE-like (without any visible recoil) ν_μ events with neither black nor grey prongs was studied. The fraction of this type of topology was measured

---

[1] Shower particles correspond to relativistic singly charged particle (MIP) with a velocity $\beta \geq 0.7$ and grain density g_0. Grey track particles correspond to charged particles with velocity $0.25 \leq \beta < 0.7$ and a grain density $1.4g_0 < g < 5g_0$. The heavy particles are produced by nuclear fragments and comparatively slower particles emitted from the target with a velocity $\beta < 0.25$ and the grain density is $g > 5g_0$.

as $(1.2 \pm 0.4)\%$ for ν_μ and $(5.3 \pm 0.9)\%$ for $\bar{\nu}_\mu$ interactions. The average values of kinematical parameters, $\langle E_\nu \rangle$, $\langle E_{\bar{\nu}} \rangle$, $\langle W^2 \rangle$, $\langle Q^2 \rangle$ for QE-like ν_μ and $\bar{\nu}_\mu$ interactions were as given in Table 3.3.

Table 3.3: Kinematical variables for QE-like events in ν_μ and $\bar{\nu}_\mu$ interactions.

	$\langle E_\nu \rangle$(GeV)	$< W^2 >$ (GeV$^2/c^4$)	Q^2((GeV/c)^2)
ν_μ (n_h=0)	35.8±9.2	21.0±14.3	0.8±0.2
ν_μ (n_h=1)	19.0±2.6	5.1±0.7	0.8±0.2
$\bar{\nu}_\mu$ (n_h=0)	28.9±3.7	8.8±4.2	1.1±0.2

3.10.3   Charm Physics in CHORUS

A sample of 2013 charmed interactions has been collected in the emulsion target of the CHORUS detector. This charm sample corresponds to the 95,450 charged current located interactions with a negative muon in the final state. In the CHORUS experiment, the charm hadronizes in four charmed hadron species, one is the neutral D^0 meson and the others are the D^+ and D_s mesons and the Λ_c baryon. These particles, whose main properties are summarized in Table 3.4, then decay to non-charmed states via electroweak interactions, with decay paths of the order of 1 mm at CHORUS energy. Theirs decays can then be identified in the emulsions, although the topology of the event only allows to distinguish neutral from charged charmed particles.

Table 3.4: Main properties of charmed hadrons [6].

Hadron	Quark contents	Mass [MeV]	Lifetime $[10^{-15}\text{s}]$
D^0	$c\bar{u}$	1864.6 ± 0.5	410.3 ± 1.5
D^+	cd	1869.4 ± 0.5	1040 ± 7
D_s^+	$c\bar{s}$	1968.3 ± 0.5	490 ± 9
Λ_c^+	udc	2284.9 ± 0.6	200 ± 6

3.10.3.1 D^0 Analysis

A first measurement of the production rate of D^0 mesons reported by the collaboration [53]. It was obtained from a subsample of neutrino interactions analyzed with NetScan method. The results have been updated with the full statistics [54].

In the sample of 93,807 ν_μCC events, 2752 events were selected for visual inspection. 819 D^0 candidates were found with a two prong decay topology, 226 with a four prong one, and 3 candidates with a six prong topology. The numbers of estimated background coming from Λ^0 and K_s^0 are 11.5 ± 1.9 and 25.1 ± 2.9 respectively.

After the background subtraction and efficiency correction, two prong decay branching ratio was found to be $BR(D^0 \to V2) = 0.647 \pm 0.049 \pm 0.031$. The first measurement of six prong branching ratio were obtained as $BR(D^0 \to V6) = (1.2^{+1.3}_{-0.9} \pm 0.2) \times 10^{-3}$.

The fully neutral D^0 topological branching ratio has also been measured. It was previously assumed to be about 5% [55]. The fully neutral branching ratio

can be written as:

$$BR(D^0 \to V0) = 1 - BR(D^0 \to V4)(1 + \frac{BR(D^0 \to V2)}{BR(D^0 \to V4)} + \frac{BR(D^0 \to V6)}{BR(D^0 \to V4)}).$$

where the $BR(D^0 \to V4) = 0.1339 \pm 0.0061$ was precisely measured by other experiments for the all V4 decay modes [55]. Therefore, the fully neutral branching ratio was found to be

$$BR(D^0 \to V0) = 0.218 \pm 0.049 \pm 0.036$$

and D^0 production rate was measured to be

$$\frac{\sigma(D^0)}{\sigma(CC)} = (2.69 \pm 0.18 \pm 0.13)\%.$$

3.10.3.2 D* Production

The identification of the D^{*+} in CHORUS is based on the $D^{*+} \to D^0\pi^+$ decay detection [56]. This decay is characterized by low transverse momentum ($p_\perp \leq$ 39 MeV/c) and, therefore, the π^+ has a low momentum (≤ 4 GeV/c) and small angle with respect to the D^0. In emulsions this event is seen as a D^0 decay with a positive hadron at the primary vertex emitted with a small $p_\perp$ with respect to the D^0.

The momentum of the hadrons is measured by the hadron spectrometer downstream of the target. 488 visually inspected D^0's with a flight length larger than 100 mm are used as a starting sample. 377 hadron tracks at the primary vertex have the momentum measured. The hadron is required to be positive and its

56

angle with respect to the D^0 to be less than 60 $mrad$. Negative hadrons are used for the background estimation. After background subtraction, the $p_\perp$ distribution for positive hadrons shows an excess of 22.1 ± 5.5 events in the range 10 to 50 MeV/c which can be attributed to D^{*+} decays. The ratio of cross-sections $\sigma(D^*)/\sigma(D^0) = 0.38 \pm 0.09 \pm 0.05$ is measured. Given the D^0 cross-section measurement [54], the D^* production rate relative to CC events is

$$\frac{\sigma(D^*)}{\sigma(CC)} = (1.02 \pm 0.25 \pm 0.15)\%.$$

3.10.3.3 Λ_c^+ Production

This analysis is based on a statistical approach using the flight length distributions of charmed hadrons [57]. Two different sets of criteria on selection have applied. The aim is to select one sample enriched in Λ_c^+ decays, called selection A, and another where the D^+ and D_s^+ decays should dominate, called selection B. In order to have a negligible background contamination, in the selection B only three-prong decays are considered while in the selection A one also one-prong decays are included. The criteria specified by selection A were applied to a sample of 50,414 μ events (5157 of which had a muon with momentum greater that 30 GeV/c) and 1614 events were selected for visual inspection. 62 events are confirmed as 1-prong decay and 66 events show 3-prong decay topology. The criteria specified by selection B were applied to 56,761 ν_μ CC interactions (5061 of which have $p_\mu > 30$ GeV) and identified 586 events as possible decay candidates.

133 events are 1-prong decay and 77 events are 3-prong decay topology.

Combining the short and long decay search and taking into account the detection efficiency and background estimation, the number of Λ_c candidates was found to be $861 \pm 198(\text{stat}) \pm 98(\text{syst})^{-54}_{+140}(QE)$.

At an average neutrino energy of 27 GeV, the Λ_c production cross section in ν_μ charged current interaction was measured to be

$$\frac{\sigma(\Lambda_c)}{\sigma(CC)} = (1.54 \pm 0.35(\text{stat}) \pm 0.18(\text{syst}))\%.$$

and branching ratio into 3-prongs was determined

$$BR(\Lambda_c^+ \rightarrow 3 - prong) = 0.24 \pm 0.07(\text{stat}) \pm 0.04(\text{syst}).$$

3.10.3.4 Quasi-elastic Charmed Baryon Production

A study of quasi-elastic production of charmed baryons in charged current interactions of neutrinos was performed by looking for their characteristic topologies [58]. Quasi-elastic charmed baryon production is characterized by two or three tracks at the primary vertex including the muon and a low hadronic and electromagnetic activity. In this analysis, a total of 46,105 ν_μ events was used and 769 events were selected for visual inspection. After visual inspection and all kinematical cuts (less than 200 μm flight length cut to enrich the sample of Λ_c) 13 candidates with an estimated background of 1.7 events were found. The cross-sections for quasi-elastic production of charmed baryons was measured to

be

$$\frac{\sigma(QE)}{\sigma(CC)} = (0.23^{+0.12}_{-0.06}(\text{stat})^{+0.02}_{-0.03}(\text{syst}))\%.$$

It shows that at an average neutrino energy of 27 GeV, the quasi-elastic contribution is about 15% of the all Λ_c production.

3.10.3.5 Fragmentation Properties of Charmed Particle Production

The measurement of the fragmentation properties of charmed particle production gives insight in the hadronization process and allows a better description of charm production to be formulated. Fragmentation properties of deep-inelastic charm production were measured by using 1048 D^0 charm candidates. Out of these D^0 events, 819 show a two-prong decay topology, 226 a four-prong topology, and only three have six charged daughter tracks at the decay vertex [54].

In order to study the fragmentation of charmed quarks into hadrons, z which is the ratio of the energy of the charmed particle E^D and the energy transfer to the hadronic system ν was defined as $z = E^D/\nu$. The estimation of ν was obtained from the measurement of the total energy deposited in the calorimeter, after subtraction of the energy loss of the muon and correction for the energy deposited in the emulsion stacks.

The mean value of z was measured to be $\langle z \rangle = 0.63 \pm 0.03(\text{stat}) \pm 0.01(\text{syst})$ [59]. From fits to the z distribution, values for the Peterson parameter $\epsilon_P = 0.108 \pm 0.017(\text{stat}) \pm 0.013(\text{syst})$ and the Collins-Spiller parameter $\epsilon_{CS} = 0.21^{+0.05}_{-0.04}(\text{stat}) \pm$

0.04(syst) were found.

3.10.3.6 Associated Charm Production

Associated charm ($c\bar{c}$) production in neutrino interactions is a very rare process and therefore very difficult to observe. A search for associated charm production in ν_μCC interactions was performed and one event with a double charm decay topology with an estimated background of 0.04 was found [60]. A new search for associated charm production in both charged current and neutral-current interaction with a high statistics have been performed [61]. 26,621 NC and 99,245 CC located ν_μ interactions have been analyzed. Three double charm decays have been observed in NC sample with an estimated background of 0.025 ± 0.003. One double charm decay has been observed in CC ν_μ with an estimated background of 0.18 ± 0.03.

After the background subtraction and efficiency correction, the average rate of double charm production at the average neutrino energy of 27 GeV was estimated to be

$$\frac{\sigma(c\bar{c}\nu_\mu)}{\sigma(NC)} = (3.96^{+3.06}_{-2.51}(\text{stat}) \pm 0.59(\text{syst}))) \times 10^{-3},$$

If we assume the charged current double charm event is coming from background process, the limit is obtained to be

$$\frac{\sigma(c\bar{c}\mu^-)}{\sigma(CC)} < 9.69 \times 10^{-4}$$

at 90% C.L..

CHAPTER 4

EVENT RECONSTRUCTION AND SELECTION IN

EMULSION

Reconstruction and analysis of the neutrino interactions in emulsion consist of several steps:

1. In the first one, the long track reconstructed by electronic detectors is used to predict the event location in the emulsion target.

2. The second step is the event location in emulsion: reconstructed tracks are scanned back through the emulsion target region until the vertex is located. Such a track is called "*scan back*" track.

3. In the third step, a fiducial volume surrounding the interaction vertex is analyzed by automatic microscopes and a three dimensional reconstruction of the neutrino interaction is produced; the events with a decay topology are selected.

4. The last step is a computer assisted eye-scanning by well trained operators.

The candidate events are carefully analyzed.

5. And then to estimate the efficiencies and background, Monte Carlo simulation of event reconstruction in emulsion, the so-called NetScan technique, is applied.

These steps are described in the following sections.

4.1 The Reconstruction of Neutrino Interaction Vertex by Electronic Detectors

All the events triggered and recorded in the electronic detectors are analyzed. To define the position of the primary neutrino interaction vertex and the parameters of the tracks, these events are processed by the CHORUS reconstruction program. In the first phase of the CHORUS analysis (Phase 1) a reconstruction program named CHORAL [62] was used to select the events for the emulsion analysis. In the second phase of the analysis (Phase 2), the CHORAL reconstruction program was replaced by the CHANT package [63].

The event reconstruction starts with the pattern recognition in the electronic detectors. Tracks are found in the fibre-trackers in the target region and, independently, in the muon spectrometer. A matching is attempted between these two sets of tracks in order to identify primary muons. Vertices are defined using the points of closest approach of the fibre-tracker tracks ("*TT-tracks*"). The primary vertex is the most upstream one that contains a muon. Such a muon is

defined as primary muon, and used as the so-called "*scan back*" track.

The selection of candidate tracks to be used for the event reconstruction was based on a χ^2 matching probability in the angular and position variables. For all the events with a primary vertex reconstructed inside the emulsion stacks, the track information is used to search for the interaction point in the emulsion target.

4.2 Event Location in Emulsion

The emulsion target, which is segmented into four stacks, has an overall mass of 770 kg, each of the stacks consisting of eight modules of 36 plates of size $36 \times 72\ cm^2$. Each plate has a 90 μm plastic support coated on both sides with a 350 μm emulsion layer. Downstream of each stack, there are three interface emulsion sheets with a 90 μm emulsion layer on both sides of an 800 μm thick plastic base and a set of scintillating fibre tracker planes. They are placed between the emulsion target and the next downstream fiber tracker module, as shown in Figure 4.1.

The interface sheets and the fibre trackers provide accurate predictions of particle trajectories into the emulsion stack for the location of the vertex positions. The accuracy of the fibre tracker prediction is about 150 μm in position and 2 $mrad$ in the track angle. The special sheet (SS) is packed with target emulsion stack on the downstream side, and is replaced by a new sheet after one year of
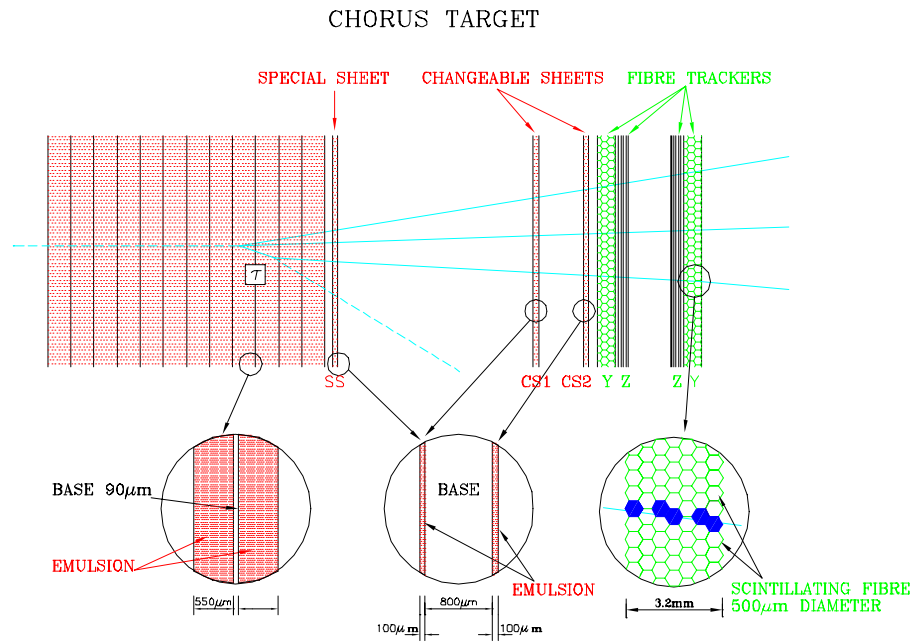
Figure 4.1: CHORUS Emulsion Target.

exposure. The two "*changeable sheets*" (CS1 and CS2) are mounted at the two faces of a 1 *cm* thick honeycomb panel, positioned in front of the first fiber tracker module downstream of the emulsion target.

In the 1994-95 data taking periods, the changeable sheets were replaced every three to six weeks during the running time of the experiment, to provide favourable background conditions for the recognition of the predicted tracks in the emulsion. During the 1996 data taking, two changeable sheets, and in the 1997 data taking one sheet change were found to be enough, due to the reduction of the background.

The target emulsion exposure was divided into a number of periods, called

as "*changeable sheet periods*". It is the interval of time during which one set of sheets were exposed. There are 8 periods during 1994 data taking (numbered as 1,2,3,4,5,6,7,8), 3 periods in 1995 (9,10,11), 3 periods in 1996 (21,22,23) and finally one period only in 1997 (31). The sheets were not changed during the 1997 run.

4.2.1 Changeable Sheet Scanning

The emulsion scanning of the event starts from the most downstream interface emulsion sheet, on the basis of the slope and position reconstructed using the information from the Target Tracker (TT). All selected tracks are extrapolated to and searched for in the first interface sheet (the so-called Changeable Sheet, CS) close to the electronic trackers. This procedure is called scan back location.

The fiber prediction coordinates of selected tracks are expressed in the general CHORUS reference frame while the measurements in emulsion are performed with respect to the X-ray marks. The position of these reference marks may be affected by the emulsion sheet expansion at the temperature and humidity of the scanning room. For this reason, the 4 X-ray mark coordinates (Y,Z) of each sheet are measured at the beginning of each scanning session.

Scanning starts by setting the emulsion plate on the microscope stage and measuring the X-ray marks on emulsion sheet in order to align CS and TT. This measurement allows for the calibration of the position of the emulsion plate

on the microscope stage. After the measurement of the X-ray marks, emulsion data acquisition starts. An automatic scanning is performed within $11 \times 11 = 121$ ($1080 \times 810 \ \mu m^2$) scanning views on up stream surface ($100 \ \mu m$ of thickness) in every plate around extrapolated position of scan back tracks.

When a track has been detected with the angle differences $\Delta\theta_Y$ and $\Delta\theta_Z$ (angle differences between predicted and measured angles) less than $40 \ mrad$, the track parameters are measured and stored in the Database. In order to select the good scan back tracks, the following selection criteria (which is called "*good stop*" method [1]) have been applied to all tracks found in the fiducial area:

- Pulse height (PH), $PH \equiv min(Nhit_{down} \times Nhit_{up}) \geq 13$,

- $\Delta\theta \equiv \sqrt{(\tan\theta_y^{cand} - \tan\theta_y^{pred})^2 + (\tan\theta_z^{cand} - \tan\theta_z^{pred})^2} \leq 0.006$.

In order to preserve the high efficiency in SS scanning, an additional selection was applied to good candidate tracks. For 1994, 1995 and 1996 runs the following criteria have been applied;

- $\Delta\theta \leq 0.015 \ rad$ without position cut, in order to reduce the background tracks,

- $PH \geq 10$ in order to reduce the noise which comes from the Compton electrons in the emulsion.

---

[1] In 94, 95, 96 CS and SS scanning and 97 CS scanning, good stop method has been applied; but not for 97 SS scanning.

Concerning 1997 data, due to the high track density in CS, different criteria have been applied;

- The tracks with $\chi^2/n.d.f. < 3.5$ [2] are selected. If there is no candidate track satisfying this criterion, the minimum χ^2 track is selected.

- Pulse height cut for 1997 data depends on the slope of the tracks and given by $PH = PH_{max}$ or $PH \geq PH_{min} - 10 * \theta^{cand}$.

All the candidates satisfying the above criteria were selected for SS scanning.

4.2.2 Special Sheet Scanning

After finding the tracks in CS, they are searched in SS. Tracks found in CS are extrapolated using TT angle and position information measured in CS. SS scanning is performed within $7 \times 7 = 49$ ($800 \times 700 \ \mu m^2$) scanning views for 1996 data ($9 \times 9 = 81$ scanning views for 1997 data) centered about predicted position. To pick up the good candidate, the good stop method was used for 1996 data. The following selection criteria are applied after the SS scanning:

---

[2] χ^2 for CS is defined as follows [64]:

- $\chi_i^2/n.d.f. = \{(\frac{\delta Y_i}{\sigma_{\delta Y}})^2 + (\frac{\delta Z_i}{\sigma_{\delta Z}})^2 + (\frac{\delta(\tan\theta_Y)_i}{\sigma_{\delta\tan\theta_Y}})^2 + (\frac{\delta\tan(\theta_Z)_i}{\sigma_{\delta\tan\theta_Z}})^2\}/4$
  where

  * $\sigma_{\delta Y} = 200. + 200. * abs(\tan\theta_Y)$
  * $\sigma_{\delta Z} = 200. + 200. * abs(\tan\theta_Z)$
  * $\sigma_{\delta\tan\theta_Y} = 0.004 + 0.004 * abs(\tan\theta_Y)$
  * $\sigma_{\delta\tan\theta_Z} = 0.004 + 0.004 * abs(\tan\theta_Z)$

- The tracks with $\chi^2/n.d.f. < 3.3$ [3] are selected. If there is no candidate track satisfying this criteria, minimum χ^2 is selected.

- $PH = PH_{max}$ or $PH \geq PH_{min} - 10 * \theta^{cand}$.

When a candidate track which satisfies the above conditions is found, track parameters are extrapolated to the bulk emulsion for bulk scanning.

4.2.3 Vertex Location

In order to locate vertices in bulk emulsion, tracks found in both interface emulsion sheets (CS and SS) are followed plate by plate (from down stream to) upstream. An automatic scanning is performed on the most upstream surface (100 μm of thickness layer) in every plate with the help of the angular and positional predictions. Bulk scanning is performed within $120 \times 90 \ \mu m^2$ (one scanning view) centered around predicted position. Vertex location in bulk starts

---

[3] χ^2 for SS is defined as follows [64]:

- $\chi_i^2/n.d.f. = \{(\frac{\delta Y_i}{\sigma_{\delta Y}})^2 + (\frac{\delta Z_i}{\sigma_{\delta Z}})^2 + (\frac{\delta(\tan\theta_Y)_i}{\sigma_{\delta\tan\theta_Y}})^2 + (\frac{\delta\tan(\theta_Z)_i}{\sigma_{\delta\tan\theta_Z}})^2\}/4$

- For the 1996 Data:
  * $\sigma_{\delta Y} = \sigma_{\delta Y} + 90.50 * abs(\tan\theta_Y)$
  * $\sigma_{\delta Z} = \sigma_{\delta Z} + 90.50 * abs(\tan\theta_Z)$
  * $\sigma_{\delta\tan\theta_Y} = \sigma_{\delta\tan\theta_Y} + 0.00114 * abs(\tan\theta_Y)$
  * $\sigma_{\delta\tan\theta_Z} = \sigma_{\delta\tan\theta_Z} + 0.00114 * abs(\tan\theta_Z)$

- For the 1997 Data:
  * $\sigma_{\delta Y} = \sigma_{\delta Y}(1 + 5 * abs(\tan\theta_Y))$
  * $\sigma_{\delta Z} = \sigma_{\delta Z}(1 + 5 * abs(\tan\theta_Z))$
  * $\sigma_{\delta\tan\theta_Y} = \sigma_{\delta\tan\theta_Y}(1 + 2.5 * abs(\tan\theta_Y))$
  * $\sigma_{\delta\tan\theta_Z} = \sigma_{\delta\tan\theta_Z}(1 + 2.5 * abs(\tan\theta_Z))$

with the measurement of the fiducial marks (light printed) on the emulsion sheets in order to get the coordinate on the emulsion plate. The relative position of each emulsion plate are aligned by measuring the four coordinates of the fiducial marks on the bulk emulsion.

Scanning in bulk starts from plate 1 which is closest to the SS. When the scan back track is found in that plate, then it is searched in the next plate, plate 2. For the following plates, positional prediction of the scan back track is made by extrapolating from the measured position on the previous plate. For the angular prediction of the scan back track, SS measured angle has been used, since the angular resolution measured in SS is better.

The scan back track is said to be found in the bulk plate if the following conditions are satisfied:

- $\Delta\theta_y \equiv |\tan\theta_y^{SS} - \tan\theta_y^{Pl.n}| \leq (0.025 + 0.05.\Delta\theta_{X7})\ rad$,

- $\Delta\theta_z \equiv |\tan\theta_z^{SS} - \tan\theta_z^{Pl.n}| \leq (0.025 + 0.05.\Delta\theta_{X7})\ rad$,

- $\Delta Y \equiv |Y^{Pl.n-1} - Y^{Pl.n}| \leq (15 + 50.\Delta\theta_{X7})\ \mu m$,

- $\Delta Z \equiv |Z^{Pl.n-1} - Z^{Pl.n}| \leq (15 + 50.\Delta\theta_{X7})\ \mu m$

where $(\theta_{X7y}, \theta_{X7z}) = (-0.080, 0)$ is the value of X7 beam slope and $\Delta\theta_{X7} = \sqrt{(\theta_y - \theta_{X7y})^2 + (\theta_z - \theta_{X7z})^2}$ and (θ_y, θ_z) is the track slope. Most of the scan back tracks have been picked up as a single candidate and 2% of them as multiple candidates including background tracks. The interaction vertex is assumed to be
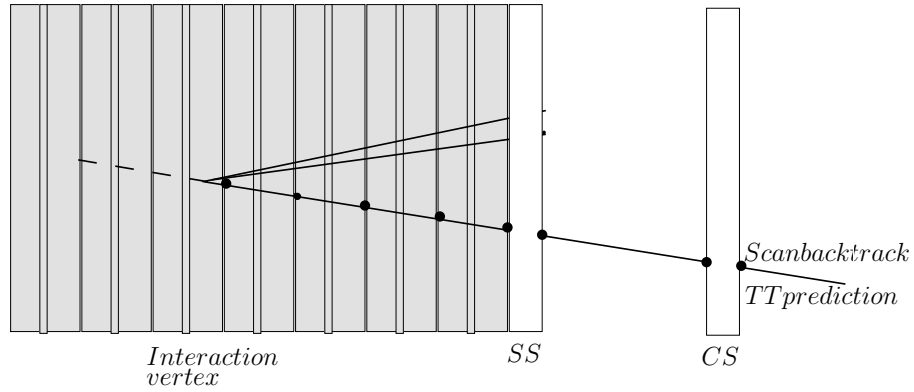
Figure 4.2: Vertex location.

located if the scan back track is not observed in two consecutive plates (consider
n and **n+1** plates), the first of which is defined as vertex plate as shown in
Figure 4.2.

4.3 Vertex Location of μ^+ Events

For our analysis, we performed a new event location in order to increase μ^+
sample size.

As mentioned in Sec. 4.1, event location starts with the reconstruction of
events inside the emulsion by the electronic detectors. 21103 events with at least
1 μ^+ have been reconstructed by the reconstruction program, CHANT. Since
emulsion scanning has been done in Nagoya University, only events in Nagoya
modules have been scanned and analyzed. This corresponds to 70% of 96 and
97 data. Emulsion modules which were scanned in Nagoya University are the
following:

$$
\text{1996 Data} \begin{cases} 11BT, 12BT, 15BT, 16BT, 18BT; \\[6pt] 21BT, 22BT, 25BT, 26BT; \\[6pt] 31BT, 32BT, 35BT, 36BT, 37BT, 38BT; \\[6pt] 41BT, 42BT, 45BT, 46BT, 47BT, 48BT. \end{cases}
$$

$$
\text{1997 Data} \begin{cases} 51BT, 52BT, 55BT, 56BT, 57BT, 58BT; \\[6pt] 61BT, 62BT, 65BT, 66BT, 67BT, 68BT; \\[6pt] 71BT, 72BT, 75BT, 76BT; \\[6pt] 81BT, 82BT, 85BT, 86BT, 88BT. \end{cases}
$$

Event location was performed according to the procedure explained in Sec. 4.2.

The automatic scanning results of event location can be summarized as:

- Total number of prediction for CS: 8881,

- Total number of events found in CS: 8764,

- Total number of events searched in SS: 8216,

- Total number of events found in SS: 7388,

- Total number of events found in bulk: 6531,

- Total number of events stopped in bulk: 4737,

- Total number of events manually confirmed: 3302.

From 21k events 8881 events have been searched in CS. The finding efficiency in CS is (found/searched) 98.9%. As we have seen from above, the number of events searched in SS is 8216, 548 events are out of the fiducial volume. The scan back finding efficiency in SS is found to be 83.1%. Figure 4.3 and Figure 4.4 show the angular difference of CS and SS angles which are measured and predicted at TT in y and z projections, respectively. The number of events connected to the bulk is 6531 (73.5%); 1793 events (20.2%) stopped in plate 1 to plate 3, 567 events (6.4%) do not have any tracks which stop in the bulk so called pass through. These events were not used in the analysis. 4737 events (53.2%) stop in emulsion between plate 4 and plate 35. These events have been checked one by one manually to confirm whether the vertex was located in the predicted plate is observed in the microscope or not, in total 3302 events (37.1%) have been manually confirmed. 416 events which were located in the previous location procedure was added. In total for the analysis, we have 3718 μ^+ events with at least a positive muon charge in the CHORUS muon spectrometer. By including events from previous location, the location efficiency becomes 41.8%.

In the Figure 4.5, the location efficiency is shown as a function of muon momentum and muon slope. The momentum dependence plot shows that at low momentum the efficiency decreases. At low momentum the muon track slopes are close to the reference X-beam. Location efficiency is parametrized in terms
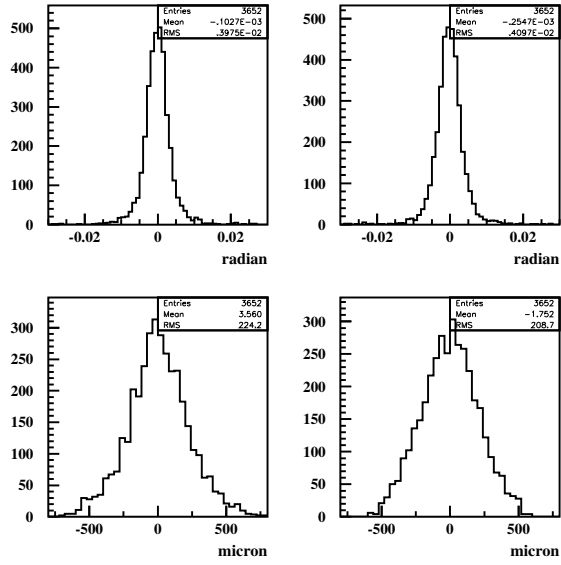
Figure 4.3: CS angular displacement.
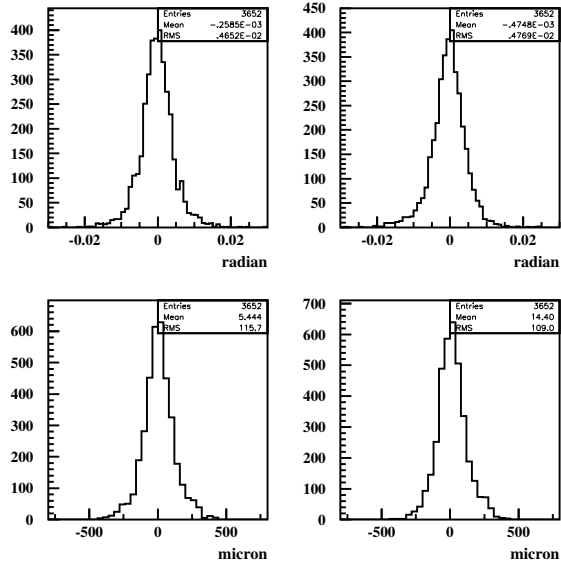
Figure 4.4: SS angular displacement.

of muon momentum and it is given by:

$$\epsilon_{location} = c_1(1 - c_2 \times \exp(-c_3 P_{\mu^+})). \tag{4.1}$$

The angle dependence plot shows that efficiency is low at large angle; this is reasonable. The event location has several sources of inefficiencies such as distortion of the emulsion, bad alignment, attachment of the scan back track to a background track.

Once the interaction vertex plate is identified, a detailed analysis of the emulsion volume around the vertex position is performed, recording for each event all track segments within a given angular acceptance. This type of scanning, originally developed for the DONUT experiment [65], is called "*NetScan*" data taking [66]. In the following section the NetScan data taking is explained in detail.

4.4 NetScan

Event reconstruction in the emulsions, the so-called NetScan technique, was developed in Nagoya University originally for the DONUT experiment [65] at Fermilab. The main feature of NetScan is that all track segments within a fixed volume centered on the vertex position are picked up. As mentioned, the events located with the scan back method are inherited by NetScan and used as a prediction of the vertex position. The NetScan data acquisition is performed by fully
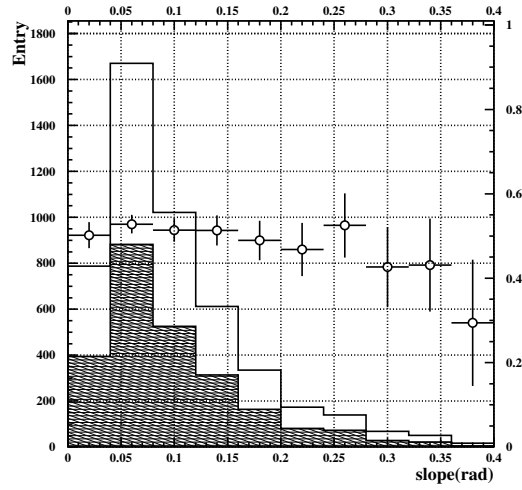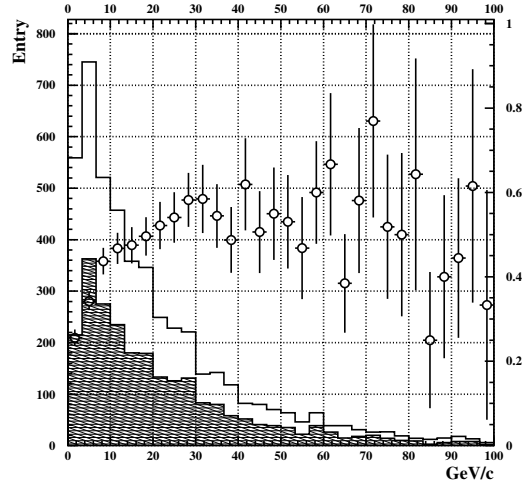
Figure 4.5: Location efficiencies of μ^+ events as a function of **Top:** momentum and **Bottom:** muon angle.

automatic scanning systems (UTS). The scanning area is much larger than scan back location.

In the CHORUS experiment, to perform the search for charm decays, the scan volume is taken as 1.5 mm wide in each transverse direction and 6.3 mm long, corresponding to eight plates (i.e., the vertex plate, and one upstream and six downstream plates [67]).

As for the scan back, sixteen tomographic images are taken in the most upstream 100 μm layer of each plate at different focal depths. The threshold on pulse height to retain a track segment is set to 10. All track segments, within the angular acceptance, in the fiducial volume are measured and stored. The angular acceptance is set to $-400 mrad < \theta_{y,z} < 400 mrad$, where θ_y and θ_z are the angles between the track and the beam axis (conventionally chosen as x) in the (x, y) and (x, z) planes. This is because of the decrease of efficiency of the UTS at larger angles.

4.4.1 Offline Reconstruction

The reconstruction program is written in C++ and is divided into two blocks: ECFSAL (Emulsion Chamber First Structure ALignment) [68] which performs first alignment and tracking, and ECVTXA (Emulsion Chamber VerTeX Analysis) [69] for background track rejection, fine alignment and vertex reconstruction.

4.4.1.1 Alignment and Tracking

Once the reliable track segments are selected on the basis of the pulse height cut off bigger than 12, "ghosts" must be rejected, i.e. copies of segments which are seen twice because they fall in the intersection zone of two microscope views. Then, if two segments having the same angle are found, the distances to the original track are compared. If the distance for one of them is greater than 5 μm, then it is rejected. After the segment selection, the recursive alignment-tracking program (ECFSAL) is run. It compares the pattern of segments in two neighbouring plates to determine the position and rotation parameters of the plate to plate alignment. As shown in Figure 4.6, the angle differences ($\Delta\theta$) between the segments and connected tracks (θ) and the position displacements (Δr) between extrapolated position are the parameters of the plate by plate alignment.

The tracking consists of the extrapolation of the segments of the first plate to the following one, looking for a matching segment in a cone of angle dependent on the alignment residuals (20 $mrad$ being the maximum angle), and in about 4 μm in position, corresponding to 3σ of alignment resolution. If no candidate is found, the starting segment is kept anyway, and the matching is tried in the further upstream plate. This means that gaps are allowed in the NetScan tracks which improves the track reconstruction efficiency.

Figure 4.7 shows the track reconstruction efficiency for $\tan\theta < 0.4$ for each
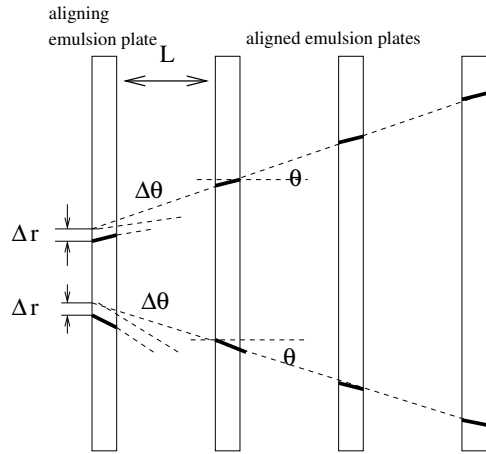
Figure 4.6: Parameter definitions used for the track connection and emulsion plate alignment.

plates. The average efficiency is about 98%. The inefficiency is due to emulsion problems and UTS's failure. Figure 4.8 shows the relation between tracking efficiency and track slope.

4.4.1.2 Fine Alignment

At the end of the first alignment-tracking process, on average 5,000 tracks are reconstructed in the fiducial volume but only a few of them are real event tracks. Almost 99% of this is background tracks, i.e. low momentum tracks coming from cosmic rays, radioactivity, low energy interactions of neutrals, accumulated during the years of emulsion exposure. Before the vertex reconstruction, it is mandatory

ID   10
Entries   21840
Mean   .9790
RMS   .1596E-01
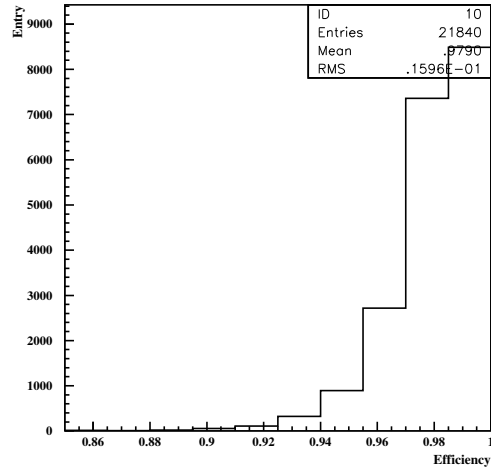
Figure 4.7: Track finding efficiency for each plate.
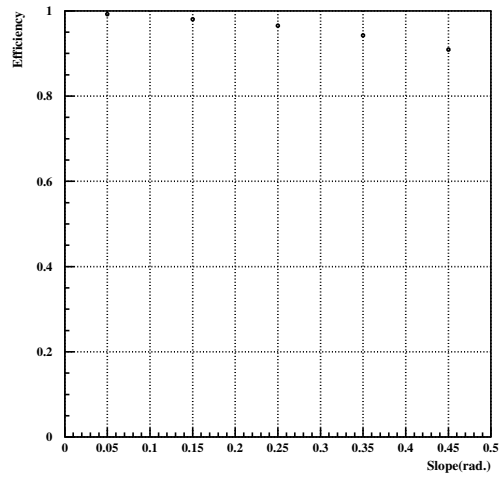
Figure 4.8: Track finding efficiency versus track slope.

79

to eliminate as much background as possible, since these fake tracks will generate fake vertices which will increase the manual check load. Fine alignment is performed after the event has been cleaned. This is done in ECVTXA.

Tracks are obtained by connecting several track segments, and the number of reconstructed tracks depends on the angular acceptance in the extrapolation of a segment to the following plate: the larger is the acceptance, the easier a segment will fall inside the solid angle. At the moment, in ECFSAL the tolerance is a floating value which depends on the plate alignment residuals: this means that low momentum tracks, that undergo large scattering, can appear with splittings in track segments. Of course, it would be easy to make them connected by increasing the acceptance; but this can be risky because then one could also attach event tracks to background tracks. It is therefore necessary to find a good balance between the level of misconnections introduced and the number of reconnected low momentum tracks. It was found that the optimal minimal momentum is 100 MeV.

After low momentum track rejection, a second, fine alignment is performed using information from the surviving tracks, similar in procedure to the first level one: position shift, angle shift, rotation between plates and gap corrections. Final tracks are chosen on the basis of their χ^2 value. These tracks, so called good tracks, are sent to vertex reconstruction.

Figure 4.9 shows RMS of the distribution of Δr after the fine alignment. After

the second alignment, the resolution is 0.5 μm in position.
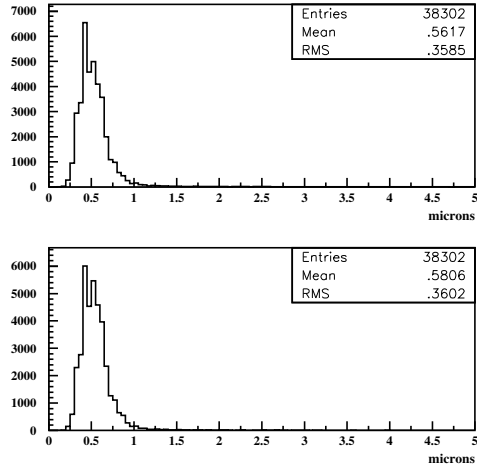
Figure 4.9: Position displacement RMS distribution for each plate. **Top:** y-axis, **Bottom:** z-axis.

4.4.2   Vertex Reconstruction

Before reconstructing the vertex, one must eliminate those tracks that seem to belong to the event only because they happen to pass through the fiducial volume, but do not originate therein. These are mainly particles produced in the neutrino interactions and their decay daughters. A track is defined to be a stopping track if it escapes the fiducial volume not more than once (no matter where, be it from the downstream face, or from the borders, or from the upstream face). All tracks which escape twice, are defined passing-through tracks and thus are not related to the event. After low momentum track rejection, on average 40 stopping tracks

81

are found in the fiducial volume. Most of the surviving tracks clearly are still background: in fact, they originate from fragments of low momentum tracks that ECVTXA was not able to reconnect and eliminate. Completely isolated segments are eliminated. Still included are the fragments of low momentum tracks made of two (or more) connected segments: since the minimum number of connected segments necessary to form a stand alone track is 2, such a fragment of a low momentum track is already considered a stopping track itself. One could increase the number of segments that form a track, but the price of this is a loss in the tracking efficiency. It was preferred to leave a bigger contamination but also higher efficiency, and use other methods to reject the background.

All the stopping tracks are used for the reconstruction of the vertices. First, tracks are considered two by two and two track vertices are constructed. The requirement for two tracks to form a vertex is that the distance between them is less than 20 μm. Also, single segments can be re-included, provided they are matched at less than 30 $mrad$ with a target tracker track; but at least one of the two tracks building the vertex must be connected in two plates. Two track vertices are then clustered to form a real vertex, requiring that the distance between two tracks that form the two track vertices is less than 10 μm.

4.5   Data Sample and Event Selection

In order to keep the high efficiency for the pentaquark search, the NetScan method is applied to 1μ events with an enlarged fiducial volume. The new scanning volume is like a truncated pyramid as shown in the Figure 4.10. This volume contains the vertex plate itself, the plate immediately upstream, and the ten plates downstream from the vertex plate, corresponding to 9.48 mm along the beam direction. The transverse area of the first plate is 1.5×1.5 mm^2, increasing to 3.0×3.0 mm^2 at the last plate. The volume is optimized to search for secondary vertices of charm or long flight decay pentaquark. Figure 4.11 shows the distribution of the number of plates corresponding to one NetScan data set.
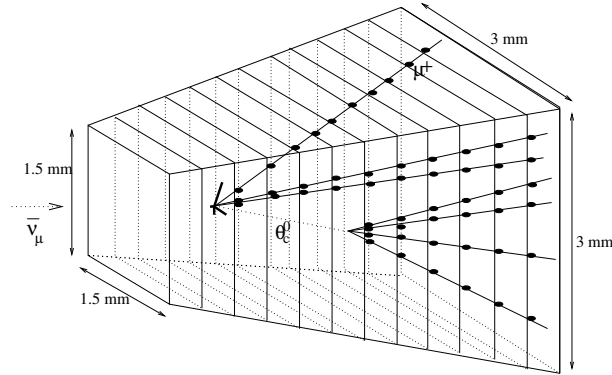
Figure 4.10: The NetScan volume with a sketch of a Θ_c^0 decay. The ellipses represent track segments in 100 μm emulsion layers in which automatic scanning performed. Offline programs reconstruct the tracks and associate them to common vertices.

The sample of 3718 μ^+ located events have been sent to NetScan for detailed analysis. Figure 4.12 shows two plates connected tracks for each module. The YZ
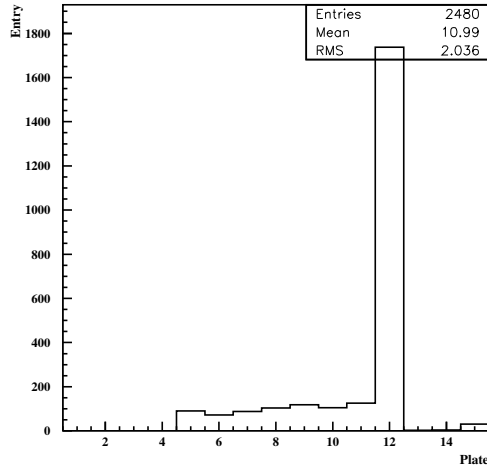
Figure 4.11: Number of plates consisting of one NetScan data set.

plane of detector is $1.4 \times 1.4\ m^2$, and the incident charged particle density is not uniform. For each module the distribution is different since some modules have a contribution from X-beam muons. We put a threshold on the two plate connected tracks to select good quality data sets. Table 4.1 shows the threshold for different modules. The small number of connected tracks is due to the misconnection of plates, and troubles in the optics or the emulsion plates.

Table 4.1: Threshold of number of two plates connected tracks.

Module	Threshold($/mm^2$)
1,2,5	20trks
6	30trks
7	40trks
8	50trks

84
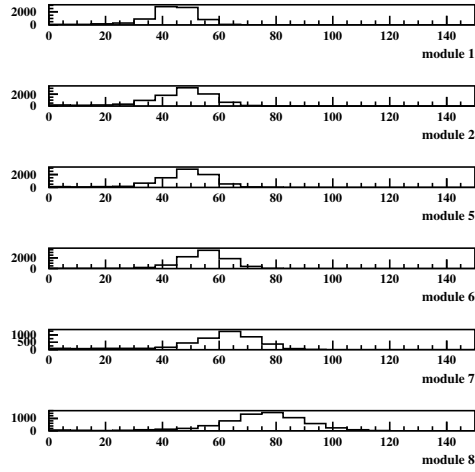
Figure 4.12: Two plates connected tracks for different module.

After the alignment and two plate connections the number of data sets which are available for the analysis are summarized in Table 4.2.

Table 4.2: The number of NetScan data sets passing the quality check.

Total number of data set	3718
Good Quality	3390
alignment is bad	160
two plates connected tracks are bad	11
both are bad	157

The number of good quality located events with a muon of positive charge determined by muon spectrometer is 3390. There is still a large fraction of background in this sample. To reduce the background, stronger criteria [70] on the muon identification have been applied:

- low momentum muons stopping inside the spectrometer are discarded;

- the distance of the impact point on the spectrometer entrance surface from its axis is required to be $\leq 150\ cm$;

- several muon reconstruction algorithms in the spectrometer are available, using only hits in the drift chambers or the combined data from all electronic detector. Consistency checks are applied when a muon track is reconstructed by more than one algorithm. Otherwise, the track length in the spectrometer has to be > 3 gaps (two magnets);

- when matching a spectrometer track with a track in the fiber trackers, a tighter cut is applied on the χ^2 of the global track fit.

With the above primary muon identification criteria, 2480 events (73.2%) were selected. These sample were used for decay search analysis[4].

4.6   Charm Selection

The sample 2480 μ^+ events still contains low momentum and passing through tracks. To select interesting decay topologies from this sample we do additional filtering of events using various cuts.

---

[4] "SatoMurat" Selection program [71] which was used for CHORUS neutrino charm decay and oscillation search, has been modified for decay search analysis.

An impact parameter based selection: The fundamental requirement of the selection is that two NetScan TT matched tracks go to two distinct reconstructed vertices. First, good tracks are selected based on the global angle difference of the fitted tracks and track segments. Then impact parameter between track and vertex point is calculated and an impact parameter cut is applied. Selection steps are the following in detail:

- Events must contain at least two TT matched tracks, which have to be two plate connected, going to two distinct vertices (one is primary vertex the other is the decay vertex). The condition for TT matching is

$$\Delta\theta_{TT} < 3.44\sqrt{(0.00546)^2 + (0.0194.\theta_t)^2} \ rad \qquad (4.2)$$

  at 99% C.L. as shown in the Figure 4.13 and Figure 4.14. This validates the primary vertex and assures that a second vertex (neutral charm or at least kink) is present. This requirement is necessary to have a reasonable manual check load.

- To eliminate low momentum tracks, the following cut (shown in Figure 4.16 and Figure 4.17) is applied at 99% C.L.

$$\Delta\theta_{global} < 2.31\sqrt{(0.00367)^2 + (0.0236.\theta_t)^2} rad \qquad (4.3)$$

  where the $\Delta\theta_{global}$ is the angle difference between the global angle of the track and the track segment angle measured in the last (and first) plate (see

87

Angle difference with TT ($\equiv$ 2 segments)

cut=3.44*sqrt(0.00546^2+(0.0194*theta)^2)
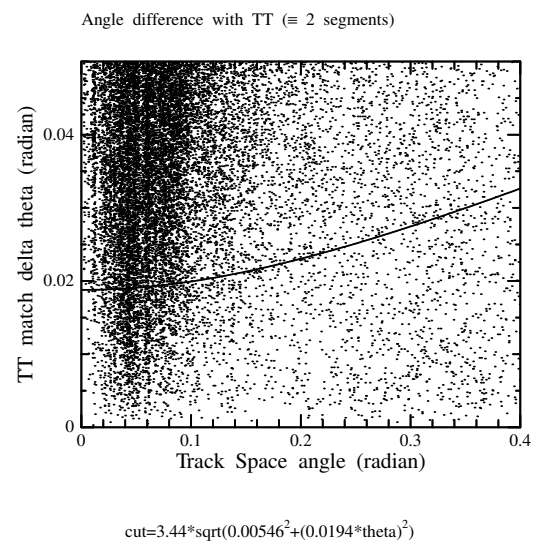
Figure 4.13: TT angle difference of 2 segment tracks.

Angle difference with TT

cut=3.44*sqrt(0.00546^2+(0.0194*theta)^2)
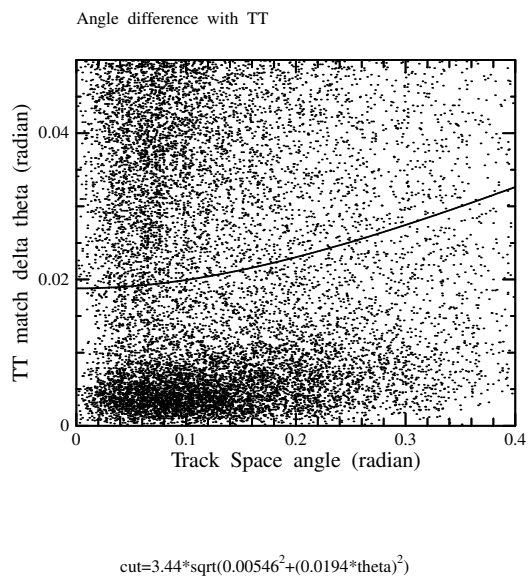
Figure 4.14: TT angle difference of 3 segment tracks.

Figure 4.15). $\Delta\theta_{global}$ is also a measure of the multiple scattering, and for a 100 $mrad$ track the threshold corresponds to about 10 $mrad$.
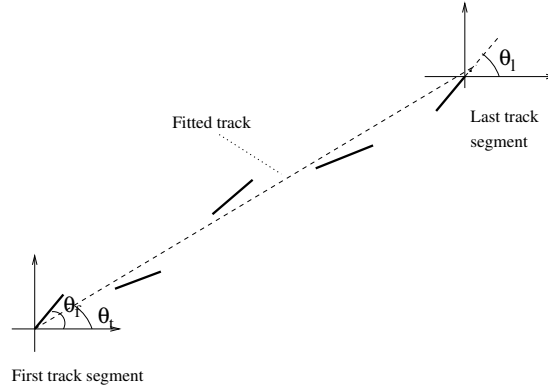
Figure 4.15: Global angle, θ_{global} is given by the difference between the angle of the fitted track θ_t and the square root of the sum of first (θ_f) and last (θ_l) segment's angles squared.

- The impact parameter (Figure 4.18) of the stopping track and the vertex point must satisfy the angle dependent condition (Figure 4.19),

$$IP > \sqrt{3^2 + (2\sigma_\theta.dx)^2} \qquad (4.4)$$

where $\sigma_\theta = \sqrt{(0.00305)^2 + (0.0194.\theta_t)^2}$ is the parametrization of the angular error, the first term in square root in the equation taking into account the minimum sensitivity of the instrument. On average, the minimum impact parameter corresponds to about 10 μm. dx is the distance of the vertex from the most upstream emulsion surface which is called vertex depth.

- The flight length of a candidate must be more than 25 μm.
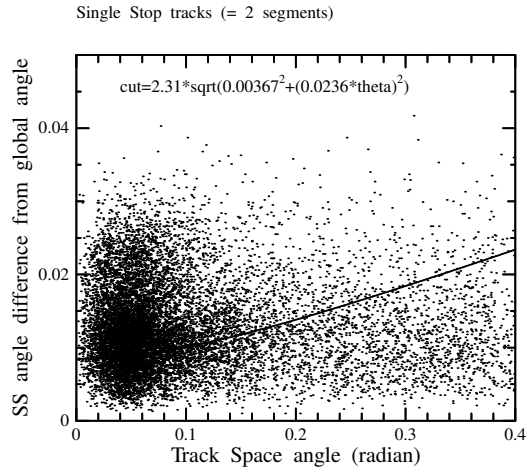
Figure 4.16: Global angle difference of 2 segment tracks
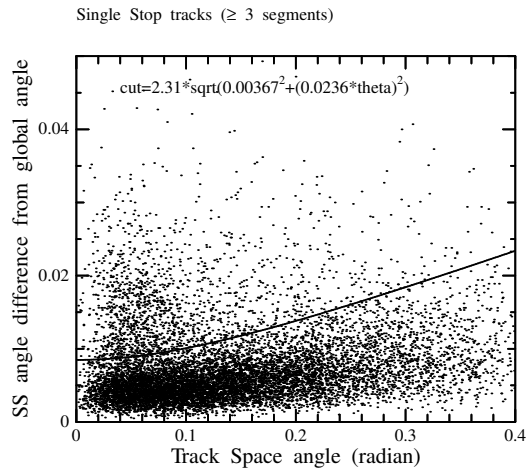
Figure 4.17: Global angle difference of 3 segment tracks.
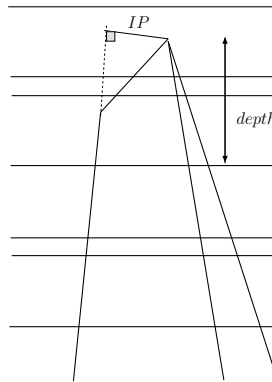
Figure 4.18: Definition of IP parameter.
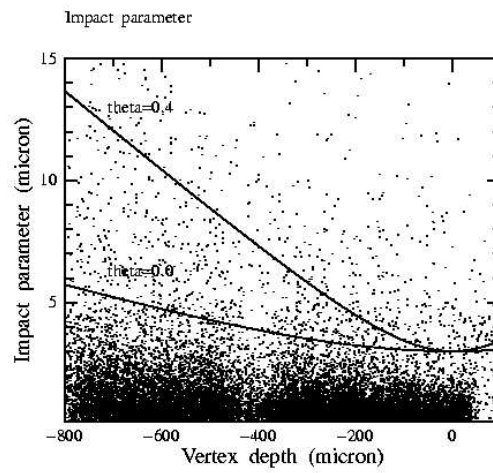
Figure 4.19: The impact parameter of the stopping track and the vertex point.

- $\chi^2 < 0.5$ cut is applied in order to suppress fake connections.

- Finally, it must be taken into account that π^0's are produced in neutrino(antineutrino) interactions. π^0 converts to γ pairs, which again convert to electron positron pairs. These tracks are almost collinear with the photon direction because their transverse momentum is negligible. Since the photons from pion decay point to the neutrino interaction vertex, the electron pairs tracks are also both pointing to the interaction vertex. Therefore, to reject events with electron pairs in which possibly only one of the tracks is matched, a cut on the minimum kink angle is applied: $\Delta\theta_{kink} > 10 \; mrad$. The kink angle is defined with respect to the line that links primary to decay vertex as shown in Figure 4.20.
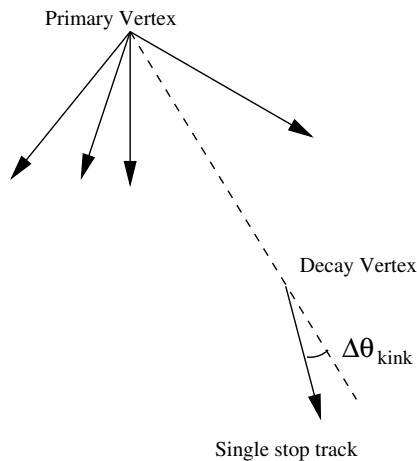
Figure 4.20: Definition of the kink angle with respect to the line which links primary to decay vertex. E-pair cut: $\Delta\theta_{kink} > 10 \; mrad$.

After the additional filtering the selection of decay candidates is performed. The selection is composed of six categories:

- Golden category: Two vertices are detected, the muon is attached to the primary vertex, and the secondary vertex has two daughter tracks which are reconstructed at TT. [5]

- Silver category: Two vertices are detected and in secondary vertex only one daughter track is TT matched.

- Bronze category: Two vertices are detected and in secondary vertex daughter tracks have only TT hits.

- Parent category: A muon is attached to the parent track, daughter track must be at least 2 segment connected.

- Isolated muon category: Only one vertex is found. A muon is reconstructed as a single stop, not attached to the vertex.

- Single stop category: Only one vertex and one separate TT track are found. Single stop track must be at least 2 segment connected.

These selection criteria were applied to the sample of 2480 located μ^+ events. A total of 152 events were selected for which a visual inspection was performed to confirm the decay topology. A secondary vertex found in the emulsion is tagged as

---

[5] If a track is connected by angular matching to the Target Tracker, it is called a TT match track. If a track is connected to Target Tracker raw hits, it is called a TThit track.

a decay vertex if no other activity (nuclear break-up or Auger electron) is observed at the decay point and if the number of outgoing tracks is consistent with charge conservation. Moreover, a decay into a single charged particle is accepted only if the angle between the parent and the decay product (kink angle) is greater than 50 $mrad$ and the flight length, i.e. the distance between the primary and decay vertices, is greater than 25 μm. To reduce further the ν_μ background in the present analysis, the primary vertex, to which the positive muon is attached, is required to be the most upstream one. After visual inspection, 51 events with a positive muon reconstructed in the spectrometer and a topology consistent with a charm decay were identified. The results of the visual inspection are given in Table 4.3 where the observable decay topologies are classified as even-prong decays N2 or N4 for neutral particles (mainly $\bar{D}^0$) and odd-prong decays C1, C3 or C5 for charged particles (mainly D^-, D_s^-), according to the prong multiplicity. The rejected sample consists mainly of neutrino-induced charm events in which

Table 4.3: Results of the visual inspection (eye-scan) of charm candidates

Secondary vertex topology	Number of events
N2	22
N4	9
C1	14
C3	4
C5	2

the reconstructed positive muon arises from a downstream charm decay vertex,

hadronic secondary interactions, delta-rays, or gamma conversions and events with a low-momentum track that, due to multiple scattering, appears to have a large impact parameter with the interaction vertex. The remaining part consists of fake vertices due to imperfections of the reconstruction program.

CHAPTER 5

MEASUREMENT OF ANTINEUTRINO CHARM

PRODUCTION

Charm production in neutrino and antineutrino charged current (CC) interactions has been studied by several experiments by looking at the presence of two oppositely charged leptons in the final state, from the process

$$\nu_\mu + d, s \rightarrow \ \mu^- + \ c + X$$

$$\downarrow$$

$$D^+ \rightarrow \mu^+ + \nu_\mu + X' \tag{5.1}$$

and

$$\bar{\nu}_\mu + \bar{d}, \bar{s} \rightarrow \ \mu^+ + \ \bar{c} + X$$

$$\downarrow$$

$$D^- \rightarrow \mu^- + \bar{\nu}_\mu + X' \tag{5.2}$$

The leading muon is interpreted as originating from the neutrino vertex and the other one, of opposite charge, as being the decay product of the charmed particle.

In particular CDHS [73], CCFR [74], CHARM [75], CHARM-II [76], NOMAD [77] and NuTeV [78] have collected a large statistics of opposite-sign dimuon events. In such experiments, the evaluation of the charm production cross section requires the knowledge of the average muonic branching ratio of the various charmed hadrons, weighted by their relative production rates. Furthermore, experiments of this type suffer from significant background ($\sim 20\%$) due to the undetected decay in flight of a pion or a kaon. The background reduction involves cuts on the energies of the primary and decay muons and this makes it difficult to study cross sections at energies below 20-30 GeV.

A different approach using a hybrid emulsion detector was pioneered by the E531 experiment at FNAL [79]. In emulsion, charmed particles can be recognized on the basis of their short flight length and characteristic decay topology. This allowed a study of all decay channels, not only the muonic one, applying loose kinematic cuts, with no required knowledge of branching ratios and with very low background.

A measurement of charm production and of the charm fractions f_h was obtained by E531. In this experiment, charm could be tagged by the presence of a detached secondary vertex in the emulsion target. 122 events were tagged in this way, 119 of which are neutrino induced and three induced by antineutrinos [80].

Antineutrino data at low neutrino energies are limited and no measurement of the production fractions $\bar{f}_h$ of the different charm species h exists.

97

CHORUS measured the average production cross section and its energy dependence by using $\bar{\nu}_\mu$CC interactions [81]. 32 charm candidates have been confirmed with an estimated background of 3.2 ± 04. The charm production rate in charged current induced by $\bar{\nu}_\mu$ was found to be

$$\frac{\sigma(\bar{\nu}N \to \mu^+ \bar{c}X)}{\sigma(\bar{\nu}N \to \mu^+ X)} = (5.0^{+1.4}_{-0.9}(\text{stat}) \pm 0.7(\text{syst}))\%.$$

And the ratio of the production fractions of neutral and charged charmed hadrons was found to be

$$\frac{f_{\bar{C}^0}}{f_{\bar{C}}} = 2.6^{+1.7}_{-1.0}(\text{stat}) \pm 0.8(\text{syst}).$$

In this thesis, we have analyzed an enlarged data sample obtained with additional event location.

5.1   Data Sample

In total, 2480 $\bar{\nu}_\mu$ events have been located in the emulsion and analyzed with the procedure discussed in Chapter 4. 46 events with topology consistent with a charm decay is found and given in Table 4.3.

In the following sections, we will describe MC simulation of the antineutrino charm production and background processes.

5.2   MC Simulation of Antineutrino Charm Production

The procedure of Monte Carlo simulation in the CHORUS experiment consists of modeling the neutrino beam, the generation of physical events, the simulation of the detector response and the reconstruction. The neutrino beams are simulated by GBEAM [38]. Parent mesons for neutrinos, modeled with FLUKA [82] by NOMAD [83], are feed into the CHORUS GEANT 3.21-based simulation of the CERN neutrino beam [84]. It simulates the interaction of a 450 GeV proton in the beryllium target and tracks hadronic shower through the neutrino tunnel and models meson decays into neutrinos. The output of the simulation is the flavor, the creation vertex and four momentum of the neutrino.

A large number of deep-inelastic neutrino interactions were simulated using the JETTA generator [85] which is based on LEPTO 6.1 [86] and JETSET [87]. Quasi-elastic (QE) interactions and resonance production events were generated with the RESQUE [88] package with a rate of 9.6% relative to deep-inelastic scattering reactions in the neutrino case and of 26% in the antineutrino case.

The simulated response of the electronic detectors was processed through the same reconstruction program, CHANT, as used for the experimental data. The tracks in emulsion and the performance of the track selector are also simulated in order to evaluate the efficiency of the scanning procedure.

The efficiency of the NetScan procedure represents the probability to recon-
struct the vertex and the decay topology of the charmed particle in the scanned
emulsion volume. In order to estimate NetScan efficiencies and numbers of the
background events for charm, MC simulation with the complete set-up and event
reconstruction has been performed.

In order to have realistic track density, NetScan data which do not contain
reconstructed vertices (empty data set) have been used. Empty data sets contain
tracks with stop or passing-through the NetScan fiducial volume representing the
real background.

For the empty data sets, specific scanning has not been performed. Instead
of this, some selection has been applied on the already scanned events. During
the scan back vertex location procedure, more than one track can be selected as
scan back tracks for scanning, or multi-candidates found in the interface sheets
are followed in the bulk emulsion. If these tracks stop in different emulsion
plates, each of them is assumed to possibly contain a vertex and NetScan data
taking is performed separately. If the scan back track is fake, the scanned fiducial
volume does not contain the neutrino interaction. Such a data set is stored in
the database and it is defined as an empty data set. For our analysis we have
selected 304 empty data sets. The distribution of empty data sets in the different
microscope stages is given in Table 5.1.

As mentioned before, in the NetScan procedure, all track segments around

Table 5.1: The number of empty data sets in the different microscope stages.

Map folder	Stage number	Number of data sets
Map-05-09-16-Anti-Emp1	Stage1	142
Map-05-09-16-Anti-Emp2	Stage2	15
Map-05-09-16-Anti-Emp3	Stage3	30
Map-05-09-16-Anti-Emp5	Stage5	34
Map-05-09-16-Anti-Emp6	Stage6	83

the located vertex are recorded within a given angular acceptance. And there are a few thousand tracks in one NetScan acquisition for each event. These tracks originate from neutrino interactions, cosmic rays and other background tracks due to other beams during the exposure of CHORUS emulsions. In the real case, emulsion plates are misaligned with respect to each other. Several hardware effects during the scanning procedure have to be taken into account. In order to evaluate the NetScan efficiency, all these aspects need to be reproduced. This was achieved by superimposing Monte Carlo events with empty data sets. This is a very realistic way to simulate the background conditions in the NetScan procedure. The scheme of Monte Carlo simulation [89] is shown in the Figure 5.1.

Starting from the Monte Carlo true track parameters of all charged particles in a simulated neutrino interaction, each track is propagated from production point through the NetScan fiducial volume, taking into account the multiple scattering as well as the measurement error and the emulsion distortions, to get the position and direction of each track segment at the upstream surface of each plate.

The number of frames (up to sixteen) where a grain is found, at the so-called pulse height, depends on the hardware efficiency. Using a large number of background tracks, the pulse-height distribution was parameterized as a function of the radial and transverse angle of the track, independently for each emulsion module. This parameterization was used to simulate pulse-height and took into account the hardware efficiency and the developing process that may result in different fog density and distortion [89]. Finally, to take into account the misalignment of the plates, the parameters of the inverse alignment transformation for the tracks in the empty data set are applied on the simulated segments to obtain segments in the same coordinate system as the raw data in the data set. In other words, misalignments are introduced for Monte Carlo tracks using alignment parameters associated to scanned emulsion plates. In doing so, the Monte Carlo data set includes an event with known physical characteristics that can be treated in exactly the same way as real data. The combined data are passed through the same NetScan reconstruction and selection programs used for real data.

The location efficiencies, the ratio of the number of located events to the number of interactions in emulsion, are given in Table 5.2.

The NetScan efficiency is a function of many variables: charm species, flight path, energy of the charmed hadron, number of prongs (decay daughters), etc.

102
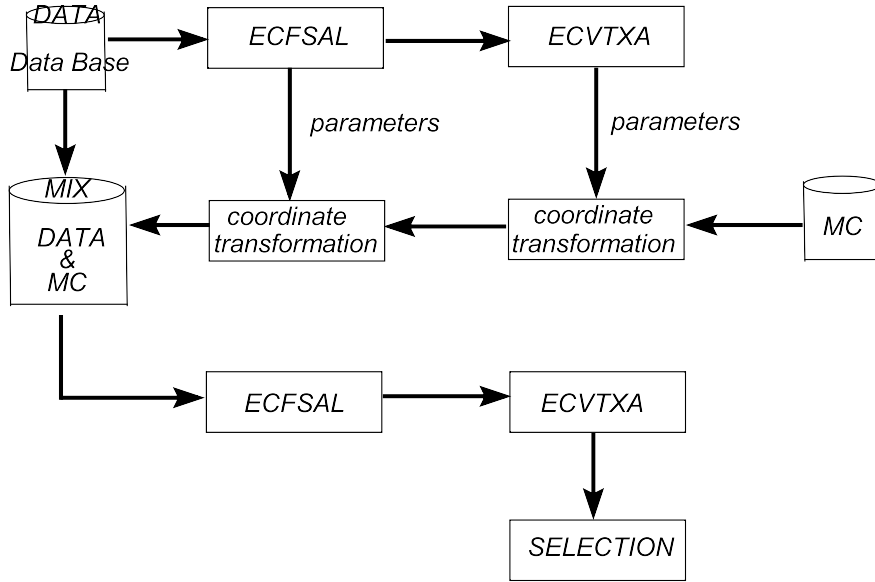
Figure 5.1: The flowchart of NetScan simulation [89].

Table 5.2: Location efficiencies.

Event	Location efficiency (%)
$\bar{\nu}_\mu CC$ DIS+0.26QE	54.9±0.3
D^0	47.4±0.5
D^-	46.4±0.9
D_s^-	43.6±1.8
$D^- + D_s^-$	44.6±1.5

The NetScan efficiencies, containing both the geometrical acceptance and the reconstruction efficiency, are shown in Table 5.3 for each decay topology. The contribution from charmed $D^\pm$ and $D_s^\pm$ mesons was evaluated assuming $D_s^+/D^+ = 0.627 \pm 0.073$ [90] and the production ratio as obtained in [53, 57]. The errors include the effect of Monte Carlo statistics used for the efficiency evaluation, instrumental effects, and the uncertainty on D_s^+/D^+. And the contribution of $\bar{\Lambda}_c$ was neglected.

Table 5.3: NetScan efficiency containing geometrical acceptance and reconstruction efficiency for decays of neutral and charged charmed hadrons for different decay topologies in the $\bar{\nu}_\mu$-induced CC events.

	$\bar{D}^0$
ϵ_{N2} (%)	66.9 ± 0.8
ϵ_{N4} (%)	79.2 ± 1.5
	$D^- + D_s^-$
ϵ_{C1} (%)	41.3 ± 3.6
ϵ_{C3} (%)	72.5 ± 2.6
ϵ_{C5} (%)	66.4 ± 10.1

Figures 5.2, 5.3 and 5.4 show the efficiency dependence as a function of the flight length for each charm species and for each decay topology. The low value of the selection efficiency at short flight lengths is explained by the difficulty to separate the two vertices. If a track from the secondary vertex appears to be attached to the primary then the efficiency to reconstruct the secondary vertex becomes lower. At long flight paths the selection efficiency goes down; because the decay point is quite close to the edge of the fiducial volume, then only a few

secondary tracks can be reconstructed. The simulation shows that approximately

3% of D^0 decay out of the fiducial volume, and similarly 13% of D^-, 7% of D_s^-.
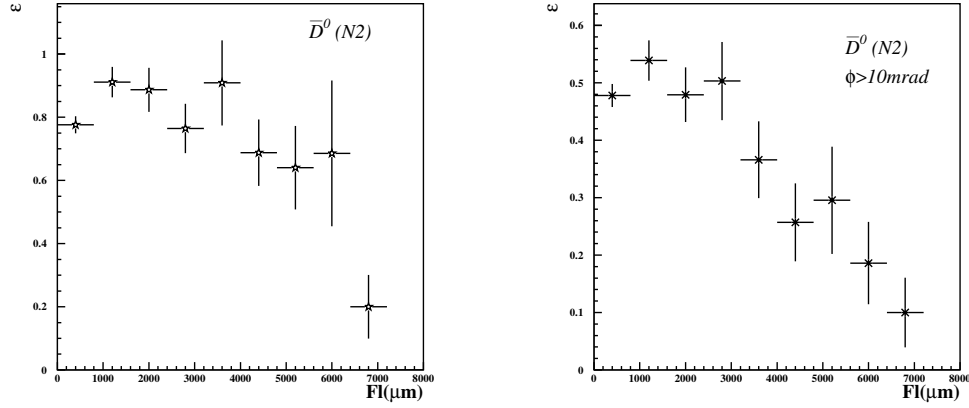
Figure 5.2: Dependence of the charm selection efficiency as a function of the flight path for $\bar{D}^0$ decaying into two prongs **Left:** without coplanarity cut, **Right:** with coplanarity cut $\phi > 10\ mrad$.
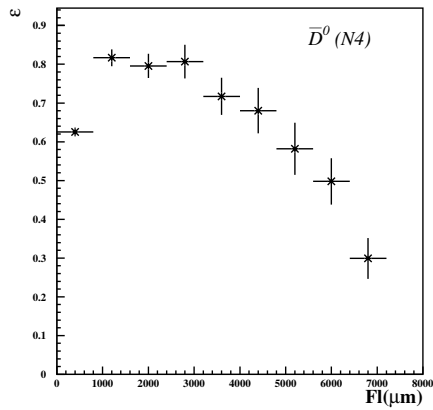
Figure 5.3: Dependence of the charm selection efficiency as a function of the flight path for $\bar{D}^0$ decaying into four prongs.
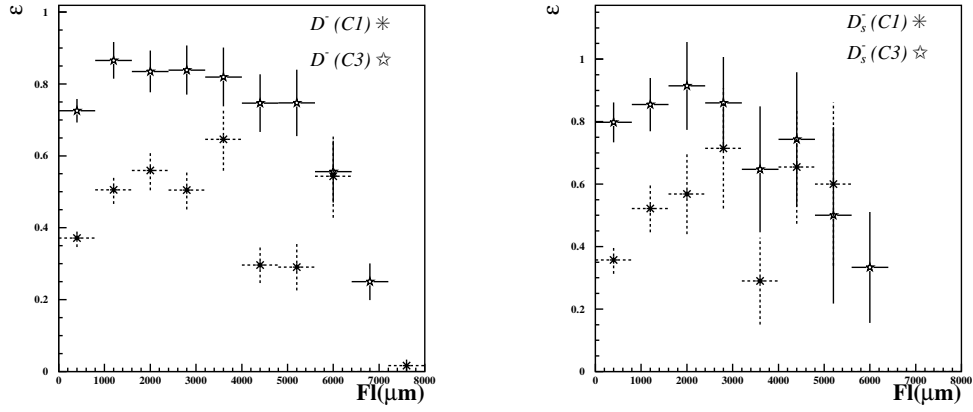
Figure 5.4: Dependence of the charm selection efficiency as a function of the flight path for **Left:** D^- and **Right:** D_s^- decaying into one and three prongs.

5.3 Background Estimations

The main background for the neutral charm $(\bar{D}^0)$ detection in emulsion comes from K^0, Λ^0 decays, and from neutron, K^0 and Λ^0 white interactions, without any visible nuclear break up at the interaction point. For the charged charmed hadrons (D^-, D_s^-) the main background coming from π, K and Σ decays in flight, and from charged hadron interactions without any visible track from nuclear break up (these are called white kinks/tridents).

5.3.1 Strange Particle Background

Although strange particles have much longer mean decay length, they can fake a charm topology. For two prong topology (N2) the main background comes from

- $K_s^0 \rightarrow \pi^+\pi^-$ with $Br = 68.60 \pm 0.27$ %,

- $\Lambda^0 \rightarrow P\pi^-$ with $Br = 63.9 \pm 0.5$ %.

The full simulation of the electronic detectors and of the event reconstruction in the emulsion is used to calculate the background from these neutral strange particle decays. The location and NetScan efficiencies for each background particle are shown in Table 5.4.

Table 5.4: Efficiencies for background particles.

Background particle	Location efficiency (%)	NetScan efficiency (%)
K_s^0	60.1 ± 1.5	3.1 ± 1.0
Λ^0	46.5 ± 0.9	3.8 ± 1.3

The number of background events per charged event was evaluated and finally the total number of background events was obtained for the antineutrino data sample. The results are shown in Table 5.5 and Table 5.6.

Table 5.5: The number of background events per CC event.

Background particle	Detectable bg events	Bg per CC event (10^{-4})
K_s^0	8.5	5.98 ± 2.12
Λ^0	8	6.36 ± 2.18

Table 5.6: Number of background events in antineutrino data sample.

Background particle	Bg events	Bg events with $\phi > 10mrad$
K_s^0	1.31 ± 0.42	0.16 ± 0.16
Λ^0	1.39 ± 0.48	0.49 ± 0.27

The rejection of e^+e^- pairs is obtained by applying the cut on the opening angle.

Other background coming from multi prong decays is estimated to be $N_{bg}^{N4} = 0.29 \pm 0.02$ events.

5.3.2 White Interactions

Hadronic white interactions are elastic or inelastic hadronic nuclear interactions with no heavily ionizing tracks or other evidence of nuclear break-up, i.e., blobs, delta rays or Auger electrons, that mimic a decay kink topology. These interactions fake a one prong decay of a charmed particle and cannot be distinguished from a decay in the emulsion.

White kinks were generated by using the event generator WHINTER (WHite INTERactions) [91] and processed through the full simulation chain. Selection criteria reduce the white kink background. Kinks with an angle smaller than $30\ mrad$ are difficult to be recognized in emulsion. In order to reduce white kink background, a cut on kink angle $\theta_{kink} > 50\ mrad$ was applied.

The number of expected white kink interactions in our sample of charm events is given by:

$$N_{WK}^{C1} = \frac{L_{had}}{\lambda_{WK}} \times \varepsilon_{sel}^{C1} \tag{5.3}$$

where

- L_{had} is the total hadronic track length. To evaluate L_{had}, all the reconstructed track, except the muon, in the NetScan volume was considered. $L_{had} = N_{CC}^{\bar{\nu}_\mu} \times \langle n_{ch} \rangle \times L_{emulsion} = 43811.5mm$. Here $L_{emulsion} = 10$ emulsion plates, $7.9\ mm$, and $\langle n_{ch} \rangle$ is 2.53 ± 0.11 [5].

- λ_{WK} is the interaction length for a hadron produced in neutrino charged current interactions. For CHORUS neutrino spectrum, the interaction length in emulsion is estimated to be $2.5 \pm 0.5\ m$ by using the FLUKA [92] simulation program.

- $\varepsilon_{sel}^{C1} = (19.8 \pm 1.1)\%$ is the efficiency of the white kink selection with NetScan on 1-prong events.

Calculation gives the white kink events in C1 to be $N_{WK}^{C1} = 3.47 \pm 0.19$ events. Hadronic interactions in 3-prong topology are also estimated to be $N_{WK}^{C3} = 0.77 \pm 0.03$ events.

5.4   Measurements of Charm Production Induced by Antineutrinos

In order to obtain the sample of $\bar{\nu}_\mu$CC interactions, one has to subtract from this sample the contaminations [72] due to:

- ν_μCC events with the μ^- reconstructed as a μ^+;

- ν_μ induced dimuon events for which the primary μ^- is not reconstructed while the μ^+ coming from the charm hadron decay is seen;

- punch through hadrons traversing the 5.2 interaction lengths of the calorimeter and reconstructed as μ^+ in the spectrometer, in CC events with the μ not identified, or in NC interactions;

- π^+, K^+ decays to μ^+.

The contaminations to the sample of 2480 μ^+ events, shown in Table 5.7 , have been subtracted statistically to determine the total number of $\bar{\nu}_\mu$CC interactions.

Table 5.7: Estimated contaminations to the sample of μ^+ located events.

μ^+ sample	2480 events
NetScan acquisition bug	84
$\mu^- \mu^+$ events	41
2 DC hits events	84
μ^+ from charm decay	9
wrong μ^- reconstruction	26
$\nu_\mu CC$	11.6 $\pm$1.1(stat)
$\nu_\mu NC$	32.7 $\pm$3.1(stat)

Table 5.8 shows the number of charm candidates after the subtraction of contaminations to the sample of μ^+. Figure 5.5 shows the flight length distribution of charm candidates. Appendix 9.1 summaries the detail of the charm candidates.

Table 5.9 shows the decay topologies of 46 events surviving the estimated residual background for each topology, and the number of events after background subtraction, weighted with the inverse of the NetScan efficiency. By using the unified approach for the analysis of small signals in presence of background [93],

Table 5.8: Charm candidates after subtracting the contamination to the μ^+ sample.

Secondary vertex topology	Number of events
N2	19
N4	9
C1	14
C3	4
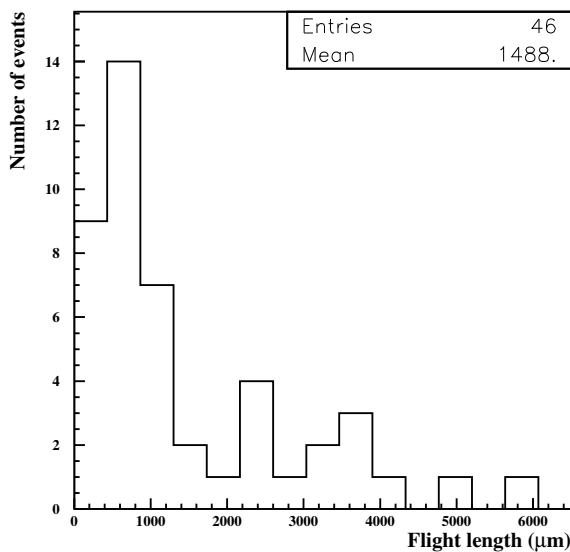
Figure 5.5: Flight length distributions for charm candidates.

the statistical error can be derived at the 68.27% (1σ) confidence interval.

Taking into account the estimated efficiencies and background described in Sec. 5.3, and the measured branching ratio of $\bar{D}^0$ to all neutrals of $0.218\pm0.049\pm$ 0.036 [54], the charm production rate can be obtained.

Table 5.9: Charm events and estimated backgrounds for each decay topology. The last column gives the final sample of events after background subtraction and NetScan efficiency correction

Decay topology	Events	Background	Weighted sample
N2	19	2.70 ± 0.64	$24.4^{+7.2}_{-6.3}$(stat) ± 0.3(syst)
N4	9	0.29 ± 0.02	$11.0^{+4.8}_{-3.4}$(stat) ± 0.2(syst)
C1	14	3.47 ± 0.19	$25.5^{+10.4}_{-9.0}$(stat) ± 2.2(syst)
C3	4	0.77 ± 0.03	$4.5^{+3.8}_{-2.3}$(stat) ± 0.2(syst)
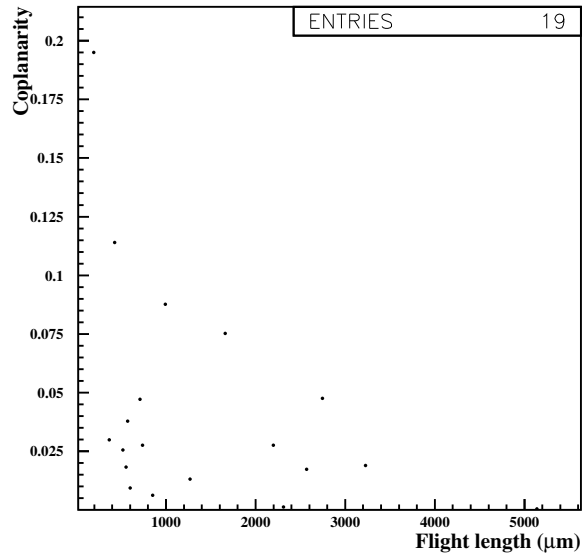
Figure 5.6: Coplanarity versus flight length distribution for N2 topology.

$\bar{D}^0$ **production rate** can be defined as:

$$\frac{\sigma(\bar{\nu}_\mu N \to \mu^+ \bar{D}^0 X)}{\sigma(\bar{\nu}_\mu N \to \mu^+ X)} = \frac{\frac{N_{N2}^{obs.}}{\epsilon_{N2}} + \frac{N_{N4}^{obs.}}{\epsilon_{N4}}}{1 - BR(D^0 \to All\ neutral)} \cdot \frac{\epsilon_{loc.}^{\bar{\nu}_\mu}}{\epsilon_{loc.}^{\bar{D}^0}} \cdot \frac{1}{N_{CC}^{\bar{\nu}_\mu}} \%. \qquad (5.4)$$

In the present sample of 2192 events, the number of background events is evaluated to be 2.70±0.64 and 0.29±0.02 in N2 and N4 decay topologies respectively. Further reduction of background can be achieved in N2 decay topologies by acoplanarity angle[1] selection, $\phi > 10 mrad$. By using this selection, the background event is reduced to 0.66±0.32 in N2 sample. By applying the acoplanarity cut, the NetScan efficiency for V2 topology becomes (45.9±0.9)%. Then $\bar{D}^0$ **production rate** has been measured to be

$$\frac{\sigma(\bar{\nu}_\mu N \to \mu^+ \bar{D}^0 X)}{\sigma(\bar{\nu}_\mu N \to \mu^+ X)} = (2.86^{+0.71}_{-0.59}(\text{stat}) \pm 0.14(\text{syst}))\% \qquad (5.5)$$

where the systematic uncertainty of the production rate rises mainly from the choice of event generator and from variations of data quality. The total systematic error estimated to be 5% [53]. The statistical error was derived by using the 68.27% (1σ) confidence interval in the unified approach for the analysis of small signals in presence of background [93].

D^-, D_s^- **production rate** can be defined as:

$$\frac{\sigma(\bar{\nu}_\mu N \to \mu^+ (D^-, D_s^-) X)}{\sigma(\bar{\nu}_\mu N \to \mu^+ X)} = \left(\frac{N_{C1}^{obs.}}{\epsilon_{C1}} + \frac{N_{C3}^{obs.}}{\epsilon_{C3}}\right) \cdot \frac{\epsilon_{loc.}^{\bar{\nu}_\mu}}{\epsilon_{loc.}^{(D^- + D_s^-)}} \qquad (5.6)$$

---

[1] Coplanarity angle,ϕ, is the angle between the line of flight of the neutral primary and the plane defined by the tangents to the lines of the secondaries at the vertex point. Figure 5.6 shows the coplanarity versus flight length distribution of 2-prong decay topology.

and has been measured to be

$$\frac{\sigma(\bar{\nu}_\mu N \rightarrow \mu^+(D^-, D_s^-)X)}{\sigma(\bar{\nu}_\mu N \rightarrow \mu^+ X)} = (1.69^{+0.62}_{-0.52}(\text{stat}) \pm 0.24(\text{syst}))\% \qquad (5.7)$$

where the systematic errors include the effect of Monte Carlo statistics used for the efficiency evaluation, instrumental effects (4.6%), location effect (2%) [53] and the uncertainty on D_s^+/D^+. And the contribution of $\bar{\Lambda}_c$ was neglected. In total the systematic error is estimated as 14%.

Hence the total charm production rate can be obtained

$$\begin{aligned}
\frac{\sigma(\bar{\nu} N \rightarrow \mu^+ \bar{c} X)}{\sigma(\bar{\nu} N \rightarrow \mu^+ X)} &= \frac{\sigma(\bar{\nu}_\mu N \rightarrow \mu^+ \bar{D}^0 X)}{\sigma(\bar{\nu}_\mu N \rightarrow \mu^+ X)} + \frac{\sigma(\bar{\nu}_\mu N \rightarrow \mu^+(D^-, D_s^-)X)}{\sigma(\bar{\nu}_\mu N \rightarrow \mu^+ X)} \\
&= (4.55^{+0.96}_{-0.81}(\text{stat}) \pm 0.64(\text{syst}))\%. \qquad (5.8)
\end{aligned}$$

The ratio of the production fractions of neutral and charged charmed hadrons measured to be

$$\frac{\sigma(\bar{\nu}_\mu N \rightarrow \mu^+ \bar{D}^0 X)}{\sigma(\bar{\nu}_\mu N \rightarrow \mu^+(D^-, D_s^-)X)} = 1.69^{+0.75}_{-0.63}(\text{stat}) \pm 0.21(\text{syst}). \qquad (5.9)$$

This result has to be compared with a value of about 1.0 obtained in the neutrino case [53, 57], supporting the expectation that the charmed baryon production is strongly suppressed in antineutrino interactions.

New measurements are in a good agrement with the previous results based on the sample of 32 $\bar{\nu}_\mu$ charm events [81].

CHAPTER 6

PENTAQUARK SEARCH IN THE CHORUS EXPERIMENT

The first experimental observation of pentaquarks came in July 2003 from the LEPS Collaboration at the SPring-8 facility in Japan [94]. They observed a sharp resonance Θ^+ with quark contents $uudd\overline{s}$ at 1.54 ± 0.01 GeV with a width smaller than 25 MeV and a statistical significance of 4.6σ in the $\gamma C_{12} \rightarrow K^+K^-X$ reaction (see Figure 6.1). This resonance decays into K^+n, hence carries strangeness S=+1. This result was shortly thereafter confirmed by the CLAS Collaboration [95, 96] by analyzing existing data on deuteron target looking at the channel $\gamma d \rightarrow K^-K^+np$. A peak was observed in the nK^+ invariant mass at a value of 1542 ± 5 MeV, with a width less than 21 MeV, and a statistical significance of more than 5σ. This result has triggered new interest in baryon spectroscopy since this baryon is manifestly exotic; that is, it cannot be composed of three quarks but may be explained as a bound state of five quarks. Several other groups have confirmed this result. Table 6.1 lists the experiments claiming evidence for pentaquark states. While pentaquark signals observed in each experiment suffered

115

from low statistics, the observation in many different reactions using different probes (photons, electrons, protons, neutrinos) and targets (protons, neutrons, nuclei) supported the pentaquark existences. On the contrary, subsequent re-analysis of data collected in a different set of experiments [108, 121] found no evidence of pentaquarks. The recent repetitions [122] of some of the previous experiments that claim positive evidence of Θ^+ pentaquark state yield null results and contradict the previous observations.
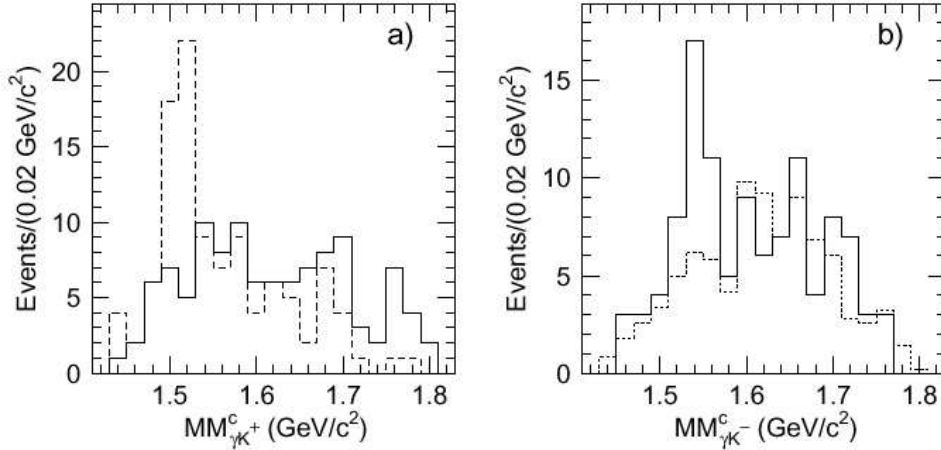
Figure 6.1: Missing mass spectra for the **Left:** γK^+ and **Right:** γK^- for the reaction $\gamma C \rightarrow K^+ K^- X$ [94]. The dashed (solid) histogram shows events with (without) additional detected proton. The Λ signal is seen on the left and evidence for Θ^+ is seen on the right.

The evidence for the cascade pentaquarks, Ξ_5^{--} and Ξ_5^0, have been announced in the $\Xi^- \pi^-$ and $\Xi^- \pi^+$ in pp collisions at $\sqrt{s} = 17.2$ GeV by the NA49 experiment at CERN [106]. The reported mass is 1.862 GeV/c^2 (see Figure 6.2).
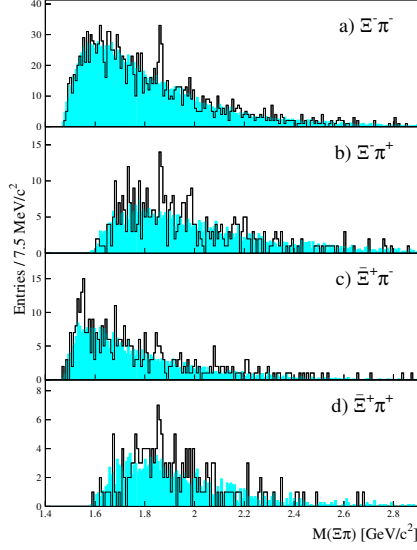
Figure 6.2: Invariant mass spectra for **(a)** $\Xi^-\pi^-$, **(b)** $\Xi^-\pi^+$, **(c)** $\bar{\Xi}^+\pi^-$, and **(d)** $\bar{\Xi}^+\pi^+$ in the NA49 experiment. The shaded histograms are the normalized mixed-event backgrounds.

The evidence for the anticharmed pentaquark, Θ_c, comes from H1 Collaboration at HERA [107], in the $D^{*+}\bar{p}$ and $D^{*-}p$ modes at a mass of $3099 \pm 3(\text{stat}) \pm 5(\text{syst})$ MeV and a measured Gaussian width of $12 \pm 3(\text{stat})$ MeV, compatible with the experimental resolution. Figure 6.3 shows the D^*p invariant mass spectrum from oppositely charged D^*p combinations in deep-inelastic scattering. It is anticharmed analogue of the $\Theta^+(1540)$ and has the quark content $uudd\bar{c}$ with spin-1/2 or -3/2. This is the first exotic baryon with anticharm quark, implying the existence of other exotic baryons with heavy quarks. Nowak *et al.* [126] claimed that the observed H1 pentaquark is a chiral partner of the yet undiscovered ground state Θ_c^0 with opposite parity and a mass of order 2700 MeV. However, a similar

117

search with larger statistics has been performed by the ZEUS [123] and FO-CUS [114] collaborations did not confirm this signal. ALEPH [108], CDF [112], BELLE [110] have also announced null search results on a strongly decaying charmed pentaquark.
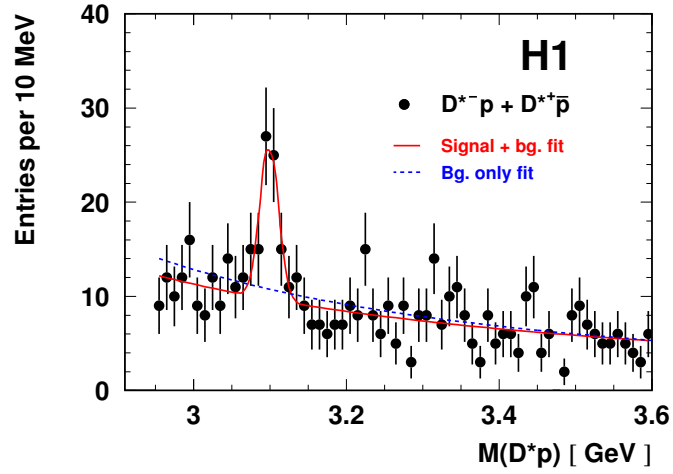
Figure 6.3: Invariant mass of the D^*p system; the D^* mesons have been reconstructed in the decay channel $D^* \to D^0\pi_s \to K\pi\pi_s$.

The pentaquark with anticharm has been seen only by H1 collaboration and studied in quark models [124], Skyrme model [125] and in other theorical approach such as diquark-diquark-antiquark of Jaffe and Wilczek [25], a diquark-triquark model of Karliner and Lipkin [29].

Table 6.1: Positive signals for pentaquark states.

Experiment	Reaction	State	Mode	Mass(MeV)
LEPS(1) [94]	$\gamma C_{12} \rightarrow K^+K^-X$	Θ^+	K^+n	1540 ± 10
CLAS(d) [95]	$\gamma d \rightarrow K^+K^-(n)p$	Θ^+	K^+n	1542 ± 5
CLAS(p) [96]	$\gamma p \rightarrow K^+K^-\pi^+(n)$	Θ^+	K^+n	1555 ± 10
SAPHIR [97]	$\gamma p \rightarrow K_S^0 K^+(n)$	Θ^+	K^+n	1540 ± 6
COSY [98]	$pp \rightarrow \Sigma^+ K_S^0 p$	Θ^+	$K_S^0 p$	1530 ± 5
JINR [99]	$p(C_3H_8) \rightarrow K_S^0 pX$	Θ^+	$K_S^0 p$	1540 ± 8
SVD [100]	$pA \rightarrow K_S^0 pX$	Θ^+	$K_S^0 p$	1526 ± 5
DIANA [101]	$K^+Xe \rightarrow K_S^0 p(Xe)'$	Θ^+	$K_S^0 p$	1539 ± 2
νBC [102]	$\nu A \rightarrow K_S^0 pX$	Θ^+	$K_S^0 p$	1533 ± 5
NOMAD [103]	$\nu A \rightarrow K_S^0 pX$	Θ^+	$K_S^0 p$	1528.7 ± 2.5
HERMES [104]	quasi-real photoproduction	Θ^+	$K_S^0 p$	1526 ± 3
ZEUS [105]	$ep \rightarrow K_S^0 pX$	Θ^+	$K_S^0 p$	1522 ± 3
NA49 [106]	$pp \rightarrow \Xi\pi X$	Ξ_5	$\Xi\pi$	1862 ± 2
H1 [107]	$ep \rightarrow (D^*p)X$	Θ_c	D^*p	$3099 \pm 3(\text{stat}) \pm 5(\text{syst})$

6.1 Pentaquark Search in CHORUS

A search for pentaquark production in $\bar{\nu}_\mu$CC interaction has been performed in the CHORUS experiment. Our search is based on the visual observation of the pentaquark decay vertex and identification of the daughter proton as shown in Figure 6.4. In the following section, the analysis strategy adopted to the CHORUS experiment [127] will be discussed.

6.1.1 Analysis Strategy

If the mass of the Θ_c^0 below DN threshold, the Θ_c^0 decays weakly. In our search, we focus on the decay channels with a proton. The possible weak decays
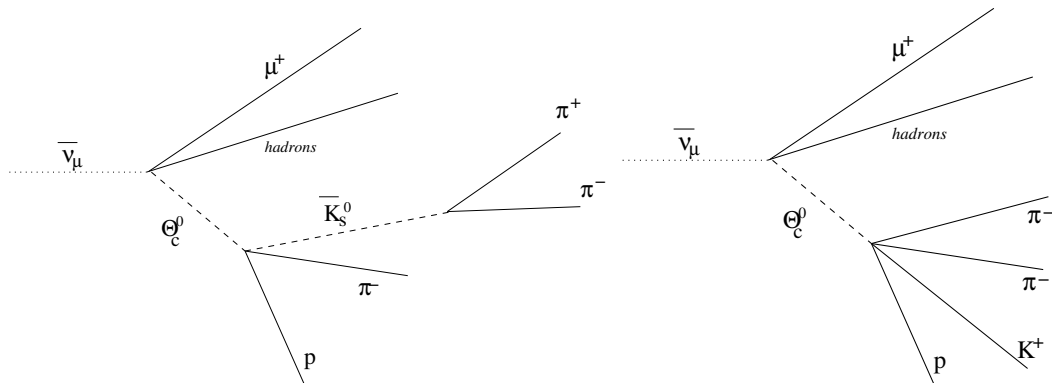
Figure 6.4: Decay topology of the Θ_c^0 events produced in $\bar{\nu}_\mu$ interactions with two and four prongs.

of the Θ_c^0 with a proton in the final state would be;

$$(i) \quad \Theta_c^0 \to pK_s^0\pi^-(l\nu_l),$$

$$(ii) \quad \Theta_c^0 \to pK_s^0\pi^0\pi^-(l\nu_l),$$

$$(iii) \quad \Theta_c^0 \to pK^+\pi^-\pi^- \quad etc. \tag{6.1}$$

Given the fact that Θ_c^0 can decay via either the annihilation or the decay of the $\bar{c}$ quark, and the lifetime of the Θ_c^0 can be expected to be longer or shorter than that of the charm hadron state, Table 6.2.

Table 6.2: The lifetime of charmed hadrons.

	D^0	D^+	D_s^+	Λ_c^+
cτ (μm)	123.0	311.8	147.0	59.9

Some experiments[1] [128, 129] claim observation of longer lifetime neutral

---

[1] The following experiments claim observation of longer lifetime neutral charmed hadrons:

- E531 experiment [129] observed one candidate for the production and decay of a long

charmed hadrons compared to D^0. Therefore, the experimental searches of pentaquark must cover a wide range of possible lifetimes.

Possible background sources for the Θ_c^0 decays are mainly decays of $\bar{D}^0$, K^0, Λ^0, and "white" interactions of a neutral hadron. Since the Θ_c^0 decays into at least three particles, the non-coplanarity of the two charged prongs and the Θ_c^0 itself rules out the Λ^0 decay. Concerning the 4-prong decay topology, such an events may be the background only if one of its daughter is wrongly identified as a proton. The contribution of white interactions is negligible.

As mentioned in Sec. 4.6, from a present sample of μ^+ events, 46 events with a topology consistent with a charm decay were found. To search for anticharmed pentaquark, the proton identification was performed on the decay daughters of the secondary vertex with an even multiplicity.

In the following section the proton identification method is discussed in detail.

6.1.2   Proton Identification

In nuclear emulsions, minimum ionizing particles (MIPs) are observed as thin tracks with a grain density of about $30 grains/100\mu m$. The grain density in emulsion is almost proportional to the electronic energy loss and its mean rate is

---

lived high mass neutral baryon with a decay mode:

- $p\pi^- K_s^0$ mass= $2450 \pm 14 MeV/c^2$ with a lifetime $77.2 \pm 0.910^{-13}s$. or
- $pK^- K_s^0$ mass= $2647 \pm 11 MeV/c^2$ with a lifetime $83.4 \pm 0.910^{-13}s$.

• SLAC Hybrid Facility Photon Collaboration [128] observed an event of $\bar{D}^0 \rightarrow K^+\pi^+\pi^-\pi^-$ with a lifetime of $55.410^{-13}sec$.

given by the Bethe-Bloch equation [130],

$$-\frac{dE}{dx} = Kz^2\frac{Z}{A}\frac{1}{\beta^2}\left[\frac{1}{2}\ln\frac{2m_ec^2\beta^2\gamma^2T_{\max}}{I^2} - \beta^2 - \frac{\delta}{2}\right].$$

This equation foresees that, in a given material, dE/dx is a function of the particle velocity (β). Therefore, if the momentum is known, the measurement of dE/dx along the particle trajectory allows particle identification.

On this basis, the discrimination between pions and protons of 1.2 GeV/c momentum with a statistical accuracy larger than 3σ was achieved by using track path lengths of about 2.6 mm [131]. The method consists of counting the grains along the track paths by the automatic scanning microscopes. This information allows the extrapolation to different path lengths and β values.

The measurement of Multiple Coulomb Scattering (MCS) can be used to estimate $p\beta$ [132], where p is the particle momentum. Therefore, the combination of dE/dx measurement and the multiple scattering can provide particle identification. The momentum resolution can be parametrized as $\Delta p/p = \sqrt{a^2 + (bp)^2}$ where a and b are constants which are inversely proportional to the traversed length and proportional to the position resolution.

In the Θ_c^0 search in $\bar{\nu}_\mu$CC interactions, kaons from D^0 decays are the main source of background if they are identified as protons.

The grain density of proton, kaon and pion tracks in emulsion with different flight lengths and velocities were simulated. The momentum resolution is also simulated according to the composition of the traversed material and the position

122

resolution.

All tracks from $\bar{\nu}_\mu$ interaction vertex followed in emulsion and track parameters, pulse height, slopes were recorded for dE/dx and $p\beta$ analysis. The average track length in the emulsion was measured to be 13.2 mm [133]. In Figure 6.5, a scatter plot of the dE/dx versus $p\beta$ as measured by MCS is shown. The simulation shows a proton identification efficiency of 0.10±0.01% for N2 topology and 1.52± 0.04% for N4 decay topology. The momentum resolution is about 30% by MCS and dE/dX resolution is about 8%. As seen in the Figure 6.6, there is no particle identified as a proton in the signal region: $p\beta$ between 0.2 to 2 GeV/c with $dE/dX > 1.9\frac{\text{MeV}}{(g/cm^2)}$.

6.2   Event Simulation

In order to simulate the Θ_c^0 production in $\bar{\nu}_\mu$ interactions, it is assumed that the energy dependence of the Θ_c^0 production cross section in $\bar{\nu}_\mu$CC interactions is the same as the D^0 production in ν_μCC interactions reported in Ref. [53]. This dependence is convoluted with the energy spectrum considered (the CERN Wide Band beam) to give the effective energy spectrum of Θ_c^0 events (Figure 6.7). By using Vegas generator [134], the $\bar{\nu}_\mu$ interactions were generated by integrating the tree level matrix element of the $\bar{\nu}_\mu$ scattering off a $\bar{s}$ quark in the nucleon which produce a μ^+ and a $\bar{c}$ quark in the final state.

Once the $\bar{c}$ quark is produced, it has to hadronize into the Θ_c^0 hadron. The
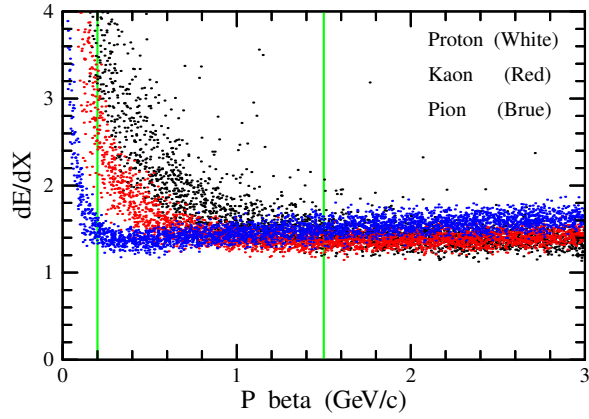
Figure 6.5: Scatter plot of the number of measured grains versus $p\beta$ (GeV/c) measured by MCS.
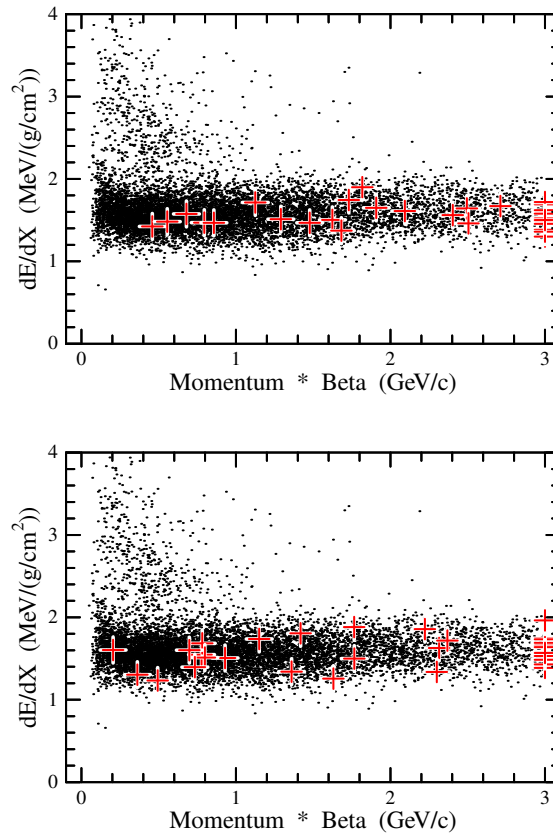
Figure 6.6: Scatter plot of the dE/dx versus $p\beta$ (GeV/c) measured by MCS, where the red marks are the decay daughters. **Top:** N2 sample, **Bottom:** N4 sample.
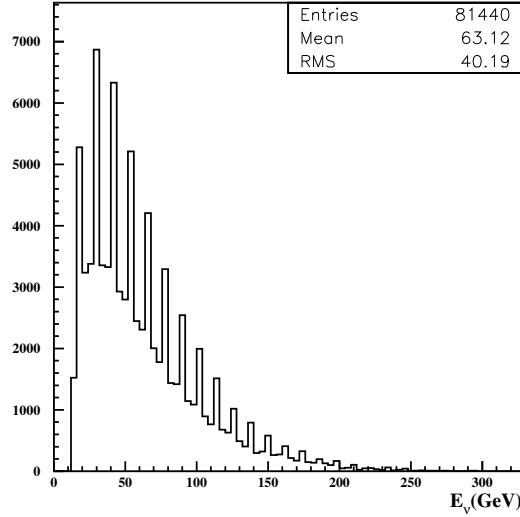
Figure 6.7: $\bar{\nu}_\mu$ energy spectrum generated by using Vegas generator.

description of the charm quark fragmentation is done in terms of the variable

$z = p_{had}/p_{quark}$ with two different models [135, 136]. They foresee a z range

between 0 and 1. As it was already pointed out in Ref. [137], this description

partially fails in fixed target experiments where the charm quark may fragment

into a charmed hadron with valence quarks. This is the case of Λ_c and Θ_c^0 baryon

production in ν_μ and $\bar{\nu}_\mu$ interactions, respectively. The HERWIG simulation

program [138] is used to get the z variable distribution for Λ_c production as

shown in Fig. 6.8 where the $z \geq 1$ part is due to valence quarks only. The same

distribution for the Θ_c^0 production is used.

The final arrangement of the valence quarks is considered to be as in Fig. 6.9

and HERWIG is used to produce hadrons from the other prompt partons via the

Entries	3627
χ²/ndf	76.30 / 59
P1	96.15
P2	0.7518
P3	0.2632
P4	147.3
P5	0.9200
P6	0.1003

p_{had}/p_{charm}
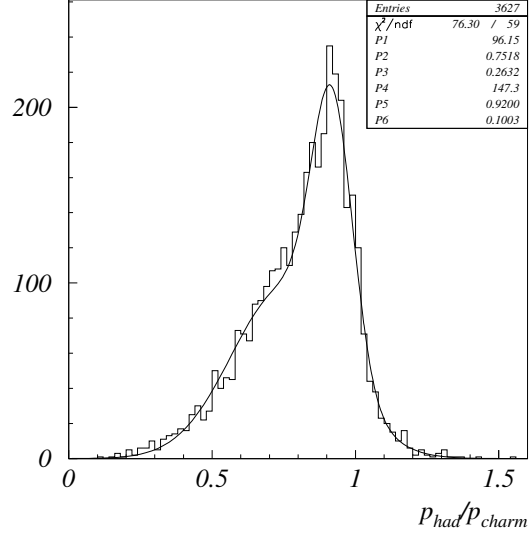
Figure 6.8: z distribution for baryon production in $\bar{\nu}_\mu$ interactions. A fifth order polynomial is used to parametrize it.

clustering algorithm. This provides a good description of the number of particles at the primary vertex and of the kinematic distribution of the prompt strange particle. A Θ_c^0 mass of 2.7 GeV/c^2 is assumed and its width is neglected.

Finally, Vegas is used to generate two and four prong Θ_c^0 decays with different lifetimes ($0.5c\tau_{D^0}$, $c\tau = 100\mu m$, $2c\tau_{D^0}$, $4c\tau_{D^0}$, $8c\tau_{D^0}$ $16c\tau_{D^0}$), neglecting the effect of the matrix element.

The generated decay modes are the following:

- $\Theta_c^0 \rightarrow pK^0\pi^-$,

- $\Theta_c^0 \rightarrow pK^0 l^- \bar{\nu}_l$,

126

Figure 6.9: Θ_c^0 production in $\bar{\nu}_\mu$ interactions.

- $\Theta_c^0 \rightarrow pK^+\pi^-\pi^-$.

For each decay mode 81k events were generated.

6.3 Decay Branching Ratios

The decay branching ratios of the Θ_c^0 were estimated in Ref. [127, 139]. Cabibbo suppressed amplitudes were neglected and the work focused on the decay channels with 2 and 4 charged prongs in the final state where one of them is always a proton.

The branching ratios were calculated by using Clebsh-Gordon coefficients from isospin conservation of the non-charmed quark cluster. The two and four prong decay branching ratio were found to be

$$br_{2p} = \frac{1}{3}, \tag{6.2}$$

$$br_{4p} = \frac{1}{30}. \tag{6.3}$$

6.4   Efficiency and Background Evaluation

In order to evaluate the location and detection efficiencies for the $\bar{\nu}_\mu$CC events with the Θ_c^0 in the final state, we have performed a fast MC simulation. We parametrized the track reconstruction efficiency in the electronic detector as a function of particle momentum using the reconstructed $\bar{\nu}_\mu$CC MC sample. The parametrization as a function of the particle momentum is given by

$$0.81806 - 0.35177 * exp(-0.76248 * P)$$

and shown in the Figure 6.10.
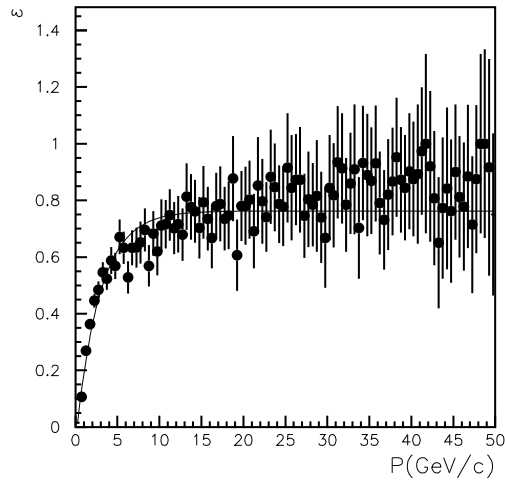
Figure 6.10: Parametrization as a function of particle momentum.

In order to have a realistic distribution of the interaction vertex in the emulsion

stack, MC truth vertex position is transferred to the CHORUS coordinates and shown in Figure 6.11. The stack number was fixed as 4. X position varied from 24.3275 $cm < x < 21.4835$ cm, Y and Z positions varied from -70 cm to 70 cm.
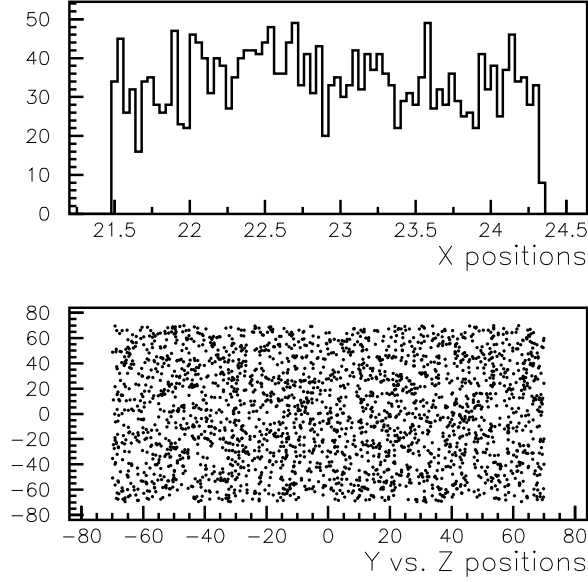
Figure 6.11: Vertex position in the emulsion target from MC simulation.

We assumed the same reconstruction efficiency for pentaquark, (Θ_c^0), production as $\bar{\nu}_\mu$CC events which is $(83.2 \pm 0.3)\%$. Using this parametrization, the ratio of reconstruction and location efficiency, Table 6.3, of events with the Θ_c^0 in the final state to that of all $\bar{\nu}_\mu$ CC events is found to be 0.88 ± 0.02 (0.86 ± 0.01 for $\bar{D}^0$ in the final state).

The selection efficiency for decay topologies of $\bar{D}^0$ are shown in Table 6.4. The Θ_c^0 selection efficiency for different lifetimes of the Θ_c^0 and for the N4 and N2

Table 6.3: The location efficiencies and the ratio of reconstruction and location efficiency of events with the Θ_c^0 in the final state to that of all $\bar{\nu}_\mu$ CC events both for N2 and N4 decay topologies.

	$\epsilon_{loc.}^{N4}$ (%)	$\frac{\epsilon_{loc.}^{N4}}{\epsilon^{\bar{\nu}_\mu CC}}$ (%)	$\epsilon_{loc.}^{N2}$ (%)	$\frac{\epsilon_{loc.}^{N2}}{\epsilon^{\bar{\nu}_\mu CC}}$ (%)
$0.5c\tau_{D^0}$	49.3 ± 0.9	90 ± 1.7	48.8 ± 0.9	89 ± 1.7
$100\mu m$	49.6 ± 0.9	90 ± 1.7	48.9 ± 0.9	89 ± 1.7
$2c\tau_{D^0}$	48.9 ± 0.9	89 ± 1.7	48.6 ± 0.9	89 ± 1.7
$4c\tau_{D^0}$	49.1 ± 0.6	89 ± 1.2	49.1 ± 0.6	89 ± 1.2
$8c\tau_{D^0}$	49.3 ± 0.6	90 ± 1.2	47.9 ± 0.9	87 ± 1.7
$16c\tau_{D^0}$	46.5 ± 0.6	85 ± 1.2	46.5 ± 0.6	85 ± 1.2

topologies are shown respectively in Table 6.6 and Table 6.5.

6.5   How to Estimate the Sensitivity and Limit

From the null result, we can set a limit on the production cross section, which relates to how often a particular process occurs. The production cross section can be thought of as a probability.

It can also be thought of as the effective area presented by the antineutrino nucleon interactions to a particular production mechanism. If you take this quantity and multiply it by a measurement of the amount of data that is collected and the efficiency for detecting the Θ_c^0 signal, you get an estimate for the number of the Θ_c^0 events in the given data set. And when we set a limit on the production cross section, in the absence of any detectable signal, we estimate a maximum possible value for this quantity.

Table 6.4: The selection efficiencies for decay topologies of $\bar{D}^0$ for the different $c\tau$ cuts.

$\bar{D}^0$	no cut(%)	$c\tau > 50$(%)	$c\tau > 100$(%)	$c\tau > 150$(%)	$c\tau > 200$(%)	$c\tau > 250$(%)
N2 ($\phi > 10$)	45.9±0.9	30.6±0.8	18.9±0.7	12.4±0.6	8.4±0.5	5.7±0.4
N4	79.2±1.5	52.8±1.8	31.7±1.7	19.3±1.4	11.1±1.1	7.5±0.9

Table 6.5: The selection efficiencies for the N2 decay topology of the Θ_c^0 for the different $c\tau$ cuts.

N2	no cut (%) $\phi >$10mrad	$c\tau > 50$(%) $\phi >$10mrad	$c\tau > 100$(%) $\phi >$10mrad	$c\tau > 150$(%) $\phi >$10mrad	$c\tau > 200$(%) $\phi >$10mrad	$c\tau > 250$(%) $\phi >$10mrad
$0.5c\tau_{D^0}$	31.8±1.2	14.9±0.9	6.3±0.6	2.8±0.4	1.4±0.3	0.6±0.2
$100\mu m$	33.9±1.2	19.6±1.0	11.7±0.8	7.3±0.7	4.8±0.6	2.9±0.4
$2c\tau_{D^0}$	35.6±1.3	28.3±1.2	20.9±1.1	16.1±1.0	13.1±0.9	9.8±0.8
$4c\tau_{D^0}$	25.5±0.7	21.6±0.7	17.5±0.6	14.4±0.6	11.6±0.5	9.4±0.5
$8c\tau_{D^0}$	26.6±0.8	23.9±0.8	21.0±0.7	18.2±0.7	15.5±0.7	12.9±0.6
$16c\tau_{D^0}$	20.2±0.7	18.9±0.7	17.0±0.7	15.1±0.7	13.5±0.6	11.9±0.6

Table 6.6: The selection efficiencies for the N4 decay topology of the Θ_c^0 for the different $c\tau$ cuts.

N4	no cut (%)	$c\tau > 50$(%)	$c\tau > 100$(%)	$c\tau > 150$(%)	$c\tau > 200$(%)	$c\tau > 250$(%)
$0.5c\tau_{D^0}$	60.6±1.3	24.6±1.1	7.7±0.7	2.7±0.4	1.5±0.3	0.8±0.2
$100\mu m$	61.5±1.3	31.8±1.2	17.5±0.9	9.9±0.8	5.7±0.7	3.4±0.5
$2c\tau_{D^0}$	54.6±1.3	39.2±1.3	28.5±1.2	21.3±1.1	15.7±0.9	11.4±0.8
$4c\tau_{D^0}$	43.9±0.9	35.9±0.9	27.9±0.8	22.3±0.8	17.6±0.7	14.0±0.6
$8c\tau_{D^0}$	31.3±0.9	27.0±0.8	23.4±0.8	19.5±0.7	16.3±0.7	14.4±0.6
$16c\tau_{D^0}$	19.8±0.7	17.7±0.7	15.6±0.7	14.2±0.6	12.3±0.6	10.8±0.6

6.6   Sensitivity and Backgrounds for Θ_c^0

The proton identification efficiency is very low in the case of the CHORUS experiment due to momentum distributions of the daughter particles as discussed in Sec. 6.1.2. Instead of evaluating the limit based on the proton identification, the limits for different possible lifetime of the Θ_c^0 ($0.5c\tau_{D^0}$, $c\tau = 100\mu m$, $2c\tau_{D^0}$, $4c\tau_{D^0}$, $8c\tau_{D^0}$ $16c\tau_{D^0}$) have been computed. The proper lifetime for a given Θ_c^0 decay is

$$\tau = \frac{\ell m_{\Theta_c^0}}{cP_{\Theta_c^0}}$$

where $m_{\Theta_c^0}$ and $P_{\Theta_c^0}$ and ℓ are the mass and momentum and flight length of the Θ_c^0, respectively. The momentum of the Θ_c^0 is not directly measured in emulsion. Instead, one can exploit the correlation between the momentum and the angular distribution of the decay products [140]. These angles are measured very precisely. For a given decay mode this correlation is determined by the decay kinematics and is model independent. The most sensitive parameter is the geometrical average of the angle of the decay daughters with respect to the direction of the Θ_c^0, $\langle\theta\rangle$, which is inversely proportional to the momentum of the parent, $P_{\Theta_c^0}$. Hence, the lifetime of the Θ_c^0 can be estimated as;

$$c\tau = \frac{Flight\ length}{\gamma_{est}},$$

where $\gamma_{est} = \frac{1}{\langle\theta\rangle}$, and $\langle\theta\rangle = \frac{\sum(\theta_{daughter} - \theta_{parent})}{N}$.

The proper lifetime of the neutral decay candidates were estimated as shown in the Figure 6.12.

In order to minimize the production sensitivity, a cut on the measured lifetime is

133

Figure 6.12: Estimated $c\tau$ versus flight length distribution of $\bar{D}^0$.

applied. The sensitivity is expressed as

$$S = \frac{N_{limit}}{N_{loc} \times \epsilon_{loc} \times \epsilon_{\Theta_c^0} \times Br(N2 + N4)} \tag{6.4}$$

where N_{limit} is the number of signal Θ_c^0 event, including estimated uncertainties at 90% CL [141]. $\epsilon_{\Theta_c^0}$ represents the efficiency for detecting decay topology, ϵ_{loc} stands for location efficiency relative to $\bar{\nu}_\mu$ event for the Θ_c^0 events.

As mentioned in Sec. 5.3.1, the background for neutral charmed decays were estimated as 2.76 ± 0.64 events in N2, while 0.29 ± 0.02 events in N4 candidates in the present sample of μ^+. Majority of background is due to strange particle decays into two bodies. Further reduction of background can be achieved in N2 decay topologies by acoplanarity angle selection, $\phi > 10mrad$. By applying this selection,the background event number is reduced to 0.66 ± 0.32 in N2 sample.

So all neutral candidates were treated as $\bar{D}^0$ here. Number of expected $\bar{D}^0$ events is given in Table 6.7. $\bar{D}^0$ production rate in antineutrino interactions was estimated in

Sec. 5.4 as

$$\frac{\sigma(\bar{\nu}_\mu N \to \mu^+ \bar{D}^0 X)}{\sigma(\bar{\nu}_\mu N \to \mu^+ X)} = (2.86^{+0.71}_{-0.59}(\text{stat}) \pm 0.14(\text{syst}))\%. \qquad (6.5)$$

Table 6.7: The number of events for each decay topology of $\bar{D}^0$ for the different $c\tau$ cuts.

$c\tau$ cut	non cut	$c\tau$ >50	$c\tau$ >100	$c\tau$ >150	$c\tau$ >200	$c\tau$ >250
N2	19	15	11	8	5	4
N2 ($\phi > 10 mrad$)	15	11	9	7	4	3
N4	9	7	4	1	1	0
N2+N4	24	18	13	8	5	3

The number of corrected $\bar{D}^0$ is given by

$$N_{\bar{D}^0} = N_{loc}^{\bar{\nu}_\mu CC} * \sigma(\bar{D}^0) * \epsilon_{\bar{D}^0} * (1 - BR(D^0 \to All\ neutral))$$

and found to be 42.3 (35.1 N2 + 7.2 N4). The number of $\bar{D}^0$ events for different lifetime is given in Table 6.8 and Table 6.9. The uncertainty in background estimation is $\frac{\delta(N_{\bar{D}^0})}{N_{\bar{D}^0}} = 0.3$. The sensitivity which is given in that tables is averaged limit by infinite times tests with null signal.

Table 6.8: $\bar{D}^0$ background estimations for the different $c\tau$ cuts. The uncertainty in background estimation is $\frac{\delta(N_{\bar{D}^0})}{N_{\bar{D}^0}} = 0.3$.

$c\tau$ cut	non cut	>50	>100	>150	>200	>250
N2(ϕ >0.01)	16.11	10.74	6.63	4.35	2.95	2.00
N4	5.70	3.80	2.28	1.39	0.80	0.54
N2+N4	21.81	14.54	8.91	5.74	3.75	2.54
30% error	6.54	4.36	2.67	1.72	1.13	0.76
Sensitivity(N_{limit}) 30%	14.54	10.89	7.97	6.20	5.12	4.31

Table 6.9: $\bar{D}^0$ background estimations for the different $c\tau$ cuts. The uncertainty in background estimation is $\frac{\delta(N_{\bar{D}^0})}{N_{\bar{D}^0}} = 0.3$.

$c\tau$ cut	non cut	<50	<100	<150	<200	<250
N2(ϕ >0.01)	16.11	5.37	9.48	11.76	13.16	14.11
N4	5.70	1.90	3.42	4.31	4.90	5.16
N2+N4	21.81	7.27	12.90	16.07	18.06	19.27
30% error	6.54	2.18	3.87	4.82	5.41	5.78
Sensitivity(N_{limit}) 30%	14.54	7.09	10.03	11.67	12.67	13.29

Table 6.10 contains the number of efficiency corrected events, $N_{test} = N_{loc}^{\bar{\nu}_\mu CC} * \epsilon_{\Theta_c^0} *$

$(\epsilon_{N2}^{\Theta_c^0} * br_{2p} + \epsilon_{N4}^{\Theta_c^0} * br_{4p})$, where the branching ratios $br_{2p} = \frac{1}{3}$ and $br_{4p} = \frac{1}{30}$ (Sec. 6.3).

Table 6.10: Number of efficiency corrected and analyzed events.

$c\tau$ cut	non cut	>50	>100	>150	>200	>250
$0.5c\tau_{D^0}$	246.26	130.49	196.00	221.46	231.13	236.53
$c\tau = 100\mu m$	260.28	145.01	85.62	52.77	34.18	20.62
$2c\tau_{D^0}$	266.11	205.10	151.18	116.04	93.38	69.64
$4c\tau_{D^0}$	194.08	160.35	129.16	105.86	85.04	68.75
$8c\tau_{D^0}$	191.97	169.32	148.57	128.27	109.04	91.28
$16c\tau_{D^0}$	142.91	131.58	118.14	105.16	93.76	82.63

Using the numbers given in Tables 6.10, 6.8, 6.9, limits on the Θ_c^0 production are

estimated and given in Table 6.13. Since the decay branching ratios of the Θ_c^0 are model

dependent, the sensitivity as a function of br_{2p} is estimated and shown in Figure 6.13.

In the range of the Θ_c^0 proper lifetimes (0.5 to $16\tau_{D^0}$), the upper limit of the produc-

tion ratio is found to be less than 0.085 at 90% C.L.. The tightest bound $\sigma_{\Theta_c^0}/\sigma_{\bar{\nu}} <0.039$

at 90% C.L is obtained for Θ_c^0 lifetime to be equal to $0.5c\tau_{D^0}$.

Table 6.11: Cross section limit sensitivity.

ct cut	non cut	>50	>100	>150	>200	>250
$0.5c\tau_{D^0}$	0.0590	0.0543	0.0512	0.0527	0.0548	0.0562
$c\tau = 100\mu m$	0.0559	0.0751	0.0931	0.1175	0.1498	0.2090
$2c\tau_{D^0}$	0.0546	0.0531	0.0527	0.0534	0.0548	0.0619
$4c\tau_{D^0}$	0.0749	0.0679	0.0617	0.0586	0.0602	0.0627
$8c\tau_{D^0}$	0.0757	0.0643	0.0536	0.0483	0.0470	0.0472
$16c\tau_{D^0}$	0.1017	0.0828	0.0675	0.0590	0.0546	0.0522

Table 6.12: The sensitivity of the Θ_c^0 production for different lifetime of the Θ_c^0. The lifetime cut is applied in order to minimize the production sensitivity. The uncertainty in background estimation is $\frac{\delta(N_{\bar{D}^0})}{N_{\bar{D}^0}} = 0.3$. As branching ratios Br(N2)=0.33 and Br(N4)=0.033 are used.

	$c\tau$ cut	D^0 (N2+N4)	sensitivity
$0.5c\tau_{D^0}$	$< 100\mu m$	9.48+3.42	0.051
$c\tau = 100\mu m$	no cut	16.11+5.70	0.056
$2c\tau_{D^0}$	$> 100\mu m$	6.63+2.28	0.053
$4c\tau_{D^0}$	$> 150\mu m$	4.35+1.39	0.059
$8c\tau_{D^0}$	$> 200\mu m$	2.95+0.80	0.047
$16c\tau_{D^0}$	$> 250\mu m$	2.00+0.54	0.052

Table 6.13: The limit of the Θ_c^o production is estimated for different lifetime of the Θ_c^o. The lifetime cut is applied in order to minimize the production sensitivity. The uncertainty in background estimation is $\frac{\delta(N_{\bar{D}^0})}{N_{\bar{D}^0}} = 0.3$. As branching ratios Br(N2)=0.33 and Br(N4)=0.033 are used.

	$c\tau$ cut	data (N2+N4)	Limit
$0.5c\tau_{D^0}$	$< 100\mu m$	6+5	0.039
$c\tau = 100\mu m$	no cut	15+9	0.065
$2c\tau_{D^0}$	$> 100\mu m$	9.4	0.084
$4c\tau_{D^0}$	$> 150\mu m$	7+1	0.083
$8c\tau_{D^0}$	$> 200\mu m$	4+1	0.062
$16c\tau_{D^0}$	$> 250\mu m$	3+0	0.052
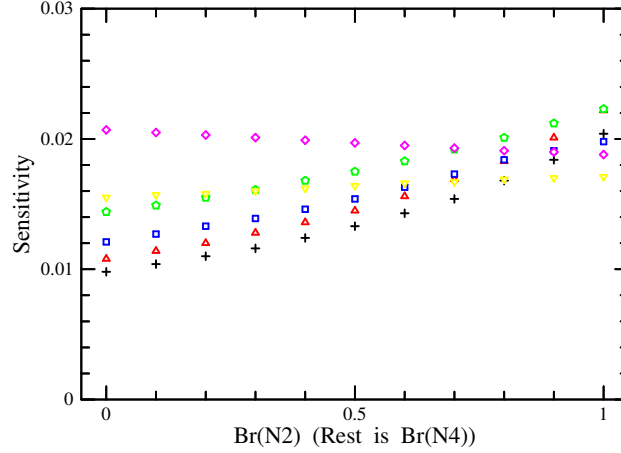
Figure 6.13: Θ^0_c production cross section sensitivity as a function of the br_{2p} (in the assumption that $br_{2p} + br_{4p} = 1$) for different proper lifetimes of Θ^0_c. Black points: $0.5c\tau_{D^0}$, Red: 100 μ, Blue: $2c\tau_{D^0}$, Green: $4c\tau_{D^0}$, Yellow: $8c\tau_{D^0}$ and Purple: $16c\tau_{D^0}$.

6.7   Future Prospect of Pentaquark Search at a Neutrino Factory

In this thesis, a strategy to search for charmed pentaquarks in antineutrino interactions is presented. This strategy is also applied to the possible search for the charmed pentaquark using an Emulsion Cloud Chamber (ECC) as used in the OPERA detector [142], at a neutrino factory [127].

It is assumed that the target section of the detector is made of lead plates and nuclear emulsions used as tracking devices. The cross section of the target is assumed to be 1 m^2 (a wall with a matrix of 8×10 OPERA-like bricks). The whole target is made of 20 walls for a total mass of about 13 *tons* and located 1 km far from the neutrino source. We assume 2 year data taking ($T = 400$ days) and a $\bar{\nu}_\mu$ flux on the

138

detector $\Phi = 10^7 (\nu/s)$ which corresponds to about 3.5×10^{14} decaying muons.

By using a 13 *ton* detector, with a conservative approach, an upper limit of 1.0×10^{-4} of the production ratio is achievable in case of a null result. This value is less than 1% of the $\bar{D}^0$ production cross section in $\bar{\nu}_\mu$ interactions.

CHAPTER 7

CONCLUSIONS

The CHORUS experiment was designed to search for $\nu_\mu \to \nu_\tau$ oscillations through ν_τ appearance in the ν_μ beam. Apart from the neutrino oscillation search, CHORUS has studied numerous subjects related to the charm quark production in neutrino-induced charged current interactions and their decays as well as associated charm production both in charged current and neutral current neutrino interactions. This thesis concerns antineutrino-induced charm and pentaquark productions by using the presence of a 6% $\bar{\nu}_\mu$ component in the beam with 18 GeV average energy.

The analysis is based on a sample of 3390 events with at least one reconstructed positive muon in the spectrometer. Selection criteria to improve the reliability of the muon reconstruction have been applied and 2480 events survived. Decay search has been applied to the sample of 2480 events. 46 $\bar{\nu}_\mu$ induced charm events were observed with an estimated background of 5.2 ± 0.4 events. At an average antineutrino energy of 18 GeV in the neutrino beam, the charm production rate induced by antineutrinos

is measured to be

$$\frac{\sigma(\bar{\nu}N \to \mu^+ \bar{c}X)}{\sigma(\bar{\nu}N \to \mu^+ X)} = (4.55^{+0.96}_{-0.81}(\text{stat}) \pm 0.64(\text{syst}))\%.$$

$\bar{D}^0$ and charged charm (D^-, D_s^-) production rate are measured to be

$$\frac{\sigma(\bar{\nu}_\mu N \to \mu^+ \bar{D}^0 X)}{\sigma(\bar{\nu}_\mu N \to \mu^+ X)} = (2.86^{+0.71}_{-0.59}(\text{stat}) \pm 0.14(\text{syst}))\%,$$

$$\frac{\sigma(\bar{\nu}_\mu N \to \mu^+ (D^-, D_s^-)X)}{\sigma(\bar{\nu}_\mu N \to \mu^+ X)} = (1.69^{+0.62}_{-0.52}(\text{stat}) \pm 0.24(\text{syst}))\%.$$

The ratio between neutral and charged charm production rates is found to be

$$1.69^{+0.75}_{-0.63}(stat) \pm 0.21(syst).$$

This result is consistent with the previous measurements [81].

By using the $\bar{\nu}_\mu$ data sample, anticharmed pentaquark (Θ_c^0) has been searched for and no evidence is found. Based on the null observation, the limit of the Θ_c^0 production is found as a function of different possible Θ_c^0 lifetimes ($0.5c\tau_{D^0}$, to $16c\tau_{D^0}$). The upper limit of the production ratio $\sigma_{\Theta_c^0}/\sigma_{\bar{\nu}}$ is less than 0.085 at 90% C.L.. The tightest bound is $\sigma_{\Theta_c^0}/\sigma_{\bar{\nu}} <$0.039 at 90% C.L. obtained for Θ_c^0 lifetime taken equal to $0.5c\tau_{D^0}$. The upper bound is above the $\bar{D}^0$ production in antineutrinos and therefore does not provide a tight bound to the Θ_c^0 production. This is mainly due to the limited statistics of the $\bar{\nu}_\mu$ sample.

REFERENCES

[1] S. L. Glashow, Nucl. Phys. **22**, 579 (1961).

[2] A. Salam, Phys. Lett. **13**, 168 (1964).

[3] S. Weinberg, Phys. Rev. Lett. **19**, 1264 (1967).

[4] L. B. Okun, **Lepton and Quarks**, North-Holland, Amsterdam (1982).

[5] CHORUS Collaboration, to be submitted to Nucl. Phys. **B**.

[6] S. Eidelman *et al.*, Review of Particle Physics (PDG), Phys. Lett. **B592**, 1 (2004).

[7] W. Seligman, Ph.D. Thesis, Nevis Report, 292 (1996).

[8] P.S. Auchincloss *et al.*, Z. Phys. **C48**, 411 (1990).

[9] D.B. MacFarlane *et al.*, Z. Phys. **C26**, 1 (1984).

[10] P. Berge *et al.*, Z. Phys. **C35**, 443 (1987).

[11] N. Cabibbo, Phys. Rev. Lett. **10**, 531 (1963).

[12] M. Kobayashi and T. Maskawa, Prog. Theor. Phys. **49**, 652 (1973).

[13] L. Maiani, Cambridge Monogr. Part. Phys. Nucl. Phys. Cosmol. **1**, 278 (1991).

[14] R. M. Barnett, Phys. Rev. Lett. **36**, 1163 (1976).

[15] R. M. Barnett, Phys. Rev. **D14**, 70 (1976).

[16] B. Andersson, G. Gustafson and B. Soderberg, Z. Phys. **C20**, 317 (1983).

[17] C. Peterson, D. Schlatter, L. Schmitt and P. M. Zerwas, Phys. Rev. **D27**, 105 (1983).

[18] M. Aguilar-Benitez *et al.*, Phys. Lett. **B135**, 237 (1984).

[19] T.N. Yang and R.L. Mills, Phys. Rev. **96**, 191 (1954).

[20] R. L. Jaffe, Phys. Rev. Lett. **38**, 195 (1977).

[21] Particle Data Group, Phys. Lett. **B592**, 848 (2004).

[22] E. Golowich, Phys. Rev. **D4**, 262 (1971).

[23] G. P. Yost *et al*, Particle Data Group, Phys. Lett. **B204**, 1 (1988).

[24] D. Diakonov, V. Petrov, and M. Polyakov, Z. Phys. **A359**, 305 (1997).

[25] R.L. Jaffe, F. Wilczek, Phys. Rev. Lett. **91**, 232003 (2003).

[26] R.L. Jaffe, F. Wilczek, hep-ph/0409065.

[27] B. Wu and B.Q. Ma, hep-ph/0402244.

[28] K. Cheung, hep-ph/0308176.

[29] M. Karliner, H.J. Lipkin, hep-ph/0307243.

[30] S. Sasaki, hep-lat/0310014.

[31] T. W. Chiu and T. H. Hsieh, hep-ph/0404007.

[32] T. H. R. Skyrme, Nucl. Phys. **31**, 556 (1962).

[33] J. K. Perring and T. H. R. Skyrme, Nucl. Phys. **31**, 550 (1962).

[34] E. Witten, Nucl. Phys. **B223**, 433 (1983).

[35] E. Eskut *et al.*, CHORUS Collaboration, Nucl. Instrum. and Meth. **A401**, 7 (1997).

[36] G. Acquistapace *et al.* The West Area Netrino Facility for CHORUS and NOMAD experiments:1994-1997 operation. CERN-ECP-95-014.

[37] B. Van de Vyver and P. Zucchelli, Nucl. Instrum. and Meth. **A385**, 91 (1997).

[38] S. Sorrentino, CHORUS internal note 980056 (1998).

[39] A. Kayis-Topaksu *et al.*, CHORUS Collaboration, Eur. Phys. J. **C30**, 159 (2003).

[40] K. Niwa, Contrib. to the "Snowmass '94" Conference on Particle and Nuclear Astrophysics and Cosmology in the next Millennium, Snowmass (1994).

[41] P. Ledermann *et al.*, Nucl. Instrum. and Meth. **A344**, 143 (1994).

[42] P. Annis *et al.*, Nucl. Instrum. and Meth. **A367**, 367 (1995).

[43] P. Annis *et al.*, Nucl. Instrum. and Meth. **A412**, 19 (1998).

[44] D. Acosta *et al.*, Nucl. Instrum. and Meth. **A308**, 481 (1991).

[45] F. Bergsma *et al.*, Nucl. Instrum. and Meth. **A357**, 243 (1995).

[46] S. Buontempo *et al.*, Nucl. Instrum. and Meth. **A349** (1994).

[47] E. Di Capua *et al.*, Nucl. Instrum. and Meth. **A378**, 221 (1996).

[48] M. G. van Beuzekom *et al.*, Nucl. Instrum. and Meth. **A427**, 587 (1999).

[49] S. Aoki *et al.*, Nucl. Instrum. and Meth. **B51**, 446 (1990).

[50] T. Nakano, Ph.D. Thesis, Nagoya University (1997).

[51] E. Eskut *et al*, CHORUS Collaboration, Phys. Lett. **B497**, 8 (2001).

[52] A. M. Guler, J. Phys. Conf. Ser. bf 39, 313 (2006).

[53] A. Kayis-Topaksu *et al.*, CHORUS Collaboration, Phys. Lett. **B527**, 173 (2002).

[54] G. Onengut *et al.*, CHORUS Collaboration, Phys. Lett. **B613**, 105 (2005).

[55] Particle Data Group, Phys. Rev. **D66**, 010001 (2002).

[56] G. Onengut *et al.*, CHORUS Collaboration, Phys. Lett. **B614**, 155 (2005).

[57] A. Kayis-Topaksu *et al.*, CHORUS Collaboration, Phys. Lett. **B555**, 156 (2003).

[58] A. Kayis-Topaksu *et al.*, CHORUS Collaboration, Phys. Lett. **B575**, 198 (2003).

[59] G. Onengut *et al.*, CHORUS Collaboration, Phys. Lett. **B604**, 145 (2004).

[60] A. Kayis-Topaksu *et al.*, CHORUS Collaboration, Phys. Lett. **B539**, 188 (2002).

[61] CHORUS Collaboration, to be submitted to Phys. Lett. **B**.

[62] J. Brunner, CHORUS offline manual (1998).

[63] A. Artamonov, J. Brunner and R. Tzenov, CHANT manual, CHORUS internal note.

[64] M.Komatsu, Y. Kotaka, Unpublished Note.

[65] K. Kodama *et al.*, DONUT Collaboration, Phys. Lett., **B504**, 218 (2001).

[66] N. Nonaka, Ph.D. Thesis, Nagoya University (2002).

[67] A. M. Guler, Ph.D. Thesis, Middle East Technical University (2000).

[68] S. Aoki, Nagoya University internal note.

[69] K. Komatsu, Nagoya University internal note.

[70] G. Derosa, Unpublished note and private communication.

[71] A. M. Guler, CHORUS Collaboration Meeting, http://choruswww.cern.ch/Internals/Collab-Meetings/200302-WS/agenda.html.

[72] J. Kawada, Ph.D. Thesis, Nagoya University (2006).

[73] H. Abramowicz *et al.*, CDHS Collaboration, Z. Phys. **C15**, 19 (1982).

[74] S.A. Rabinowitz *et al.*, CCFR Collaboration, Phys. Rev. Lett. **70**, 134 (1993).

[75] M. Jonker *et al.*, CHARM Collaboration, Phys. Lett. **B107**, 241 (1981).

[76] P. Vilain *et al.*, CHARM II Collaboration, Eur. Phys. J. **C11**, 19 (1999).

[77] P. Astier *et al.*, NOMAD Collaboration, Phys. Lett. **B486**, 35 (2000).

[78] M. Goncharov *et al.*, NuTeV Collaboration, Phys. Rev. **D64**, 112006 (2001).

[79] N. Ushida, *et al.*, E531 Collaboration, Phys. Lett. **B206**, 375 (1988).

[80] N. Ushida, *et al.*, E531 Collaboration, Phys. Lett. **B121**, 287 (1983).

[81] G. Onengut *et al.*, CHORUS Collaboration, Phys. Lett. **B604**, 11 (2004).

[82] A. Fasso, A. Ferrari, P. R. Sala, *Electron-photon transport in FLUKA: Status* invited talk in the Proceeding of the MonteCarlo 2000 Conference, Lisbon, October 23-26 2000.

[83] I. I. Tsukerman, CHORUS internal note 2000010 (2001).

[84] GEANT 3.21. CERN program library long write up W5013.

[85] P. Zuchelli, Ph.D. Thesis, Universita di Ferrara (1995).

[86] G. Ingelman, Preprint TSL/ISV-92-0065, Uppsala University (1992).

[87] T. Sjostrand, Comput. Phys. Commun. **82**, 74 (1990).

[88] S. Ricciardi, Ph.D. Thesis, Universita di Ferrara (1996).

[89] A. M. Guler, O. Sato, CHORUS Internal note 2000017 (2002).

[90] G. De Lellis *et al.*, Phys. Lett. **B550**, 16 (2002).

[91] A. Satta, Ph.D. Thesis, Universita La Sapienza di Roma (2001).

[92] A. Fasso, A. Ferrari, P. R. Sala, *Proc. 3rd Workshop on Simulating Accelerator Ratiation Environments (SARE 3)*, Ed. H. Hirayama (1997).

[93] G.J. Feldman and R.D. Cousins, Phys. Rev. **D57**, 3873 (1998).

[94] Nakano T. *et al.*, Phys. Rev. Lett. **91**, 012002 (2003).

[95] Stepanyan S. *et al.*, CLAS Collaboration, Phys. Rev. Lett. **91**, 252001-1 (2003).

[96] Kubarovsky V. *et al.*, CLAS Collaboration, Phys. Rev. Lett. **92**, 032001-1 (2004).

[97] Barth J. *et al.*, SAPHIR Collaboration, Phys. Lett. **B572**, 127 (2003).

[98] Abdel-Bary M. *et al.*, COSY Collaboration, Phys. Lett. **B595**, 127 (2004).

[99] Aslanyan P., Emelyanenko V. and Rikhkvitzkaya, hep-ex/0403044.

[100] Aleev A. *et al.*, SVD Collaboration, hep-ex/0401024.

[101] Barmin V. *et al.*, Phys. Atom. Nucl. **66**, 1715 (2003).

[102] Asratyan A., Dolgolenko A. and Kubantsev A., Phys. Atom. Nucl. **67**, 682 (2004).

[103] Camilleri L., Presented at the *Neutrinos 2004 Paris*, `neutrino2004.in2p3.fr`.

[104] Airapetian A. *et al.*, Hermes Collaboration, Phys. Lett. **B585**, 213 (2004).

[105] Chekanov S. *et al.*, ZEUS Collaboration, Phys. Lett. **B591**, 7 (2004).

[106] Alt C. *et al.*, NA49 Collaboration, Phys. Rev. Lett. bf 92, 042003-1 (2004).

[107] Aktas, A. *et al.*, H1 Collaboration, Phys. Lett. **B588**, 17 (2004).

[108] Schael S. *et al.*, ALEPH Collaboration, Phys. Lett. **B599**, 1 (2004).

[109] Aubert B. *et al.*, BaBar Collaboration, hep-ex/0408064.

[110] Mizuk R., BELLE Collaboration, hep-ex/0411005.

[111] Bai J. *et al.*, BES Collaboration, Phys. Rev. **D70**, 012004 (2004).

[112] Wang M-J. *et al.*, CDF Collaboration, hep-ex/0408025 and hep-ex/0410024.

[113] Brona G. and Badelek B., COMPASS Collaboration, `wwwcompass.cern.ch/compass/notes/2004-5`

[114] Stenson, K., FOCUS Collaboration, hep-ex/0412021.

[115] Abt I. *et al.*, HERA-B Collaboration, Phys. Rev. Lett. **93**, 212003 (2004); Knoepfle, K *et al.*, HERA-B Collaboration, J. Phys. **G30**, S1363 (2004).

[116] Longo M. *et al.*, HyperCP Collaboration, hep-ex/0410027.

[117] Armstrong S, hep-ex/0410080.

[118] Pinkenburg C., PHENIX Collaboration, J. Phys. **G30**, S1201 (2004).

[119] Antipov Yu *et al.*, SPHINX Collaboration, Eur. Phys. J. **A21**, 455 (2004).

[120] Salur S., STAR Collaboration, hep-ex/0403009 and nucl-ex/0410039

[121] Adamovich M. *et al.*, WA89 Colaboration, hep-ex/0405042.

[122] M. Battaglieri *et al.*, CLASS Colaboration, Phys. Rev. Lett. **96**, 042001 (2006).

[123] Chekanov S. *et al.*, ZEUS Collaboration, Eur.Phys.J. **C38**, 29 (2004).

[124] C. Gignoux, B. Silvestre-Brac, J.M. Richard, Phys. Lett. **B193**, 323 (1987). H.J. Lipkin, Phys. Lett. **B195**, 484 (1987)

[125] D.O. Riska, N.N. Scoccola, Phys. Lett. **B299**, 338 (1993).

[126] M. A. Nowak *at el.*, Phys. Rev. **D70**, 031503 (2004).

[127] G. de Lellis *et al.*, Accepted for publication in Nucl. Phys. **B**.

[128] K. Abe *et al.*, SLAC Hybrid Facility Photon Collaboration, Phys. Rev **D33**, 1 (1986); SLAC-PUB-3493 (1984).

[129] S. M. Errede, Ph.D. Thesis, Ohio State University, USA (1981)
H. Shibuya, Ph.D. Thesis, Nagoya University, Japan (1982).

[130] C.F. Powell, P.H. Fowler, D.H. Perkins, **The Study of Elementary particles by the Photographic Method**, Pergamon Press, Oxford (1959); W.H. Barkas, **Nuclear Research Emulsions**, Academic Press, New York (1963).

[131] T. Toshito et al., Nucl. Instrum. Method. **A516**, 436 (2004).

[132] G. De Lellis et al., Nucl. Instrum. Meth. **A512**, 539 (2003).

[133] S. Aoki et al., Nucl. Instrum. Meth. **A447**, 361 (2000).

[134] G. P. Lepage, J. Comput. Phys. **27**, 192 (1978).

[135] C. Peterson, D. Schlatter, I. Schmitt and P.M. Zerwas, Phys. Rev. **D 27**, 105 (1983).

[136] P.D.B. Collins and T.P. Spiller, J. Phys. **G 11**, 1289 (1985).

[137] G. De Lellis, P. Migliozzi and P. Santorelli, Phys. Rept. **399**, 227 (2004).

[138] G. Corcella *et al.*, JHEP **0101**, 010 (2001).
G. Corcella *et al.*, hep-ph/0210213.

[139] F. Bucella, D. Falcone and F. Tramontano, Central Eur. J. Phys. **3**, 525 (2005).

[140] S. Petrera, G. Romano, Nucl. Instrum. Meth. **174**, 61 (1980).

[141] J.Conrad et al., Phys. Rev. **D67**, 012002 (2003).

[142] D. Autiero for the OPERA Collaboration, Nucl. Phys. Proc. Suppl. **143**, 257 (2005).

CHAPTER 9

APPENDIX

9.1   List of Charm Candidates:

The list of 46 charm events is reported. The header has the following information:
iev topology dvtx pvtx nshower nblack thetay thetaz pmuon fl where it iev is the run-event number, *top* is the decay topolog (*1 = kink, 2 = Vee, 3 = trident, 4 = 4Vee*), *dvtx* is the decay vertex plate number, *pvtx* is the primary vertex plate number, *nshower* and *nblack* are the number of shower and black track at primary vertex respectively, *thetay* and *thetaz* are the slope angle of the muon (*mrad*), *pmuon* is the muon momentum and *fl* is the flight length(*μm*).

```
49961084 3 11 14  5  0  0.0067  0.0861  55.19 1665.0

51622934 2 31 33  4  0 -0.0240  0.1066  53.17 1267.9

51912532 1 12 13  6  1 -0.0281  0.0263 104.08  996.0

53540459 4 29 33  4  8 -0.0196  0.0648  73.59 3236.1

53654692 1 28 28  3 14  0.0062 -0.0491  18.75  505.5

53820241 4 10 11  1  2 -0.0255 -0.1090   8.83 1097.0
```

```
55021038 4 23 23  2  0 -0.0285 -0.0763  15.60  344.5

56284150 4 18 20  4  0 -0.1036  0.1668   5.94 1044.5

56763284 1 22 30  4  5  0.0447 -0.0443  13.44 5760.3

57660312 1 20 23  8  9  0.0520 -0.0235  20.11 2384.3

58050782 1 13 17  8  2 -0.1377  0.2703   6.41 3797.6

58431625 2 14 15  2  5  0.0850  0.0466  19.94  852.2

59130634 3  4  9  6 13 -0.0606  0.0160  17.40 3568.4

59433622 2 19 19  1  6  0.0151  0.0236  33.12  193.9

61161353 2 17 18  3  1 -0.0176 -0.0062   3.62  739.6

61830657 1 28 30  3  1 -0.1118  0.0648  15.89 1223.6

62433293 1  6  6  4  5  0.1519  0.0527   4.37  208.3

63271369 3 20 21  8  5  0.0365  0.0814  23.88  332.9

66111892 2  8  7  8 10 -0.0145 -0.0060  50.59  554.0

66322446 2 20 23  7  2 -0.0947  0.0080  15.17 2744.4

69082757 4 10 11  3  0  0.0076 -0.0005  40.68  866.0

70282165 2 14 15  4  1 -0.0546  0.1545  13.79  520.0

72922167 4 10 11  6  1  0.0708  0.1171  30.20  617.0

73180682 2 32 33  3  6  0.0882  0.0056  10.40  709.7

73862499 1 30 31  5  2 -0.0611 -0.0460  25.53  665.7

74301849 2  6  6  4  1 -0.0374  0.0939  28.60  573.4

74901210 1  8 13  9  3  0.0593  0.0091  18.82 3976.6

75373730 1 19 20  4  7 -0.0197  0.0230 151.93  987.9
```

```
75932518 1 26 28  6  2  0.0604  0.0397  43.75 1952.0

75978738 2 34 34  4  3 -0.0050  0.0429  97.13  426.7

76141510 1 14 14  5  1 -0.0457  0.0428  44.63  194.9

76521111 2 23 27  4  0  0.0688 -0.0721   5.71 3227.3

76819034 2 10 16  3  4 -0.0010  0.0429 102.82 5137.4

77582068 2  3  6  2  5  0.0059  0.0984   9.16 2313.0

77787202 4 13 14  4  4  0.1253  0.0960   4.89  679.2

78617938 3 14 14  3  0  0.0674  0.0883   6.99  469.0

79180027 4 13 13  4  8  0.0337  0.0464  34.84  358.3

79222654 1 16 21  5  2 -0.0322  0.0376 142.80 3611.6

79242473 2 25 27  4  1  0.0268  0.0158  37.73  993.5

79262017 2 11 12 15 11  0.0294  0.0590  28.07  600.3

79741708 2 27 27  3  0  0.0227  0.0199  13.03  366.2

79769884 2 14 17  2  9 -0.0040  0.1672   8.52 2199.4

79914818 1 32 33  4  0 -0.0762  0.0645   7.48  710.2

80086811 2 25 27  4  2 -0.0791  0.0596  14.31 1662.6

81018164 4 11 11  3  4  0.0033  0.0564 259.88  105.4

81400638 2 25 28  1  3 -0.0128  0.0581  31.05 2570.7
```

VITA

Umut Köse was born in Samandağ, Hatay, on 09 November 1974. After completing his studies at Antakya Merkez Lisesi, he went on to the University of Mersin at İçel where he studied physics and received his Bachelor of Science in 1998. In 1999 he entered The Graduate School at Middle East Technical University at Ankara and get his M.S. degree in 2002.

International Scholarships:

1. CERN Summer Studentship (Switzerland), 2001,

2. Visiting researcher, Nagoya University (Japan), February-March 2001,

3. Visiting researcher, Nagoya University (Japan), February-March 2002,

4. Visiting researcher, Napoli University (Italy), June 2002,

5. Visiting researcher, Nagoya University (Japan), March-September 2003,

6. Visiting researcher, Nagoya University (Japan), July-October 2004,

7. Visiting researcher, Nagoya University (Japan), February 2005-February 2006,

8. Visiting researcher, LNGS Laboratory (Italy), August-September 2006,

Conferences and Workshops:

1. II. International Workshop on Nuclear Emulsion Techniques, 7-9 March 2002, Nagoya University, Nagoya, Japan.

2. NUINT'02, Second International Workshop on Neutrino-Nucleus Interactions in the few-GeV Region, 12-15 December 2002, University of California, Irvine, USA, "*Multiplicity Measurement of Nuclear Fragments in Neutrino Interactions with CHORUS*", U. Kose.

3. Summer school on "Neutrino Physics and Astrophysics", 16-27 July 2002, Feza Gursey Institute, Istanbul, Turkey. Talk in Student seminar: "*Neutrino Nucleon Interactions in CHORUS Experiment*", U. Köse.

4. VII. Ulusal Nukleer Bilimler ve Teknolojileri Kongresi, 15-17 October 2003, Erciyes University, Kayseri, Turkey, "*Multiplicity Measurement in High Energy Neutrino Emulsion Interaction in CHORUS Experiment*", U. Köse.

5. Yüksek Enerji Fiziği Çalıştayı, 23-25 June 2004, Abant Izzet Baysal University, Bolu, Turkey.

6. CERN Openday, 16 November 2004, CERN, Switzerland, Poster: "Turkey at CERN 'CHORUS' ", E. Arik *et al.*

7. Exotic Hadron Workshop, 27 May 2005, Nara Women's University, Nara, Japan, "*Search for Exotics by Emulsion*", J. Kawada, U. Kose.

8. NuFact06 Workshop, 24-30 August 2006, University of California, Irvine, USA, "*Search for Charmed Pentaquarks at a Neutrino Factory*", G. De Lellis, M. Guler,

J. Kawada, U. Kose, O. Sato, F. Tramontano.

9. International Summer School on High Energy Physics: Standard Model and Beyond, 25-30 September 2006, Akyaka, Mugla, Turkey, "*Search for Anticharmed Pentaquark (Θ_c^0) in High Energy Antineutrino Interactions in the CHORUS Experiment and Future Neutrino Experiments at Neutrino Factory*", U. Kose, G. De Lellis, M. Guler, J. Kawada, O. Sato, F. Tramontano.

Publications:

1. Search for charmed pentaquarks in high energy antineutrino interactions. G. De Lellis, A. M. Güler, J. Kawada, U. Köse, O. Sato, F. Tramontano, Accepted for publication in Nuclear Physics **B** (2006).

2. First events from the CNGS neutrino beam detected in the OPERA experiment. By OPERA Collaboration (R. Acquafredda et al.), hep-ex/0611023; Accepted for publication in New Journal of Physics (2006).

3. Measurement of nucleon structure functions in neutrino scattering. By CHORUS Collaboration (G. Onengut et al.), CERN-PH-EP-2005-048; Phys. Lett. B632: 65-75, 2006.

4. Measurement of topological muonic branching ratios of charmed hadrons produced in neutrino induced charged-current interactions. By CHORUS Collaboration (A. Kayis- Topaksu et al.), CERN-PH-EP-2005-039; Phys. Lett. B626: 24-34, 2005.

5. Search for superfragments and measurement of the production of hyperfragments in neutrino nucleus interactions. By CHORUS Collaboration (G. Onengut et al.), CERN-PHEP- 2005-017; Nucl. Phys. B718: 35-54, 2005.

6. Measurement of D^{*+} production in charged-current neutrino interactions. By CHORUS Collaboration (G. Onengut et al.), CERN-PH-EP-2005-010; Phys. Lett. B614: 155-164, 2005.

7. Measurements of D0 production and of decay branching fractions in neutrino nucleon scattering. By CHORUS Collaboration (G. Onengut et al.), CERN-PH-EP-2005-008; Phys. Lett. B613: 105-117, 2005.

8. Measurement of charm production in antineutrino charged-current interactions. By CHORUS Collaboration (G. Onengut et al.), CERN-PH-EP-2004-057; Phys. Lett. B604: 11-21, 2004.

9. Measurement of fragmentation properties of charmed particle production in charged current neutrino interactions. By CHORUS Collaboration (G. Onengut et al.), CERN-PHEP- 2004-056; Phys. Lett. B604:145-156, 2004.

10. Experimental study of trimuon events in neutrino charged-current interactions. By CHORUS Collaboration (A. Kayis-Topaksu et al.), CERN-PH-EP-2004-029; Phys. Lett. B596: 44-53, 2004.

11. Cross-section measurement for quasi-elastic production of charmed baryons in nu N interactions. By CHORUS Collaboration (A. Kayis-Topaksu et al.), CERN-EP-2003-063; Phys. Lett. B575: 198-207, 2003.

12. Measurement of Lambda/c+ production in neutrino charged-current interactions. By CHORUS Collaboration (A. Kayis-Topaksu et al.), CERN-EP-2003-001; Phys. Lett. B555: 156-166, 2003.